University of Southampton

Faculty of Engineering, Science and Mathematics

National Oceanography Centre, Southampton

School of Ocean and Earth Sciences

Oceanic Planetary Waves in the Coupled Ocean-Atmosphere System

Riccardo Farneti

Thesis for the degree of Doctor of Philosophy

September, 2005

Graduate School of the National Oceanography Centre, Southampton

This PhD dissertation by

Riccardo Farneti

has been produced under the supervision of the following persons:

Supervisor:

Prof. Peter D. Killworth

Chair of Advisory Panel:

Prof. John Marshall

Member of Advisory Panel:

Prof. Harry L. Bryden

University of Southampton

ABSTRACT

Faculty of Engineering, Science and Mathematics
National Oceanography Centre, Southampton
School of Ocean and Earth Science

Doctor of Philosophy

Oceanic Planetary Waves in the Coupled Ocean-Atmosphere System

by Riccardo Farneti

September, 2005

The propagation of planetary, or Rossby, waves is studied under the effects of different atmospheric couplings. First, analytical matchings are formulated in which a Rossby wave is coupled to different thermodynamical atmospheres, from a simple heat flux condition to the inclusion of an atmospheric energy balance model. The effects on the vertical structure and phase speed of the first modes are negligible. However, it is shown that for the latter case an unstable mode appears. This growing mode, of decadal period and growth rate, has no physical source of energy and therefore is a result of the oversimplified atmosphere employed. In fact, adding physics to the atmospheric model results in a gradual disappearance of the instability. The possibility of observing similar unphysical modes in climate studies, where oversimplified models are adopted, is raised.

Next, a quasi-geostrophic coupled model is used in order to analyse the oceanic Rossby wave characteristics under the influence of a full atmosphere. The idealised eddy-resolving model consists of an ocean basin underneath a channel atmosphere, and different configurations for the oceanic component are used. The Rossby waves are observed to propagate faster than both the classical linear theory (unperturbed solution) and the phase speed estimates when the effect of the zonal mean flow is added (perturbed solution). Moreover, using statistical eigentechniques, a coupled Rossby wave is identified, bearing the characteristics of the coupled mode proposed by Goodman and Marshall (1999). It is argued that the atmospheric coupling is capable of adding an extra speed up to the wave; in fact, when the waves are simply forced, their propagation speed approaches the perturbed solution. The waves are observed to break into faster waves, as suggested by LaCasce and Pedlosky (2004), although their resistance to dissipation and instabilities processes is enhanced by the atmospheric coupling, which provides extra energy to the initial wave during its propagation. The development of a coupled Rossby wave is found to be possible in a basin of the dimensions of both the Pacific and the Atlantic ocean, and its characteristics and strength vary little when the tridimensional accuracy of the ocean is increased.

Declaration of Authorship

I, **Riccardo Farneti**, declare that the thesis entitled **'Oceanic Planetary Waves in the Coupled Ocean-Atmosphere System'** and the work presented in it are my own. I confirm that:

- this work was done wholly or mainly while in candidature for a research degree at this University;
- where any part of this thesis has previously been submitted for a degree or any other qualification at this University or any other institution, this has been clearly stated;
- where I have consulted the published work of others, this is always clearly attributed;
- where I have quoted from the work of others, the source is always given. With the exception of such quotations, this thesis is entirely my own work;
- I have acknowledged all main sources of help;
- where the thesis is based on work done by myself jointly with others, I have made clear exactly what was done by others and what I have contributed myself;
- Chapter 2 has been published as
  Farneti, R. and Killworth, P.D. (2005). The effects on oceanic planetary waves of coupling with an atmospheric energy balance model, *Tellus*, **57A**, 742-757.

Signed: .....

Date: .....

Acknowledgements

It is with pleasure that I thank my supervisor, Peter Killworth, first for giving me the opportunity to work on this Ph.D. and then for giving me the freedom of finding my way through it. It has been both challenging and rewarding, and I thank you for that. However, my *quasi-second supervisor*, Jeff Blundell, was often the link between Peter and me, helping in any computing issue and on the model set-up. Thank you.

The members of my advisory panel, Prof. John Marshall and Prof. Harry Bryden, are acknowledged for their constructive comments during my Ph.D. work.

I have benefited from many discussions with Paolo Cipollini (on Rossby waves, satellite observations, statistical analysis and Olive Oil) and with Andy Hogg (on Rossby waves, statistical analysis and Southern Hemisphere climate), who also shared with me some of his initial codes.

The Ph.D. experience was completed with old and new friends. My loyal housemate Angela and Gianluca, the *Marsigliesi* Manfredi & Giuseppe, Haris and Christos, Xana, Irene, Taro, Ale, my beloved *Alfa Romeo*, Rubia Farma and Puck who are waiting for me, and many others spread throughout Europe.

A special thanks to Anna, to all my family, to my brother for occasionally finance my "research" and to my mother for always encouraging me in doing what I wanted.

This is dedicated to my father.

Contents

List of Figures

List of Tables

Chapter 1

Introduction

In this introduction we describe the general dynamics of planetary waves and try to put them into a wider context, emphasising their role in the ocean circulation and the coupled ocean-atmosphere system. We start by giving a brief introduction of planetary wave theory and their general characteristics followed by a summary of the new theories developed since the advent of satellite altimetry and the role played in the ocean-atmosphere coupling. The chapter concludes with an outline of the structure of the thesis.

1.1 Planetary waves and their role in ocean and climate dynamics

The time-dependent ocean circulation has an important impact on our climate due to the ocean large heat capacity. Any abrupt change, the intrinsic variability and possible variations of the general circulation caused by the atmospheric influence is fundamental in climate studies. Moreover, the oceans are no longer considered passive in the atmosphere-ocean system, but contribute to the production of the climate low-frequency variability at interannual to decadal time scales (Talley, 1999; Dewar, 2001; Pierce et al., 2001).

The oceans are forced at the surface by the wind frictional stress and Rossby waves appear to play a fundamental role in redistributing and dispersing large-scale time-varying energy in the ocean. The propagation of Rossby waves towards the ocean interior under the influence of wind stress results in establishing a Sverdrup balance in the basin, accumulating energy in the western boundaries and intensifying currents there (Anderson and Gill, 1975, 1979).

The importance of Rossby waves in the spinup of the ocean and in the adjustment of the ocean interior was also recently shown by Johnson and Marshall (2002).

They proposed a theory for surface Atlantic response to thermohaline variability; in their work they study the reaction of the ocean to a perturbation of the rate of deep water formation at high latitudes. These changes initiate Kelvin waves which propagate along the western boundary, in a similar response of that demonstrated by Kawase (1987), and then cross the basin as equatorial Kelvin waves until they reach the eastern boundary where they propagate northwards and southwards. The final part of the response is the radiation of Rossby waves from the eastern boundary, communicating the thermocline displacement to the ocean interior which is clearly illustrated with a series of snapshots.

Due to the ubiquitous presence of Rossby waves in the world oceans they influence ocean gyres and air-sea fluxes at all latitudes, affecting in turn the atmospheric heat transport and circulation. They are believed to provide teleconnections between the equatorial and middle latitudes regions (Galanti and Tziperman, 2003) as well as transhemispheric and interbasin communications (Cessi and Otheguy, 2003). Other major effects are the maintenance and intensification of western boundary currents, transport of a large amount of heat and, because of their time-scale, they play a key role in the climate system.

1.1.1 The linear theory in a 3-layer ocean

The discovery of Planetary waves by the solution of Laplace's equation as the second class waves dates back to the late nineteenth century by Hough (1897). Later C.G. Rossby pointed out the characteristic of these waves, hence they carry his name and are also called Rossby waves.

Since then, Rossby wave theory is well known (Gill, 1982; Dickinson, 1978; Leblond and Mysak, 1978) and is usually applied to an ocean at rest with uniform depth.

Rossby waves owe their existence to the meridional variation of the Coriolis force (the β effect) and therefore propagate following an east-west waveguide, as the conservation of potential vorticity is their restoring force.

These kind of waves, whose frequencies are considerably lower than those of gravity waves and are subinertial ($\sigma \ll f$), are also sometimes called quasigeostrophic waves, with a dynamic evolution depending on the departure from geostrophy.

The generation of these waves is still not completely understood but the main forcing is wind stress and buoyancy forcing, though the latter is thought to act in a minor way, and upwelling-downwelling on the eastern boundary (Leblond and Mysak, 1978; Gill, 1982).

In order to obtain and describe the Rossby wave solutions, we consider the

linearised quasi-geostrophic (QG) potential vorticity equation (Pedlosky, 1987):

$$\partial_t q_i + J(\psi_i, q_i) = 0, \quad i = 1, ..., N \tag{1.1}$$

where $J(a, b) = a_x b_y - a_y b_x$ is the Jacobian, q_i the layer potential vorticity and ψ the stream function. Introducing a plane wave solution of the type $\psi = \Psi e^{i(kx+ly-\sigma t)}$ into (1.1) we naturally obtain the dispersion relation for Rossby waves, showing their basic characteristics (Leblond and Mysak, 1978; Gill, 1982)

$$\sigma = -\frac{\beta k}{(k^2 + l^2) + a^{-2}},$$

where σ is the frequency, k and l are horizontal wavenumbers, β is the meridional variation of the Coriolis parameter and a the Rossby radius (C/f , where C is the internal wave speed). It is clear that Rossby waves have westward phase velocities (of the order of a few cm/s) and that these are increasing toward the equator (where equatorial wave theory holds) with a maximum speed $c_x = \beta a^2$; the group velocities, C_g, in the case of long waves, are westward and the waves are nondispersive ($C_g = c_x$), while short waves propagate eastwards but with very slow speeds.

Another remarkable feature of the planetary wave dispersion relation is that not all frequencies exist, with a cutoff frequency at $\frac{1}{2}\beta a$.

Besides the horizontal problem, the vertical one is of great importance. Using a normal mode representation (Leblond and Mysak, 1978), separating the vertical and horizontal structure, we find an infinite set of solutions (or normal modes). The zeroth is the barotropic one, almost vertically independent and very rapid; the other solutions, or modes, are called baroclinic with decreasing phase speeds and increasing oscillation in the vertical. A first-mode baroclinic Rossby wave takes months to years to cross an ocean basin, depending on the latitude.

In the case of a 3-layer ocean, the potential vorticities are given by

$$\begin{aligned} q_1 &= \nabla\psi_1 + \beta y - F_{11}(\psi_1 - \psi_2) \\ q_2 &= \nabla\psi_2 + \beta y - F_{21}(\psi_2 - \psi_1) - F_{22}(\psi_2 - \psi_3) \\ q_3 &= \nabla\psi_3 + \beta y - F_{32}(\psi_3 - \psi_2), \end{aligned}$$

where $F_{m,n} = f_0^2/(H_m g'_n)$ and g'_i and H_i are the reduced gravities and layer depths respectively.

For this 3-layer system, substitution of a plane wave solution leads to a generalised eigenvalue problem of the form $\mathsf{A}\Psi = \sigma\mathsf{B}\Psi$, or explicitly:

$$\begin{bmatrix} \beta_1 & 0 & 0 \\ 0 & \beta_2 & 0 \\ 0 & 0 & \beta_3 \end{bmatrix} \begin{bmatrix} \psi_1 \\ \psi_2 \\ \psi_3 \end{bmatrix} = \sigma \begin{bmatrix} -G_1 & 1 & 0 \\ G_2 & -G_3 & 1 \\ 0 & 1 & -G_4 \end{bmatrix} \begin{bmatrix} \psi_1 \\ \psi_2 \\ \psi_3 \end{bmatrix},$$

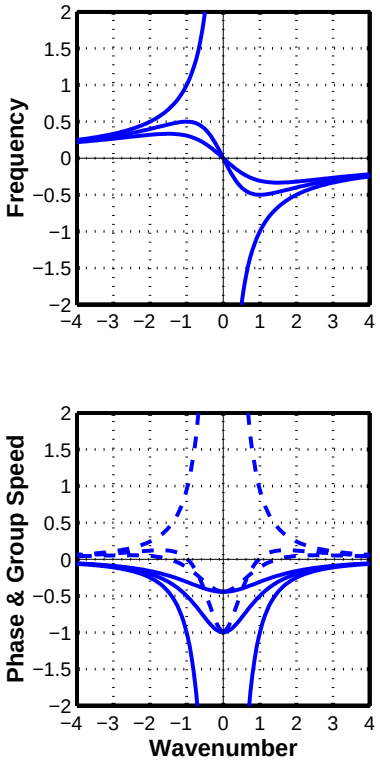

Figure 1.1: *Upper panel: the dispersion relation for the barotropic and first two baroclinic modes of the 3-layer QG ocean. Shown are values of both positive and negative wavenumbers. The wavenumber is scaled by the deformation radius a and the frequency by βa; the meridional wavenumber l is set to zero. Lower panel: phase (solid lines, $c_x = \sigma/k$) and group (dashed lines, $Cg_x = \partial\sigma/\partial k$) velocities of the barotropic and first two baroclinic modes, scaled by βa^2.*

where $\beta_1 = (k\beta)/F_{11}$, $\beta_2 = (k\beta)/F_{22}$, $\beta_3 = (k\beta)/F_{32}$ and $G_1 = (K^2 + F_{11})/F_{11}$, $G_2 = F_{21}/F_{22}$, $G_3 = (K^2 + F_{21} + F_{22})/F_{22}$, $G_4 = (K^2 + F_{32})/F_{32}$, where $K^2 = k^2 + l^2$.

The solution of the system is plotted in Fig.1.1 and it describes the basic properties of Rossby wave propagation. In fact, for the 3-layer system, the dispersion relation is found on the upper panel and both phase and group velocities on the bottom panel of Fig.1.1. We can distinguish the barotropic mode with increasing frequencies towards long wavelengths, very fast phase speeds and positive (eastward) group velocities. The baroclinc modes have smaller frequencies, their phase velocities are always westward but their group velocities turn from westward to eastward at the point of maximum frequency ($ka = |1|$, $\sigma/(\beta a) = |0.5|$), where the group velocity is zero. Therefore, long baroclinic waves direct their energy westward while short waves direct it eastward. This means that, in the limit of long wavelengths, the phase and group speeds are the same and the waves are nondispersive. On the other hand, for short waves phase and group speeds differ and the waves are dispersive. The maximum group and phase velocity ($C_x = Cg_x = -\beta a^2$) are attained for long waves, they are to the west and can be found on the axis origin of the dispersion relation.

The system could be extended to an N-layer or even, as proposed in chapter

2, to a continuously stratified ocean. In every case, the solutions obtained are one barotropic and N-1 baroclinic modes of decreasing phase speeds. This method of analysis is called the *normal modes method*, in which the ocean is decomposed into an infinite set of solutions (or modes): one barotropic (or external) and the remaining baroclinic (or internal).

1.1.2 The linear theory revisited

The linear theory, generally explained in the preceding sections, was accepted for a long time, due to the difficulty in obtaining direct observations of Rossby waves in the ocean[1], except some international projects like the USSR Polygon experiment in 1970 and the Mid-Ocean Dynamics Experiment (MODE) some years later. Both experiments carried out studies investigating mesoscale motions and observed a good fit of the Rossby waves characteristics with mooring data and identifying mesoscale eddies satisfying the dispersion relation for linear Rossby waves (Leblond and Mysak, 1978; Dickinson, 1978).

With the advent of satellite altimetry the direct observation of large-scale propagating disturbances has become possible and it has been pointed out, first by Chelton and Schlax (1996), that the speed of Rossby waves is faster than that predicted by standard linear theory. After these first results, the need for reconsidering and improving the theory became clear as standard theory for freely propagating, linear, baroclinic wave is deficient.

Killworth et al. (1997) have tested different possibilities for this deficiency. They have suggested that a coupled system (that is, the waves are not free) is not able to magnify Rossby waves speed in a ubiquitous way, that the effect of a varying topography could be important, though it is not clear that it could always result in a speedup, that the nonlinearity is not supported by observations and finally they studied the role of the background state of the ocean.

They investigated the case of an east-west mean flow, inducing changes in the gradient of potential vorticity, analytically with different velocities and numerically with different stratifications. The results matched and explained the speedup of the waves, with the new phase speed being a linear combination of the mode-1 speed and the amplitude of the mean flow. Finally, they used Levitus and Boyer data to reproduce the baroclinic background flow and plot the new perturbed velocities in the ocean finding a good agreement almost everywhere, attaining a ratio of 2

[1]Rossby waves in the atmosphere are easily detected as perturbation (undulations) of the mid-latitude jet stream and are responsible of the generation of different weather systems (Gill, 1982; Kundu and Cohen, 2002).

for the perturbed and unperturbed velocities at high latitudes as indicated by the observations of Chelton and Schlax (1996).

Thus, it seems that the presence of a baroclinic mean flow is able to increase the Rossby wave phase velocities and to explain them in their majority. Furthermore, Killworth et al. (1997) did not find any significant difference in their results adding a barotropic flow.

Dewar (1998) found similar results in his investigations confirming the previous results. In his study, he used a 3-layer quasigeostrophic (QG) model looking at the interaction between Rossby waves and the vertical shear; first with a linear analysis and then with a nonlinear one with a general forcing and a continously stratified ocean showing that a 3-layer QG model is needed at the very least to capture the dynamics of the wave propagation.

Probably the most important result in Dewar (1998) is the asymmetry in the changes in phase velocities: they are found to be larger at the west than at the east (because of the increasing role of the mean flow effect toward the western basin) and accelerated in the northern half of the subtropical gyre and decelerated in the southern half, in good agreement with Chelton and Schlax (1996). Dewar and Morris (2000) used an eddy-resolving QG numerical model to study first-mode long planetary wave propagation and mean flow interaction, arguing that the full QG model matched well with the theory and the observations. Thus, they concluded that a 3-layer model captures this interaction qualitatively, but had several problems in explaining and reproduce near equatorial propagation.

In conclusion, Killworth et al. (1997) and Dewar (1998) seem to agree, probably because they both use the same hypothesis (the vertical shear and the potential vorticity field), though applying a different approach.

Even though all the discrepancies are not explained, not much space is left for other factors involved in the perturbation of wave phase velocities. The work of Killworth and Blundell (1999) partly confirmed this, finding that a slowly varying bottom topography was not able to speedup planetary waves. Results demonstrating localised effects have been found with phase speeds increasing in shallow waters, westward and equatorward of an isolated seamount, but with the general effect being negligible.

Intuitively, bearing in mind all the previous results, one would think that adding a varying bottom topography to a baroclinic shear flow would not change the results found by Killworth et al. (1997) and Dewar (1998), but this does not seem to be the true. Recently, Killworth and Blundell (2003) proposed this case and found a second speed-up of the wave phase velocities but without giving a complete reason for this and opening new questions about coupled/uncoupled planetary wave propagation

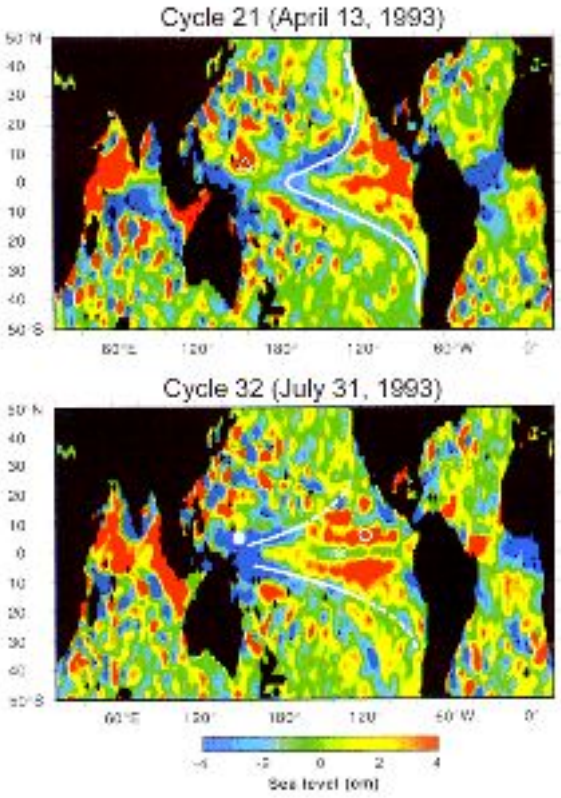

Figure 1.2: *Sea surface height anomalies showing the propagation of planetary waves in the Pacific Ocean. Also clear is the β-effect inducing larger phase speeds towards the equator [from Chelton and Schlax (1996)].*

and group velocities.

A completely different hypothesis for the observed high phase speeds is given by LaCasce and Pedlosky (2004). They consider the stability of oceanic Rossby waves in a 2-layer QG ocean and conclude that they are subject to a β-dependent baroclinic instability. That is, the instability is stronger as we move northward and the waves cannot travel very far at high latitudes because they break into barotropic vortices following an inverse cascade mechanism. Those barotropic vortices (or waves) possess phase speeds of the order of twice the linear baroclinic one, and the authors argue that this could be the reason for the *too fast* Rossby waves. Although Rossby waves are definitely subject to strong instability processes in a real turbulent ocean, the possibility of detecting such barotropic waves with satellite altimetry is still controversial.

It is worth noting that all these theoretical considerations are based on dynamics on a β-plane. Paldor and Mariano (2005) discuss the limitations of this assumption considering the equations on a spherical earth and points out the conservation of angular momentum as a reason for the discrepancies in phase speeds.

As anticipated, the advent of satellite altimetry brought a powerful tool to describe Rossby waves in the real ocean. The TOPEX/POSEIDON (T/P) altimeter is

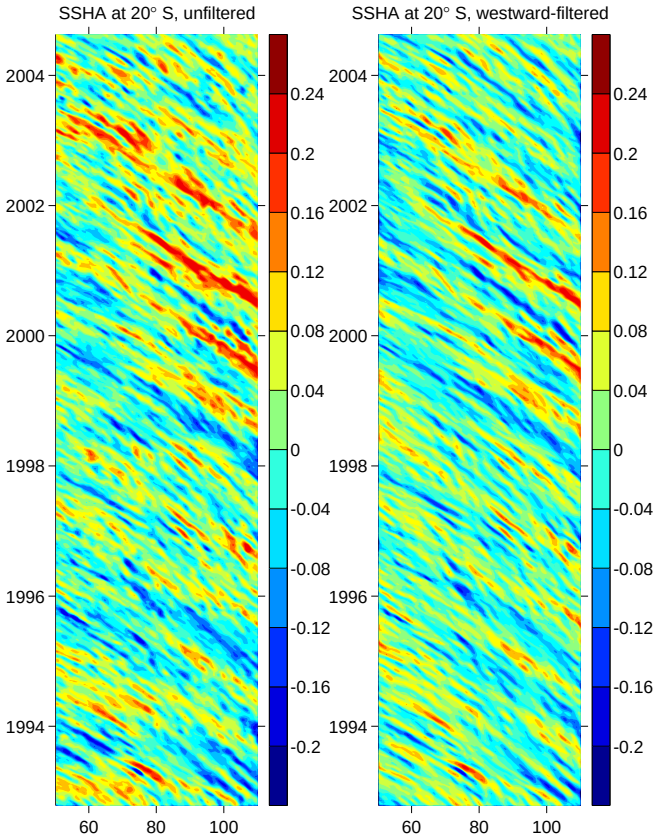

Figure 1.3: *Time-longitude plot of the sea surface height anomalies (in meters) in the Indian Ocean at 20°S. On the left panels, the original altimeter data. On the right panel, the corresponding westward-filtered signature. There is a clear evidence of crests and troughs propagating westward with a biannual period (Courtesy of P. Cipollini).*

able to detect long baroclinic planetary waves unambiguously over the entire world ocean.

Chelton and Schlax (1996) presented for the first time the results of these observations identifying clear Rossby waves signals (Fig.1.2) and common features like the increase of phase speed in the western basin, the effect of bottom topography, eastward propagating equatorially trapped Kelvin waves and pulses related to El Niño events.

Globally, Rossby wave phase velocities were found to be greater than those predicted by standard theory and up to twice their value at mid-latitudes. This has motivated the theoretical studies described in the previous section (Killworth et al., 1997; Dewar, 1998; Killworth and Blundell, 1999; Dewar and Morris, 2000) and several satellite-based investigations (Hill et al., 2000; Hughes, 1995; Cipollini et al., 2001; White et al., 1998).

The T/P altimetry data reveal the sea surface height anomalies (SSHA) and to analyse this data time-longitude plots, known as Hovmöller diagrams, are used, which clearly show Rossby waves as diagonal alignments of crests and troughs moving westward. An example of this is given in Fig.1.3, where SSHA data from the Indian Ocean are plotted for the latitude 20°S from 1993 till May 2005; in the left

panel the row data are plotted while in the right panel the data have been filtered with a westward filter to better show Rossby wave propagation.

By this technique, Rossby waves are detected in all basins and altimetry has been used also in the Southern Ocean (Hughes, 1995) where two dynamical systems were found, a supercritical and a subcritical one with respect to Rossby waves, the first one being able to advect the waves eastward.

Rossby waves are also detected by other sensors like the Along-track Scanning Radiometer (ATSR) in sea surface temperature (SST) and, recently, SeaWiFS in ocean colour.

As an example, Hill et al. (2000) used a SST record to compute Rossby wave phase speeds finding good agreement with Killworth et al. (1997). They were also able to detect topographic effects such as those predicted by Killworth and Blundell (1999).

One of the latest applications has been using ocean colour. Cipollini et al. (2001) found for the first time Rossby waves in SeaWiFS datasets, although they are neither very clear nor ubiquitous. A preliminary explanation for this detectability was in term of the vertical displacements of the thermocline associated with the Rossby wave and subsequently changes in the nutrient upwelling, however, Killworth et al. (2004) concluded that the chlorophyll signal can be explained by horizontal advective processes.

1.1.3 The role in the coupled ocean-atmosphere system

Planetary waves are very slow oceanic movements and their time-scale is so that they acquire a central role in the climate dynamics at interannual to decadal time scales. Not only they transfer and distribute atmospheric informations to the ocean interior but they also directly interact with the atmosphere above them.

Several mechanisms have been identified in which Rossby waves are a key component. The El Niño Southern Oscillation (ENSO) is probably the most common, but others exist, like the newly described (and still controversial) Antarctic Circumpolar Wave (ACW, White and Peterson, 1996).

Coupled ocean-atmosphere modes, in which oceanic baroclinic Rossby waves set the "clock" of the coupled interaction, develop at both equatorial- and mid-latitudes, and have been observed (White et al., 1998; White, 2000a, 2001; Jin et al., 2003), modelled (Latif and Barnett, 1994; Münnich et al., 1998; Barnett et al., 1999; Solomon and McCready, 2003) and studied with the help of simple analytical models (Jin, 1997; Qiu and Jin, 1997; Talley, 1999; Neelin and Weng, 1999; Goodman and Marshall, 1999; Ferreira et al., 2001; Bye, 2004).

The basic mechanism by which oceanic Rossby waves can couple to the troposphere is as follows: the propagation of baroclinic waves in the ocean generates undulations in the thermal field associated with the mixed layer depth, this causes SST anomalies that influence the tropospheric heat structure and therefore its circulation. As a result of this, anomalous winds are generated and a stress is exerted over the ocean. Depending on the spatial phase relationship between several oceanic and atmospheric variables, this anomalous wind stress can amplify the subsurface undulations and the related SST field, leading to a positive feedback. Otherwise, the coupled mechanism leads to a damping of the anomalies and the couple mode slowly dies away.

Because of their period and their role in setting the time-scale in the coupled modes, oceanic Rossby waves are crucial in decadal ocean and climate variability, as confirmed by many studies (Latif and Barnett, 1996; Capotondi and Alexander, 2001; Arzel and Huck, 2003).

As mentioned above, oceanic Rossby waves have been observed to be coupled with the overlying atmosphere and some simple ocean-atmosphere models have been formulated in order to try to explain the coupled mode mechanism. However, a detailed study focused on Rossby wave propagation under an atmospheric coupling, the effects on the general wave dynamics and the identification of a truly coupled Rossby mode in a non-linear coupled model of intermediate complexity is lacking in the literature.

This will be the main aim of the thesis, which is explained in the following section together with its general organisation.

1.2 Aims and structure of the thesis

A coupled ocean-atmosphere study will be carried out in which primary attention will be given to oceanic Rossby wave propagation.

Different stages of complexity in the coupling will be considered, from a simple analytical coupling with a simplified thermal atmosphere to a fully non-linear ocean-atmosphere coupled model.

In a first very idealised study, coupling mechanisms such as a heat flux condition at the surface and a simple Energy Balance atmosphere will be introduced to the long-wave equations for a continuously stratified ocean on a β-plane. The wave response will be studied under the different couplings and the relevance of these to climate models will be addressed.

Then, a quasi-geostrophic coupled model, recently developed at the National Oceanography Centre, Southampton (Hogg et al., 2003a,b), will be used to study

the Rossby wave propagation influenced by both thermodynamical and mechanical atmospheric coupling and the results compared to the linear theory. Finally, in the context of a fully coupled ocean-atmosphere model, the identification of a coupled Rossby mode will be pursued, compared with previous studies and examined under different configurations.

In summary, we will try to answer the following questions:

- What is the response of a Rossby wave coupled to a thermal atmosphere?, that is, is the wave damped by atmospheric heat fluxes?
- What are the Rossby wave characteristics in terms of phase speed and stability in a coupled ocean-atmosphere model?
- And finally, are the waves coupled to the atmosphere? can an unstable coupled mode exist and what is the mechanism of such coupling?

In Chapter 2 we study the simple coupling of a Rossby wave to an atmospheric Energy Balance Model. Chapter 3 explains the main features of the QG coupled model employed in this thesis. In Chapter 4 we investigate the oceanic Rossby waves in the model with the help of statistical techniques, analysing their coupling with the atmosphere; this is followed by a test on the results applying a different configuration to the coupled model in Chapter 5. Finally, we summarise and discuss the main results and future studies in Chapter 6.

Chapter 2

The effects of coupling with a thermal atmosphere †

This chapter shows the existence of a growing planetary-wavelike ocean mode, with a decadal period and growth rate, which appears when a stratified, diffusive ocean is coupled to a simple atmosphere via an energy balance model (EBM). Such modes are not found when simpler surface ocean conditions are applied. The mode is low order in the vertical and, because of its slow growth, is likely to be observed in Earth System Models using an EBM in place of a fuller set of atmospheric dynamics. There is no apparent physical energy source for such a mode, and therefore it should not be expected to arise in such a model. The mode is analysed through a hierarchy of simple models which differ only through their surface boundary condition.

2.1 Introduction

Energy Balance Models (EBMs) have been very useful for the development of coupled models for thermohaline circulation studies (Pierce et al., 1996; Bjornsson et al., 1997; Huck et al., 2001; Kravtsov and Dewar, 2003) as well as for decadal-interdecadal climate variability identification (Barsugli and Battisti, 1998, BB98 hereafter). The latter study found that the coupling of a simple ocean with an atmospheric EBM is able to reduce the energy fluxes between the ocean and atmosphere increasing at the same time the variance of both the atmosphere and ocean. It is argued in their paper that this model based on thermal coupling only is a valid tool for understanding the basic effects of ocean-atmosphere coupling at midlatitudes. EBMs have also played a fundamental role in the early development of Earth System Models (North, 1975; North et al., 1981; Harvey, 1988; Trenberth, 1992;

†This chapter is published as Farneti, R. and P.D. Killworth, 2005: The effects on oceanic planetary waves of coupling with an atmospheric energy balance model. *Tellus*, **57A**, 742-757.

Weaver et al., 2001) since a fully active atmospheric model is usually too slow for the lengthy integration periods under investigation.

Though still very simplified, the one-dimensional EBM is very popular for reproducing coupled ocean-atmosphere systems (Kiehl, 1992). It is the simplest model of the coupled system at midlatitudes and often agrees well with more sophisticated GCM studies. Other studies have focused on couplings with different oceans, from a slab ocean to an OGCM, with sometimes the explicitly inclusion of the results of latent heat through moisture (Fanning and Weaver, 1996; Bjornsson et al., 1997).

Nonetheless, EBMs are a drastic simplification of the atmospheric reality, and it is important to understand both their features and their shortcomings. Is it possible for a model including an EBM to possess unphysical responses, for example? A possible hint is given by the study by Goodman and Marshall (1999), who described a model which, using both dynamical and thermal forcing as coupling mechanisms, supports growing coupled modes in the decadal period via positive feedbacks between the atmosphere and the ocean. Some limitations of Goodman and Marshall (1999) were addressed by Ferreira et al. (2001), mainly in the use of a bounded basin, exploring the air-sea interactions at midlatitudes with a two-layer quasigeostrophic channel atmosphere. In their work, the atmosphere component of the coupled model consists of an EBM, similar to BB98, and explicit dynamics. When Ferreira et al. (2001) couple their atmosphere to an oceanic mixed layer, their results are in better agreement with previous GCM studies, with their success attributed to the inclusion of atmospheric dynamics.

The purpose of this chapter is to examine how an EBM may be implicated in the production of a growing mode of oscillation when an EBM is coupled to an ocean under conditions relevant to climate simulations (long period, predominantly geostrophic, etc.). This is done by coupling a stratified ocean which includes a vertical diffusivity[1] to a succession of slightly more complicated surface boundary conditions, in the context of Rossby, or planetary, waves. These waves are the main mechanism whereby climatic information is carried around the ocean.

The concept of Rossby wave coupling to the overlying atmosphere is hardly new (consider White et al., 1998; White, 2000a, for example); but no clear attempt has been made so far to explain or study the effects on the wave structure and propagation. Nonetheless, experiments with coupled atmosphere-ocean systems in which planetary waves play a major role have proliferated (Frankignoul et al., 1997; Jin, 1997; Qiu and Jin, 1997; Goodman and Marshall, 1999; Colin de Verdière and Blanc, 2001; Ferreira et al., 2001) in the attempt of better understanding and increasing

[1]Qiu et al. (1997) has examined the effects of horizontal eddy diffusion in a 1.5-layer model, finding no change to the westward phase speed of free long baroclinic waves.

the predictability of the decadal-interdecadal climate variability.

Indeed, Jin (1997) found a spectral peak in the decadal-interdecadal period due to the resonance of the forced oceanic Rossby waves in his reduced-gravity uncoupled model but also an oscillatory mode with an interdecadal peak when the model was coupled. Also, this mode was found to be unstable when positive thermal feedbacks were present.

The question of why planetary waves are observed to propagate faster than the linear theory predicts has been tackled in many ways. Since Chelton and Schlax (1996) published their results, many authors have tried to match the satellite results with a more complete theory. The inclusion of a baroclinic mean flow into a continuously stratified ocean, inducing changes in the gradient of potential vorticity, has been the first and probably the most successful study (Killworth et al., 1997). The results matched and explained the speed-up of the waves and were in good agreement with observations almost everywhere. Although these results were a good approximation to the observed phase speeds, not all discrepancies were explained.

The importance of topographic effects was also considered in Killworth and Blundell (1999), but they were found to be negligible over an entire basin; however, when the effects of a mean flow and bottom topography are combined a second speed-up is found (Killworth and Blundell, 2003).

The first study to address the question of how dissipative mechanisms influence the propagation of baroclinic planetary waves was by Qiu et al. (1997). Dissipation in the form of horizontal eddy diffusion in a 1.5-layer model of a forced ocean induced no changes in the westward phase speed of the free long baroclinic waves. Moreover, the free Rossby wave was found to be more sensitive to eddy dissipation at higher latitudes, due to its e-folding latitudinal dependence.

The purpose of this study is to identify another potential cause of differences in planetary wave propagation from the classic linear theory: the coupling with the atmosphere.

We will be concerned not with direct wind or buoyancy forcing, which can be effective generators of forced waves, but with the response of the ocean surface to the atmosphere above for free waves.

We examine the role of an EBM as follows. After the introduction of the vertical diffusion coefficient K_v into the stratified ocean wave equation, exchanges with the atmosphere take the form of a surface boundary condition to an eigenmodal problem. Only the first few normal modes of the system are of interest, as the remainder possess higher vertical structure than is observed. Various boundary conditions will be employed: no flux to the atmosphere (NF, hereafter), a vertical diffusive heat

flux of sensible heat to the atmosphere (HF, hereafter) and the coupling with an EBM. However, as we shall show, when an EBM provides a surface condition, a growing mode which is low order in the vertical is permitted. This mode does not exist with the other surface boundary conditions. More complete models involving an atmospheric EBM have proved the presence of sustained oscillations in the ocean (Cessi, 2000; Huck et al., 2001), but the inclusion of wind stress in the case of Cessi (2000) and of mean flow in Huck et al. (2001) was essential.

2.2 Formulation of the coupling

2.2.1 The ocean

The introduction of the vertical diffusivity coefficient K_v into the long wave equations for a continuously stratified Boussinesq ocean on a β-plane is formulated.

The perturbation equations of momentum, continuity and conservation are

$$u_t - fv + \frac{1}{\rho_0} p_x = 0 \tag{2.1}$$

$$v_t + fu + \frac{1}{\rho_0} p_y = 0 \tag{2.2}$$

$$p_z = -\rho g \tag{2.3}$$

$$u_x + v_y + w_z = 0 \tag{2.4}$$

$$\rho_t + \bar{\rho}_z w = K_v \rho_{zz} \tag{2.5}$$

where u,v and w are the velocity components, ρ and p are the perturbation density and pressure fields, g is the gravitational acceleration, $f = f_0 + \beta y$ is the Coriolis parameter, β the meridional gradient of f, K_v is the vertical diffusion coefficient and subscripts denote partial derivatives.

The addition of vertical diffusion effects requires some background density forcing to maintain the background stratification (which is denoted by an overbar). As is customary in perturbation studies, this is ignored henceforth.

Eliminating the vorticity terms between (2.1)-(2.2) we get

$$w_{ztt} + f^2 w_z - f\beta v - \beta u_t = \frac{1}{\rho_0} \nabla^2 p_t. \tag{2.6}$$

Introducing plane wave form eigensolutions of the type

$$[u, v, w, p] = e^{i(kx+ly-\sigma t)} [\hat{u}, \hat{v}, \hat{w}, \hat{p}]$$

and after using (2.3), we have (dropping the hats)

$$f^2 w_{zz} - f\beta v_z + i\sigma\beta u_z = \frac{-i\sigma(k^2 + l^2)}{\rho_o} \rho g. \tag{2.7}$$

Here we have made use of the approximation of low-frequency motions, $\sigma \ll |f|$, typical for planetary wave studies.

To leading order we may now substitute geostrophy

$$u = \frac{-ilp}{f\rho_o}, \quad v = \frac{ikp}{f\rho_o}$$

into (2.7), arriving at the expression

$$f^2 w_{zz} + \beta ik\frac{\rho g}{\rho_o} = -i\sigma(k^2 + l^2)\frac{\rho g}{\rho_o}, \tag{2.8}$$

where again $\sigma/f \ll 1$ has been used. This leads in turn to

$$\rho = \frac{if^2\rho_o}{g[\sigma(k^2 + l^2) + \beta k]} w_{zz}, \tag{2.9}$$

which relates the density to the second derivative of w. This relationship will be used throughout this study to formulate the coupling as one of the boundary conditions at the surface.

Substituting the expression for ρ into the conservation of density and rearranging yields an expression for the vertical velocity

$$N^2[\sigma(k^2 + l^2) + \beta k]w = -iK_v f^2 w_{zzzz} + \sigma f^2 w_{zz} \tag{2.10}$$

where $N^2 = -g\bar{\rho_z}/\rho_o$.

Diffusion, being a fourth derivative, is therefore not expected to alter the frequency of the wave significantly. In fact, the surface boundary layer generated by K_v should have a thickness of 100-200 m depending on k (this is discussed later). Computing the phase speeds with the inclusion of the predicted homogeneous boundary layer leads to no differences from the unperturbed solutions.

Setting $K_v = 0$ reduces the problem to the classical Sturm-Liouville problem (e.g., Gill (1982))

$$w_{zz} + \frac{N^2}{C^2} w = 0 \tag{2.11}$$

together with vanishing w at surface[2] and floor, where the eigenvalue C, the internal wave speed, is related to the frequency by

$$\sigma = -\frac{\beta k}{(k^2 + l^2) + a^{-2}} \tag{2.12}$$

and $a = C/f$ is the Rossby radius of deformation.

[2]The assumption of a rigid lid does lose the possibility of an interaction between barotropic and baroclinic modes which could occur in the presence of diffusion. This is likely to be negligible, since it is of order the small parameter C^2/gH.

If the diffusivity is non-zero, then two more boundary conditions are required for the fourth order eigenvalue problem (2.10). The condition of no heat flux through the floor requires from (2.9) that

$$w_{zzz} = 0, \quad z = -H. \tag{2.13}$$

The last boundary condition is at the surface. In the case of no heat flux at the surface (the NF case), (2.9) gives

$$w_{zzz} = 0, \quad z = 0 \tag{2.14}$$

though this boundary condition will be changed later to permit fluxes to and from the atmosphere.

The eigenvalue problem (2.10), (2.13), (2.14) must be solved numerically (though analytical solutions are possible for simple forms of $N^2(z)$, the algebra is tedious and unenlightening). The problem is cast onto a fine-resolution finite-difference grid (5 m spacing) so that any boundary layer structure can be adequately resolved. Such resolution is not too computationally expensive. Then (2.10) is converted into a matrix eigenvalue problem of the form $\mathsf{A}\hat{w} = \sigma\mathsf{B}\hat{w}$, where A and B are the matrices of the coefficients and $\sigma = (\sigma_r + i\sigma_i)$ the complex eigenfrequency; the eigenvectors $\hat{w}$ and associated eigenvalues are ordered by decreasing value of σ. The meridional wavenumber, l, is set to zero for simplicity. The square of the Brunt-Väisälä frequency, N^2, is an exponential function of z ($N^2 = N_0^2 e^{-\gamma z/H}$), where $N_0^2 = 10^{-5}\mathrm{s}^{-2}$ is the stratification at $z = 0$ and $\gamma = 3.7$ a typical midlatitude value (Killworth et al., 1997).

The system is solved numerically with NAGLIB's generalised eigenvalue problem solver routines.

With a β-plane centred at 30^oN, we set

$$f = 0.7{\times}10^{-4}\mathrm{s}^{-1}, \quad \beta = 2{\times}10^{-11}(\mathrm{m\ s})^{-1},$$
$$K_v = 10^{-4}\mathrm{m}^2\mathrm{s}^{-1}, \quad H = 5{\times}10^3\mathrm{m}.$$

For the stratification considered, $C_1 = 2.37782\ \mathrm{ms}^{-1}$ is the internal wave speed for the first mode, and therefore $a = C_1/f = 23.7782{\times}10^3$m is the Rossby radius of deformation. Due to the choice of a weak N_0^2, the resulting radius of deformation is possibly small, but the effects on the eigenmodes will be discussed later.

2.2.2 The atmospheric energy balance model

A one-dimensional, linear EBM is used to simulate the basic coupling between the atmosphere and ocean in the midlatitudes.

We use here the model of BB98 with the only difference being that there is no dynamical forcing in this case. The basic mechanisms of the different EBMs in the literature are very similar. The model takes into account the balance between shortwave, longwave and surface fluxes and thus reproduces the balance of incoming and outgoing radiant energy. BB98's equations, linearised about the climatological mean state and neglecting any dynamical forcing, are

$$\gamma_a \partial_t T_a = -\lambda_{sa}(T_a - T_o) - \lambda_a T_a \tag{2.15}$$

$$\gamma_o \partial_t T_o = \lambda_{so}(T_a - T_o) - \lambda_o T_o. \tag{2.16}$$

Here subscripts "a" and "o" refer to atmosphere and ocean respectively; T is the anomalous temperature; $\gamma_a = \rho_a C_{pa} H_a$ and $\gamma_o = \rho_o C_{po} H_o$ the heat capacities; λ_s the linearised coefficient of combined latent, sensible and longwave heat flux; λ_a and λ_o(bulk transfer coefficients) are the radiative damping of each component to space. The standard values for the ocean are ρ_o = 1024 kg m^{-3}, C$_{po}$ = 4×10^3 J (kg K)$^{-1}$, T$_o$ = 285 K, and for the atmosphere ρ_a = 1.25 kg m^{-3}, C_{pa} = 1×10^3 J (kg K)$^{-1}$, T_a = 270 K, H_a = 8.4× 10^3 m, ϵ = 0.76, σ_b=5.67×10^{-8} W (m^2 K^4)$^{-1}$, where ϵ is the longwave emissivity and σ_b the Stefan-Boltzmann constant. Finally, following BB98, we choose λ_{sa} = 23.9, λ_{so} = 23.4, λ_a = 2.8 and λ_o = 1.9 (in units of W m^{-2}K^{-1}).

After taking the Fourier transform ($\partial_t \rightarrow -i\sigma$), BB98's equations take the form

$$-i\sigma\gamma_a T_a = \lambda_{sa} T_o - (\lambda_{sa} + \lambda_a) T_a \tag{2.17}$$

$$-\gamma_o^{'} K_v \partial_z T_o = \lambda_{so} T_a - (\lambda_{so} + \lambda_o) T_o. \tag{2.18}$$

Here the ocean heat equation has been converted into a vertical diffusive flux towards the interior, the ocean heat capacity has become $\gamma_o^{'} = \rho_o C_{po}$ and the assumption that

$$\rho_o C_{po} K_v \partial_z T_o \cong \rho_o C_{po} H_o \partial_t T_o, \tag{2.19}$$

where H_o is a mixed layer depth, has been made.

The ocean equation (2.18) is the same as the one used in (Bjornsson et al., 1997, their eq. 20), if the contribution from the evaporation term is neglected.

It is straightforward to prove that (2.17)-(2.18), with (2.19) substituted, is a stable system with two different and negative eigenvalues.

From (2.17):

$$T_a\Big(\frac{\lambda_{sa} + \lambda_a}{\lambda_{sa}} - i\sigma\frac{\gamma_a}{\lambda_{sa}}\Big) = T_o, \tag{2.20}$$

which describes the relationship between the atmospheric and oceanic temperature for every eigenfrequency; the presence of an imaginary part indicates a phase shift between T_a and T_o.

Substituting (2.20) into (2.18) and rearranging yields

$$-\frac{\gamma_o^{'}}{\lambda_{so}} K_v \partial_z T_o = \Big(\frac{\lambda_{sa}+\lambda_a}{\lambda_{sa}} - i\sigma\frac{\gamma_a}{\lambda_{sa}}\Big)^{-1} T_o - \Big(\frac{\lambda_{so}+\lambda_o}{\lambda_{so}}\Big) T_o, \tag{2.21}$$

or:

$$-\Gamma_o^{'} \partial_z T_o = \Big[\Big(\Lambda_a - i\sigma\Gamma_a\Big)^{-1} - \Lambda_o\Big] T_o, \tag{2.22}$$

where the following substitutions have been made: $\Gamma_o^{'} = (\gamma_o^{'}/\lambda_{so})K_v$, $\Gamma_a = (\gamma_a/\lambda_{sa})$, $\Lambda_o = (\lambda_{so}+\lambda_o)/\lambda_{so}$ and $\Lambda_a = (\lambda_{sa}+\lambda_a)/\lambda_{sa}$.

Equation (2.22) will be the new surface boundary condition for (2.10) in the EBM case.

Using again the relationship described in (2.9), the suitable form for the boundary condition in the EBM case becomes:

$$-\Gamma_o^{'} w_{zzz} = \Big[\Big(\Lambda_a - i\sigma\Gamma_a\Big)^{-1} - \Lambda_o\Big] w_{zz}, \tag{2.23}$$

The accuracy of our grid spacing was tested for the resulting σ and the length scale (of around 10 m) was found to be well resolved.

The new coupling involves incoming longwave and surface fluxes to the ocean modulated by the eigenfrequency and a direct estimate of the atmospheric and oceanic temperature feedback.

2.2.3 A surface thermal boundary condition

To permit investigation of the possible effects of simpler matching to the atmosphere, we also construct a simpler coupling of heat fluxes at the ocean surface through a surface thermal boundary condition. Restoring boundary conditions implicitly model the atmosphere and the vertical diffusive heat flux only considers the sensible heat (Haney, 1971). In this case, only losses towards the atmosphere are possible.

In this case we will allow a heat flux to the atmosphere with a simple matching via one of the boundary conditions. We will consider a standard vertical diffusive heat flux,

$$Q = -\rho_0 C_{po} K_v \partial_z T_o, \tag{2.24}$$

where

$$Q = \partial_T Q T^{'},$$

is proportional to the vertical diffusivity of heat and the vertical gradient of temperature, C_{po} is the ocean heat capacity and T_o its temperature.

The heat flux Q is reformulated in order to give the following expression:

$$-K_v \partial_z T_o|_{z=0} = \tau T', \tag{2.25}$$

where $T^{'}$ is the difference between oceanic and atmospheric temperature and $\tau = (1/\rho_0 C_{po})\partial_T Q = 1.15 \times 10^{-5}$ m s^{-1}, corresponds to the sensible heat and can be thought of as the restoring time scale of a mixed layer relaxing to the prescribed temperature; for a mixed layer depth of 30 m this timescale would be of 30 days. The negative sign on the l.h.s of (2.25) means a return towards zero of any surface perturbation temperature. Assuming that the perturbation densities are function of the perturbation temperatures only, $\rho' = -\alpha\rho_0 T'$, and using the relationship in (2.9), equation (2.13) is included as a surface boundary condition for (2.10) and the top boundary condition for the third derivative in the HF case takes the form

$$w_{zzz} = -\mu w_{zz}, \tag{2.26}$$

where $\mu = \tau/K_v$. This would imply a length scale $\mu^{-1} = K_v/\tau$, which for K_v=10^{-4}m^{2}s^{-1} is equal to 10 m and therefore adequately resolved by our 5 m grid spacing. For a smaller diffusivity value, e.g. 10^{-5}m^{2}s^{-1}, the length scale would reduce to 1 m; however, the results have been tested with a 4 and 3 m spacing without changes in the solution.

2.3 Discussion

For selected wavenumbers, the real and imaginary parts of the eigenfrequencies resulted from the solution of the eigensystem (2.10)-(2.13)-(2.22) are plotted for the first twenty least damped modes in Fig.2.1.

Re(σ) (top panels) is not noticeably perturbed by the coupling for any of the first twenty modes, but Im(σ) presents some peculiarities. Besides the intuitive increase in damping rate as we move to higher mode numbers, an unstable mode (Im(σ) > 0) and a slowly decaying mode are present for both selected wavelengths in the EBM case. This is a surprising result, since an instability is not expected to rise from a thermal coupling of this kind and there is no apparent source of energy. Sensible heat exchanges with the atmosphere are expected to provide a sink of energy and therefore an extra damping to the diffusive ocean. Unstable coupled modes need a source from either the ocean or the atmospheric reservoir to release available potential energy. In our simple model there is no mean flow in the ocean nor in the atmosphere and the coupling is given only by thermal exchanges. Mean flows and wind stress are essential factors for developing growing coupled modes through ocean-atmosphere positive feedbacks (Qiu et al., 1997; Goodman and Marshall, 1999; Cessi, 2000; Cessi and Paparella, 2001; Colin de Verdière and Blanc, 2001; Huck et al., 2001). In the model presented here there is no kinetic energy since the basic state is motionless

and no available potential energy in either the ocean or the atmosphere, therefore there is no energy to sustain instabilities.

Interestingly, the slowly decaying mode found in Fig.2.1 is present for the NF and HF case as well, where only losses towards the atmosphere are present, but the growing mode appears only when the EBM is coupled to the ocean. Both Colin de Verdière and Huck (1999) and Huck and Vallis (2001) found interdecadal oscillations in their ocean forced by constant surface heat fluxes but in our simple representation these are not supported under the HF case. However, we can speculate, as discussed later, that the weakly damped mode highlighted before might get unstable under more realistic physical conditions.

A global view of the main results is summarized in Fig.2.2. Here the dispersion relation for the first two baroclinic modes of the linear unperturbed theory is compared with the results from our three alternative surface conditions. None of the simple couplings applied to the planetary wave change its frequencies significantly, and therefore its phase velocities are essentially the same as the linear theory predicts. Some discrepancies from the standard linear theory appear only at very long wavelengths λ_w (around 10^7m, much longer than any observed planetary wave) where greater decaying rates (Im(σ)) are found.

Decay rates are plotted in the bottom panel of Fig.2.2. Here a slow increase in Im(σ) is clear as the wavenumber moves towards longer waves for all three cases. For long wavelengths, the EBM produces the strongest damping, though in a range

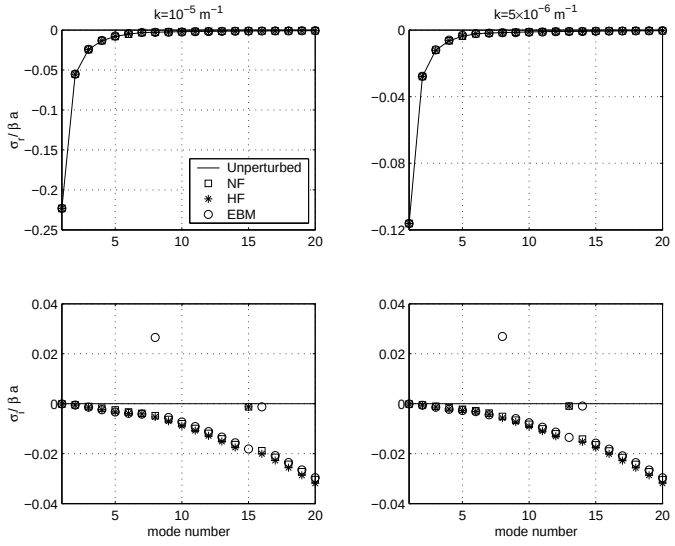

Figure 2.1: *Real and Imaginary parts of the eigenfrequencies for $k = 10^{-5}m^{-1}$ and $k = 5\times10^{-6}m^{-1}$ (NF = no fluxes, HF = heat fluxes and EBM = Energy Balance Model). No differences are found for Re(σ) and only small decays exist for Im(σ). Whilst all the modes resemble each other in the different cases, an unstable mode appears for the EBM and a slowly decaying one for the NF and HF case as well.*

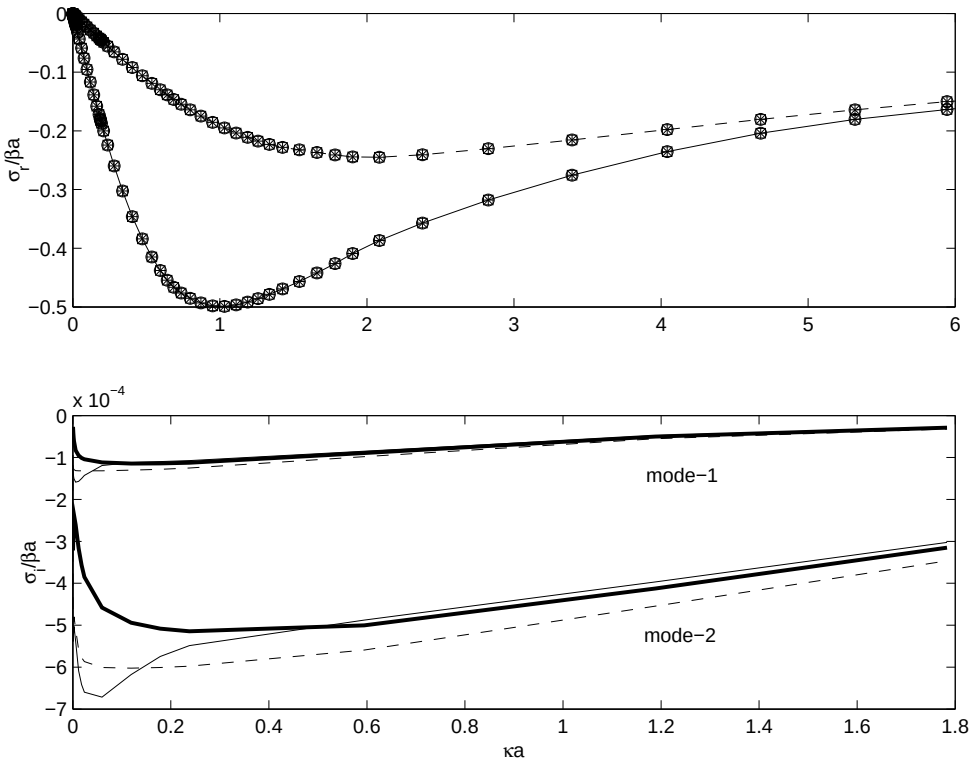

Figure 2.2: *Dispersion relation for the first and second mode for all the three cases studied ($N_0^2 = 10^{-5}s^{-2}$, K_v=$10^{-4}m^2s^{-1}$). The frequency is scaled by $1/\beta a$ and the wavenumber by a. Top panel: real part of the frequency. Solid and dotted lines correspond to the unperturbed solution for the first and second mode respectively.* □ *= diffusivity-only case (NF),* ∗ *= heat flux case (HF),* ∘ *= EBM case. Bottom panel: decaying rate of the first and second mode for the three cases. Thick solid lines = NF, solid lines = HF, dashed line = EBM.*

of λ_w from decadal to annual period ($\lambda_w = 10^6$ - 10^4m), the HF dominates. This was to a certain point predictable as the EBM includes some incoming fluxes that counteract the outgoing fluxes, also included in the HF case. Therefore, the first mode is weakly damped everywhere whereas the second and successive modes are more and more damped. The result is then an insensitivity of the first mode to all these couplings and a small dependence of the following ones.

The vertical structure of the wave is also analysed. The unperturbed nondiffusive solution, together with the results of the different surface conditions, is shown in Fig.2.3 for the first three modes for the stratification considered. The eigenvectors are almost independent of the wavenumber but this is not the case when they become complex. For a wave with $\lambda_w = 6 \times 10^5$m, vertical diffusivity only and the two couplings have negligible effects on the eigenstructure; when we move toward longer waves, the effects are visible from the third mode ($\lambda_w = 6 \times 10^6$m, right panel of Fig.2.3). As anticipated by the dispersion relationship, damping starts to be “felt"

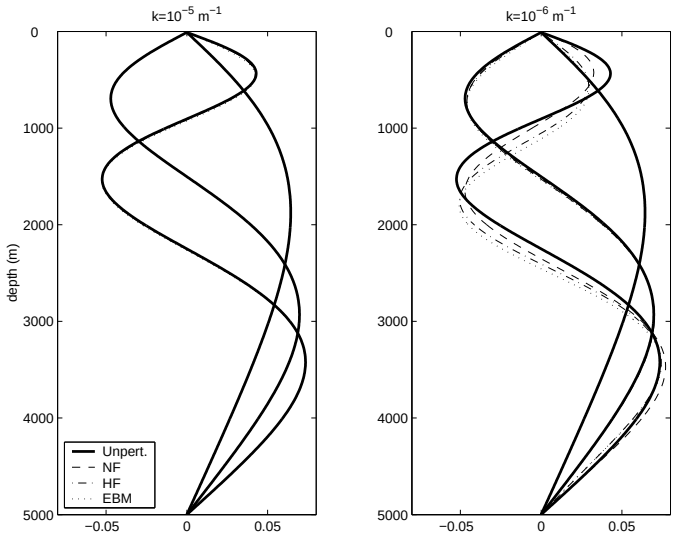

Figure 2.3: *Solutions for the vertical structures of the first three modes for the three cases. Only the third mode at long wavelengths starts being significantly modified.*

at higher modes and longer waves. After computing the solutions for all matchings and looking at different wavenumbers, neither a surface boundary layer nor any significant difference from the linear unperturbed vertical structure could be found in the first mode.

Moreover, no discernible difference was found in the perturbation of the vertical structure from the HF or the EBM coupling. The introduction of unrealistically high K_v ($10^{-3}\mathrm{m}^2\mathrm{s}^{-1}$) into the wave equations is significant in the vertical structure in the second and higher modes, as can be seen for the NF case in Fig.2.4. The dependence of the eigenfrequencies on changes in K_v showed similar results: the real part remains unaffected for all modes while σ_i starts to be perturbed by diffusivity from the second mode if K_v=$10^{-3}\mathrm{m}^2\mathrm{s}^{-1}$ as found for the vertical structure. Therefore, vertical diffusivity only and the coupling through heat fluxes do not slow down the wave or damp it effectively, even with unrealistically high values. This result is in contrast with previous studies, which suggested that planetary waves could be slowed and damped by Newtonian cooling by the atmosphere (White, 2000a). Sensible heat fluxes seem to be the most successful mechanism in damping out the wave; in the EBM, positive contributions of sensible and latent fluxes to the ocean do exist, possibly inducing some positive feedbacks that diminish the net loss to the atmosphere and therefore the damping of the wave.

Since more damping effects are found for the second mode, it is interesting to look at the whole spectrum of modes (Fig.2.1). These are progressively slower and hence they have more time to interact with the overlying atmosphere and, in this case, be damped by heat losses.

Weakly dissipated modes have been recently discussed by Cessi and Primeau

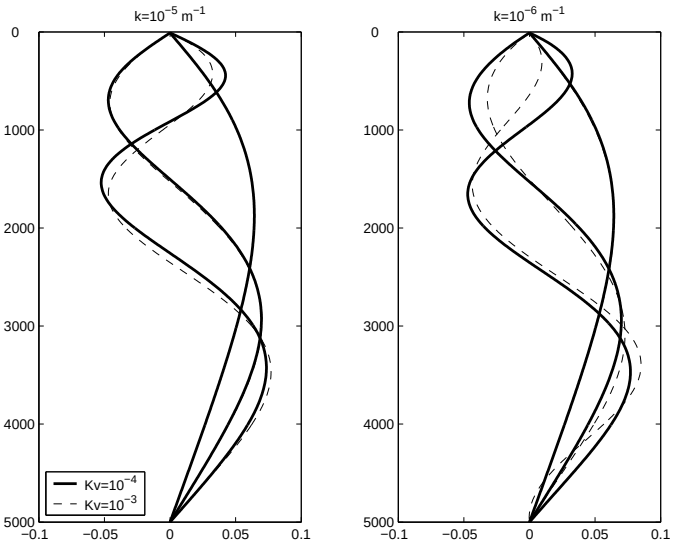

Figure 2.4: *Effects of changes in the diffusivity coefficient on the first three modes for selected wavenumbers in the NF case. When K_v is increased from $10^{-4}m^2s^{-1}$ to $10^{-3}m^2s^{-1}$ the second mode, and for long waves also the third mode, is perturbed. Therefore, the K_v value necessary to modify the vertical structure is too high.*

(2001). Within the free basin modes they found the existence of weakly damped modes promoted by dissipation; moreover, these ocean-only modes can be excited by dynamical air-sea coupling (Cessi and Paparella, 2001). In fact, Jin (1997) discussed a coupled mode that under a moderate thermal damping was weakly damped but when positive coupled feedbacks are acting the mode turns to be weakly unstable. Therefore, while the unstable modes generated by the EBM result from a different process, we hypothesize that the slowly decaying modes found with the NF and HF case could be generated by similar mechanisms as the ones found by Cessi and Primeau (2001), and possibly become sustained by a subsequent atmospheric forcing.

2.4 Structure and growth of the unstable mode

The mode with a positive imaginary part found in Fig.2.1, implying a growing disturbance, exists for a wide range of wavenumbers (Fig.2.5), including the physically significant range. In the longwave limit, the growth rate varies linearly with the wavelength. Its vertical structure resembles that of a first mode, becoming more oscillatory in the vertical as the wavelength decreases; this holds for its imaginary part as well, which is of the same order of magnitude as the real part (Fig.2.6). Clearly this mode arises from the interaction of the wave with the overlying EBM and its incoming energy, the longer the wave the more it interacts with the atmosphere. At the beginning of this chapter we suggested the possibility of a boundary layer arising due to the inclusion of K_v and different matching at the surface, but

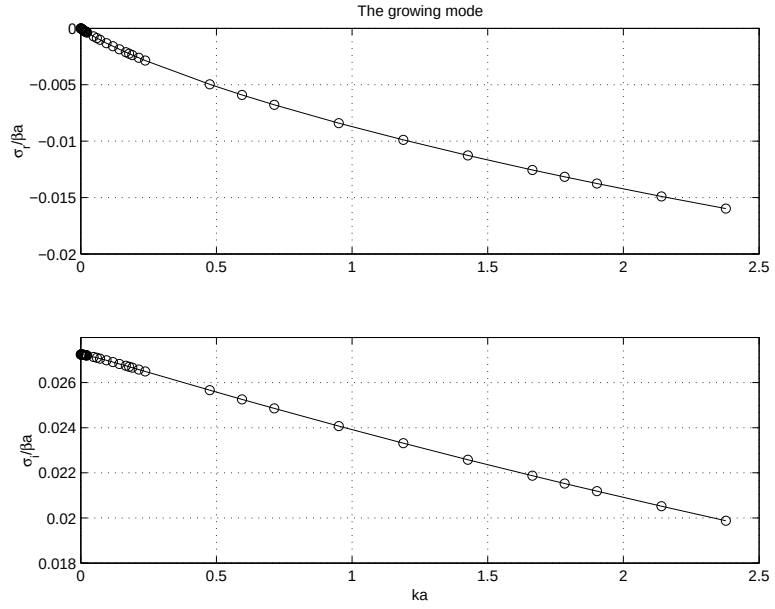

Figure 2.5: *Real part (top) and Imaginary part (bottom) of σ for the unstable mode in the long wave band.*

this was not found for any of the modes. In contrast, this growing mode possess a clear surface boundary layer (Fig.2.6) which deepens as $k \to 0$. We therefore try to predict what the boundary layer should be.

The standard dispersion relation for planetary waves is

$$\sigma = -\frac{\beta k}{(k^2 + l^2) + \frac{1}{a^2}}, \tag{2.27}$$

If $a \sim 25$ km, the long wave approximation is reached from $k \sim 10^{-6} m^{-1}$ and the approximate dispersion relation is $\sigma \approx -\beta k a^2$. Rewriting (2.10) we have

$$N^2\big[\sigma(k^2 + l^2) + \beta k\big]w = -iK_v f^2 w_{zzzz} + \sigma f^2 w_{zz} \tag{2.28}$$

and introducing the approximation for σ

$$N^2\big(-\beta k^3 a^2 + \beta k\big)w = -iK_v f^2 w_{zzzz} - \beta k a^2 f^2 w_{zz} \tag{2.29}$$

Finally, since $-\beta k^3 a^2 \ll \beta k$ we get

$$\beta k N^2 w = -iK_v f^2 w_{zzzz} - \beta k a^2 f^2 w_{zz} \tag{2.30}$$

or

$$\underbrace{\beta k N^2 w}_{A} = \underbrace{\frac{-iK_v f^2 w}{\delta^4}}_{B} - \underbrace{\frac{\beta k a^2 f^2 w}{\delta^2}}_{C} \tag{2.31}$$

In the boundary layer, the 4-th order term (w_{zzzz}) balances the 2-nd order term (w_{zz}) and the relation $B \sim C$ must hold. This is

$$K_v f^2 w \sim \beta k a^2 f^2 w \delta^2$$

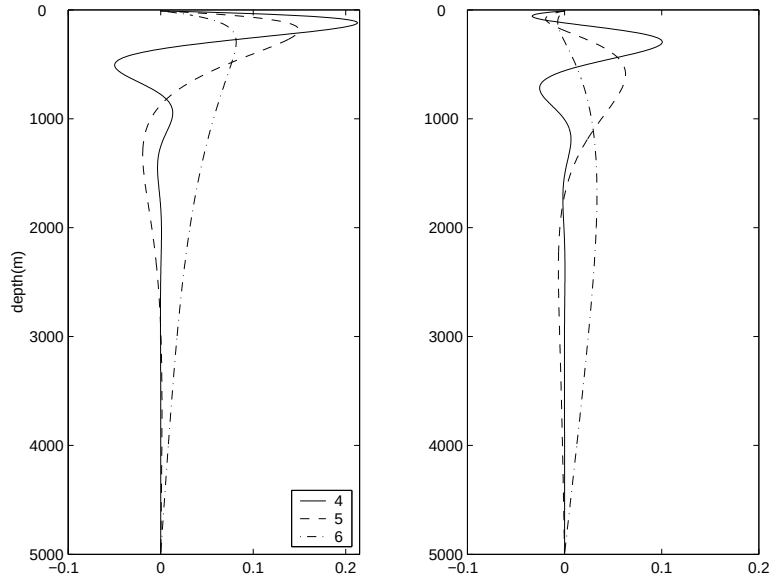

Figure 2.6: *Vertical structure of the growing mode. Re(w) (left panel) and Im(w) (right panel). Solutions are plotted for $k = 10^{-4}$, 10^{-5}, $10^{-6} m^{-1}$. Note how the boundary layer thickness is linearly increasing with k.*

Therefore with the introduction of K_v into the long wave equations, the dependence of the boundary layer thickness δ on diffusivity would be described by

$$\delta \sim \frac{1}{a\sqrt{\beta}} \left(\frac{K_v}{k} \right)^{1/2} . \tag{2.32}$$

The resulting boundary layer thickness can be predicted and some examples are calculated below:

$$\delta \sim \begin{cases} 300m. & , \quad k = 10^{-7} m^{-1} \\ 140m. & , \quad k = 5 \times 10^{-7} \\ 100m. & , \quad k = 10^{-6} \end{cases} \tag{2.33}$$

This would give a δ of about 200m for $\lambda = 6 \times 10^6$m, which is roughly what we obtain in the growing mode. Also, after computing the vertical structure for several k, it was observed that the decay of δ towards smaller wavelengths is linear and therefore contradicting the previous relationship. However, (2.32) would describe a boundary layer for a no heat flux condition where (2.14) holds; in this case the EBM needs to be present for the unstable mode to exist, therefore the theoretical behaviour of δ is expected to be different from the one found here.

The other singular mode, the slowly-decaying one, has a bottom trapped structure and no particular changes are found when the air-sea coefficient λ or K_v vary, as only the surface trapped growing mode will be sensitive to changes at the surface.

2.4.1 Parameter sensitivity

In order to understand the response of this unstable mode to changes in the background conditions we carried out sensitivity analyses on the main parameters that could control the ocean-atmosphere interaction.

As the selected value for the stratification is slightly weak ($N_0^2 = 10^{-5}\mathrm{s}^{-2}$) we studied the eigenresponse to an increase in the ocean stratification. In Fig.2.7 the decaying rates for different N_0^2 are plotted. The growing rate diminishes and the unstable mode is shifted towards higher modes, indicating that a lower frequency is needed to interact positively with the EBM. The same happens for the slowly decaying mode and for both wavenumbers ($k = 5 \times 10^{-6}\mathrm{m}^{-1}$, $k = 10^{-5}\mathrm{m}^{-1}$). At the same time, with stronger stratification the response is more concentrated in the surface layer and more oscillations in the vertical start to appear (Fig.2.8). Interestingly, surface intensified unstable modes have also been found by Huck et al. (2001) in their three-dimensional dynamical ocean model forced by constant surface fluxes. Their unstable mode, studied in the framework of quasigeostrophic baroclinic instability and identified as potential vorticity waves (a kind of planetary waves), relied on the background flow in order to propagate. In our case such a mode could not exist, lacking our model of a circulation on which the unstable wave could grow. In our study, with an exponential profile for the Brunt-Väisälä frequency, the mixed layer is not represented. Since the heat exchanges with the atmosphere are concentrated at the surface, the inclusion of a mixed layer could be important. Therefore, we studied the case of an exponentially stratified ocean with an homogeneous mixed layer

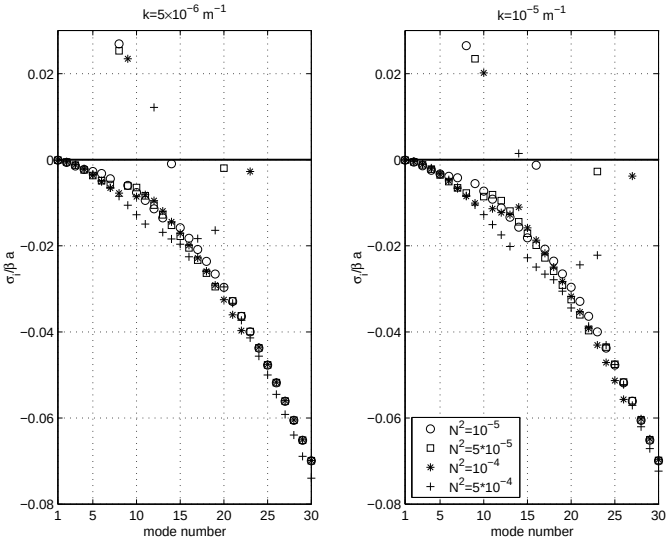

Figure 2.7: *Responses of the decaying rate to changes in N_0^2 (s^{-2}). As the exponential stratification increases the unstable mode is displaced toward higher modes and its growth rate becomes smaller. The same is happening for the slowly decaying mode which is approaching the other modes. Note how shorter waves are more sensitive to changes in N_0^2.*

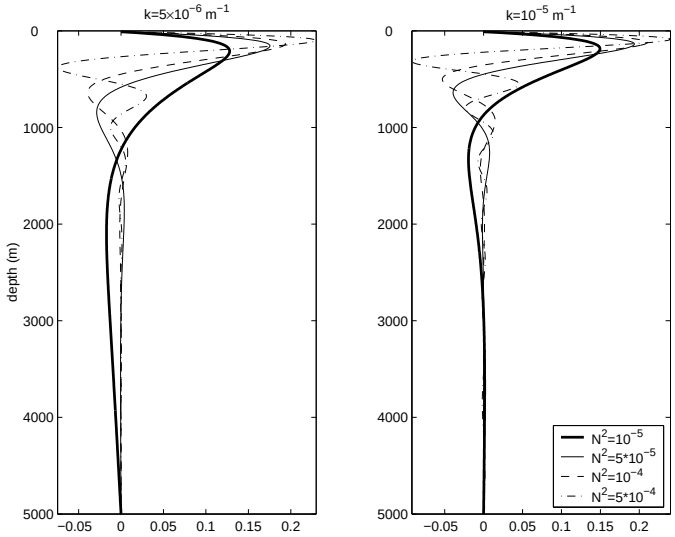

Figure 2.8: *Structure of the unstable mode at different stratifications (s^{-2}). With stronger N_0^2 the mode is trapped at the surface with more oscillation in the vertical.*

at the top. In this case, we used the same exponential stratification $N^2 = N_0^2 e^{-\gamma z}$ (where again $N_0^2 = 10^{-5}$ s^{-2} and $\gamma = 3.7$) and introduced an homogeneous layer of different thickness δ at the surface, i.e.

$$N^2 = \begin{cases} 0 & , \quad -\delta \leq z \leq 0 \\ N_0^2 e^{-\gamma z} & , \quad -H \leq z \leq -\delta \end{cases} \tag{2.34}$$

Applying the same boundary conditions for the coupling and using values ranging 300 m $\leq \delta \leq$ 0 m, no significant differences were found, apart from similar changes obtained when N_0^2 is modified (not shown). The unstable mode is still present indicating that the heat exchanges at the surface are rapidly transmitted into interior of the ocean and the homogeneous mixed layer is not able to modify the wave response. Also, introducing the homogeneous surface layer in the stratified ocean did not change the characteristics of the internal wave propagation, resulting in similar wave speeds and vertical structure.

Another fundamental parameter is the coefficient of air-sea exchange λ, which is included in λ_{sa}, λ_{so}[3]. An increase in λ would mean a stronger communication between the wave and EBM leading to an excitement of the coupled unstable mode. This is clearly seen in Fig.2.9 when λ is changed from its original standard value of 20 W m^{-2} K^{-1}. All modes react to a smaller value of λ (which is the way to separate the wave from the overlying atmosphere and recover the ocean-only solution) but only the unstable mode is sensitive to greater values, being the direct consequence of the coupling. Clearly, λ is a necessary condition for the existence of the coupled

[3]For a clear derivation of equations (2.15)-(2.16) and the relationship between λ and λ_{sa},λ_{so}, see Appendix A in BB98.

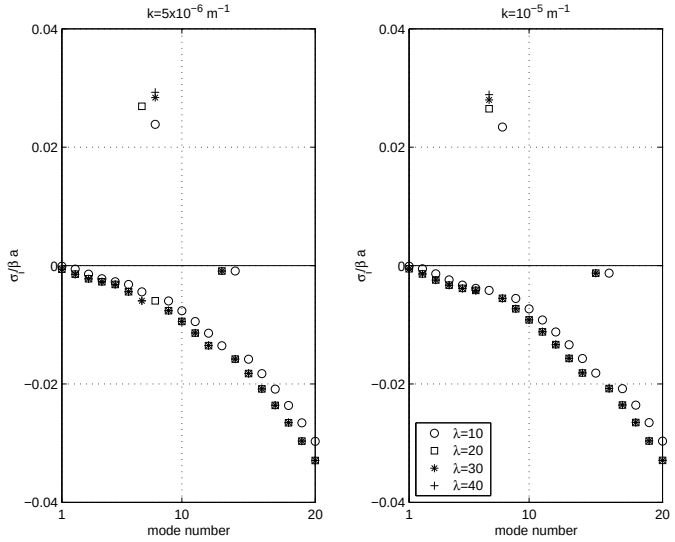

Figure 2.9: *Same as Fig.2.7 for changes in λ. The growing mode responds to an increase or decrease in the air-sea exchange but not dramatically. In contrast, the slowly decaying mode is less affected.*

mode but it is not controlling its growth rate as strongly as the existent stratification. Also, the vertical unstable eigenmodes at different values of λ are not shown as no significant modifications are found for changes in the air-sea coefficient.

The weak effect of changes in the exchange coefficient was also demonstrated in Huck et al. (2001) when using a vertical diffusivity of $10^{-4}\mathrm{m}^2\mathrm{s}^{-1}$; in their planetary geostrophic model coupled to an atmospheric EBM they found no dependence of the variability of the system by varying the air-sea exchange coefficient within a range of 10-60 W $\mathrm{m}^{-2}\mathrm{K}^{-1}$.

The last parameter subject to study is the vertical diffusivity. The existence of K_v is crucial to the transmission of the information received at the surface to the ocean interior and, although it did not affect the properties of the modes, it is expected to control the behaviour of the unstable mode due to the boundary layer at the top.

In Fig.2.10 the solution for different values of K_v is represented (top panels) and the vertical structure of the unstable mode is also given (bottom panels). As diffusivity increases the unstable mode appears at low mode numbers, reaching its maximum growth for a diffusivity of 3-4$\times10^{-5}\mathrm{m}^2\mathrm{s}^{-1}$. Then the growth rate of the unstable mode gradually decreases until it becomes zero for a value of K_v=5-4$\times10^{-4}\mathrm{m}^2\mathrm{s}^{-1}$ for the two wavelengths considered. While the mode is being destroyed its vertical structure is slowly modified until it becomes a third or fourth mode, coherent with the frequency trajectory. The coupled mode, strongly influenced by K_v, is extremely slow with a timescale of $\sim$100 years but has a growth rate of $\sim$10 years. This might be interesting in studies concerning climate variability, in which timescales are of the order of a hundred years.

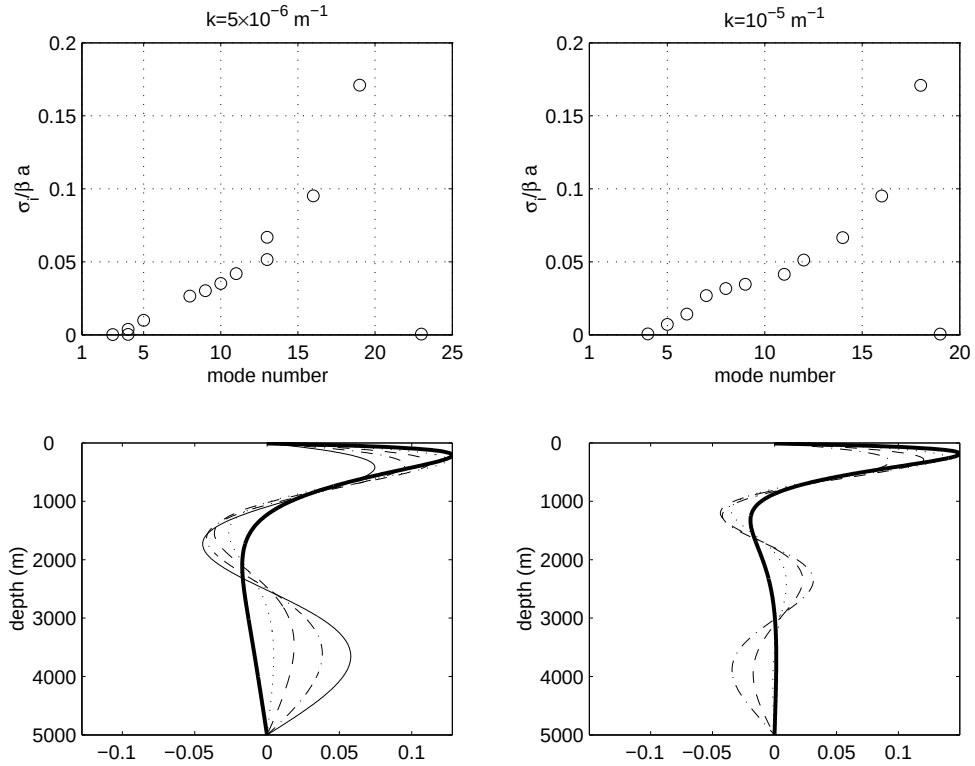

Figure 2.10: *The dependence of the unstable mode to diffusivity. The position of the mode is shown in the top panels from $K_v = 2 \times 10^{-5}$ (the first value at which the unstable mode appears) to $K_v = 5 \times 10^{-4}$ for $k = 5 \times 10^{-6}$ and $K_v = 4 \times 10^{-4}$ for $k = 10^{-5}$ (the last value of diffusivity supporting the mode). As K_v increases from its critical value the mode is rapidly destroyed and reenters the decaying curve of modes. For $k = 5 \times 10^{-6} m^{-1}$ the final position is the third mode and for $k = 10^{-5} m^{-1}$ the fourth mode . This trajectory is reflected in the vertical structure of the bottom panels (thick solid line = $K_v = 10^{-4}$, thin solid line = last vertical structure for which $\sigma_i > 0$).*

Moreover, the unstable mode possesses a vertical structure typical of a first, second or third mode, depending on the wavenumber (Fig.2.6). Also, when tested with different values of K_v, it rapidly moved to the fourth and even third position of the eigenspectrum (Fig.2.10), adjusting its vertical shape to the modal ordering. What seemed an unimportant mode, far from the first two or three eigenfrequencies, and therefore not likely to play a major role when more complicated physics is added in the ocean, is now a mode that, under certain parameters values, reaches the higher eigenfrequencies and *looks* like one of them.

This mode could be misleading if identified as a first or second mode and we need to know more about its behaviour. Therefore, it is interesting to study in detail its time dependent solution with the help of an initial value problem.

2.4.2 The time-dependent solution

We here examine briefly the time-dependent solution of the unstable EBM mode. The initial value problem of the damped eigenmodes is not of any particular interest in this case; as predicted by the eigenanalysis, all of them are slowly decaying in time with stronger damping rates for higher modes. However, the behaviour of the unstable mode during a cycle will inform us about its vertical structure evolution and how its boundary layer grows. The time-dependent problem will also be useful in corroborating the previous numerical solution.

From (2.1)-(2.5) the time dependent equation reads

$$\left(\partial_t - K_v\partial_z^2\right) f^2 w_{zz} = \left[(k^2+l^2)\partial_t - ik\beta\right] N^2 w, \tag{2.35}$$

which can be rewritten in the condensed form

$$\partial_t \mathcal{L}(w) = \mathcal{M}(w) \tag{2.36}$$

where the linear operators are $\mathcal{L} = f^2\partial_z^2 - N^2(k^2+l^2)$ and $\mathcal{M} = K_v f^2 \partial_z^4 - ik\beta N^2$. The problem was time stepped using the semi-implicit Crank-Nicholson scheme, which is unconditionally stable and second order in space and time. The initial condition is the solution found with (2.10) with a different boundary condition at the top for every case and every mode.

The time stepped EBM involves the system (2.17)-(2.18). In our simplified model we will neglect the effects of salinity and consider density perturbations driven only by temperature perturbations, i.e. $\rho = -\rho_0 \alpha T$ (where $\alpha = 10^{-4}K^{-1}$ is the coefficient of thermal expansion of seawater). Then the initial conditions can be expressed as

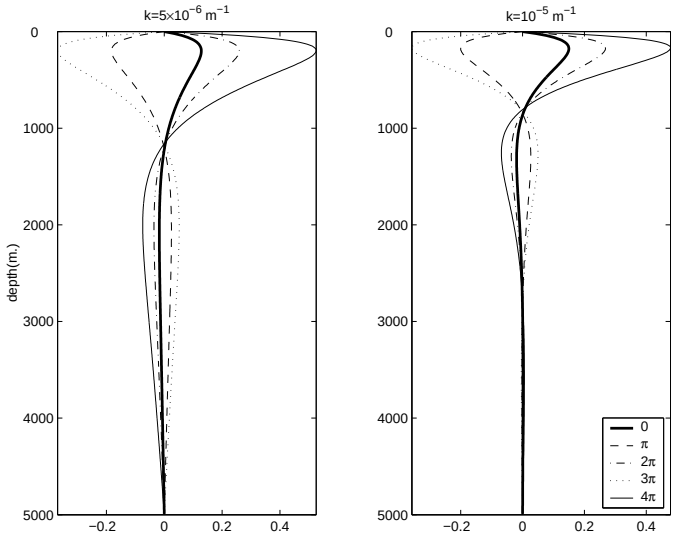

Figure 2.11: *Time dependent solution after two cycles for the real part of the growing modes of Fig.2.1.*

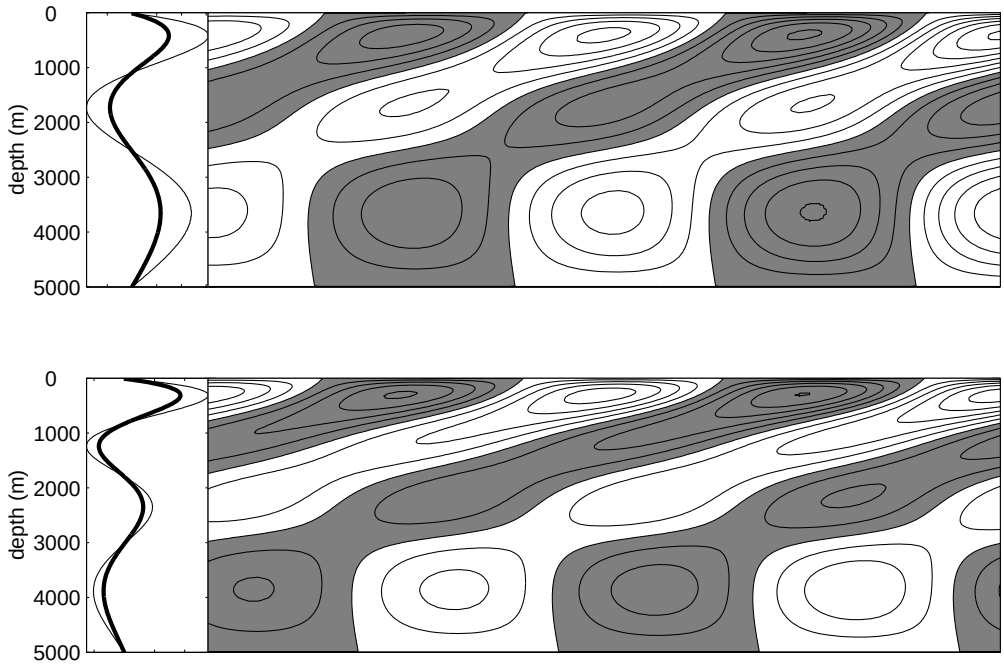

Figure 2.12: *Time dependent solution after two cycles for the real part of the slowest growing modes of Fig.2.10 (top: $k = 10^{-5}m^{-1}$, bottom: $k = 5 \times 10^{-6}m^{-1}$). Left panels: thick line = initial state, thin line = final state. Right panels: evolution of Re(w) during the two cycles integration. The contour interval is 0.025. Negative contours are shaded.*

(from (2.9)):

$$T_o = \frac{-if^2}{\alpha g(\sigma k^2 + \beta k)} w_{zz} \tag{2.37}$$

$$T_a = \lambda_o T_o - \Gamma_o^{'} \partial_z T_o. \tag{2.38}$$

and the time stepped expression for the atmospheric temperature is

$$\partial_t T_a = \frac{\lambda_{sa}}{\gamma_a} w_{zz}|_{top} - \frac{\lambda_{sa} + \lambda_a}{\gamma_a} T_a \tag{2.39}$$

In order to solve the problem numerically, the integration for T_a is included in the time stepped matrix system, therefore the problem $\partial_t w = \mathsf{A}^{-1}\mathsf{B}w$ becomes of order $N + 1$.

The time stepped solution of the unstable modes found in the eigenanalysis can be seen in Fig.2.11. After two cycles they grow as predicted by their σ_i and so appear more and more surface intensified. In Fig.2.12 the growing modes for $k = 5 \times 10^{-6}\mathrm{m}^{-1}$, top panel, and $k = 10^{-5}\mathrm{m}^{-1}$, bottom panel, with the smallest growing rate are plotted ($K_v = 4 \times 10^{-4}$ and $K_v = 3 \times 10^{-4}$ $\mathrm{m}^2\mathrm{s}^{-1}$ respectively for $N_0^2 = 10^{-5}\mathrm{s}^{-2}$) confirming their third and fourth mode vertical structure. Therefore, this growing solution is robust, as a large K_v coefficient is needed to destroy it, even though the stratification is rather weak in this case.

The solution given by this initial value problem proves the existence of an unstable mode, which is travelling very slowly but growing at the decadal period, present for every wavenumber and sustained by the interaction with the atmospheric EBM. However, the reasons for the existence of this mode are still unclear as is the origin of the energy necessary for its growth. A brief discussion of energetics is given in the next section.

2.4.3 Energetics

In the simple case of constant N^2, some progress can be made towards identifying the source of the instability. We construct a kinetic energy equation by multiplying (2.1) and (2.2) by $\rho_0 u$ and $\rho_0 v$ respectively, adding and integrating over a horizontal wave cycle and depth. To this is added the potential vorticity equation, obtained by multiplying (2.5) by $g^2\rho/\rho_0 N^2$. The terms in w cancel, leaving

$$E_t \equiv \frac{\partial}{\partial t}\frac{1}{2}\int_{-H}^{0}\left[\rho_0(u^2+v^2)+\frac{g^2\rho^2}{\rho_0 N^2}\right]dz = \\ = \frac{K_v g^2}{\rho_0}\int_{-H}^{0}\frac{\rho\rho_{zz}}{N^2}dz. \tag{2.40}$$

The r.h.s. cannot be further simplified in general, except when the background stratification is uniform. In that case, integrating by parts,

$$E_t = \frac{K_v g^2}{\rho_0}\left\{\left.\frac{\rho\rho_z}{N^2}\right|_{z=0} - \int_{-H}^{0}\frac{\rho_z^2}{N^2}dz\right\}. \tag{2.41}$$

The second term is negative definite (the diffusion acting as an energy sink) and the first term can only have a contribution at the surface by (2.14). In all the cases considered here except the EBM case, the surface contribution is identically zero, and the system energy can only decrease with time, indicating damped solutions.

In the EBM case, however, the potential energy in the EBM atmosphere must also be considered. To obtain this, take (2.17), with the l.h.s. converted back to $\gamma_a T_{at}$, multiply by λ_{so}, and add λ_{sa} times (2.18), which eliminates the first terms on the r.h.s., to obtain

$$\gamma_a\lambda_{so}T_a T_{at} + \gamma_o' K_v\lambda_{sa}T_o T_{oz}|_{z=0} = \\ = -\lambda_{so}(\lambda_{sa}+\lambda_a)T_a^2 + \lambda_{sa}(\lambda_{so}+\lambda_o)T_o^2. \tag{2.42}$$

Converting ocean temperature to density perturbations through $\rho = -\rho_0\alpha T$, this becomes

$$\frac{\gamma_a\lambda_{so}\rho_0\alpha^2 g^2}{\gamma_o'\lambda_{sa}N^2}T_a T_{at} + \frac{K_v g^2}{\rho_0 N^2}\rho\rho_z|_{z=0} = \\ -\frac{\lambda_{so}(\lambda_{sa}+\lambda_a)\rho_0\alpha^2 g^2 T_a^2}{\gamma_o'\lambda_{sa}N^2} + \frac{(\lambda_{so}+\lambda_o)g^2\rho^2|_{z=0}}{\rho_0\gamma_o' N^2} \tag{2.43}$$

so that a total energy equation is found by adding (3.1):

$$E_t + \frac{\gamma_a \lambda_{so} \rho_0 \alpha^2 g^2}{\gamma'_o \lambda_{sa} N^2} T_a T_{at} = -\frac{K_v g^2}{\rho_0} \int_{-H}^{0} \frac{\rho_z^2}{N^2} dz - \\ - \frac{\lambda_{so}(\lambda_{sa} + \lambda_a)\rho_0 \alpha^2 g^2 T_a^2}{\gamma'_o \lambda_{sa} N^2} + \frac{(\lambda_{so} + \lambda_o) g^2 \rho^2|_{z=0}}{\rho_0 \gamma'_o N^2}. \tag{2.44}$$

The l.h.s. is a time derivative of a positive definite (quadratic) quantity, and the r.h.s. consists of negative terms apart from the last, which is positive definite. This term, if sufficiently large, can permit growth of the solution as observed. After performing an eigenanalysis for the case in which the stratification is constant we use the numerical results to evaluate the three terms in the total energy equation (2.44). We are then able to compare the positive term against the other two for the decaying and the growing modes.

In the first mode solution the negative terms are greater than the positive term indicating a total sink of energy. In the case of the growing mode, the positive term is larger than both decaying terms and the r.h.s. of (2.44) is positive, confirming an increase in the energy of the system. Also, the energy loss of the decaying modes is much smaller than the energy inputs of the growing modes, confirming again the previous results of growth rates greater than the decaying rates of the first modes.

Moreover, we emphasize the dependence of the first term in (2.44) upon K_v. Since the first term is the largest of the negative terms, it will play a major role in balancing the energy conservation against the growing term. Therefore, an increase in the vertical diffusivity coefficient is likely to rapidly counteract the third term as previously observed.

These results are summarised in Table 1 where the total energy budgets of the cases depicted in Fig.2.10 are shown. Only the first two damped modes and the unstable mode are analysed. The values of the three terms in (3.4) are given as a percentage of the total budget, being the first two negative contributions and the third a positive contribution. It is clear how the first term (involving vertical diffusivity) and the third term (the positive contribution) are dominating the budget at all parameters values. In the case of decaying (unstable) modes, the diffusivity (positive) term is responsible for the energy of the system. Also, the term allowing growth gets weaker with stronger stratifications and bigger diffusivities, which is in agreement with the results shown in Fig.2.7 and Fig.2.10. The position of the unstable mode within the damped modes is shifting depending on the parameters values (as pointed out in the parameter sensitivity analysis) and, because of the uniform stratification, is always located at higher position than in the exponential case, but always present.

Table 2.1: *Energy budget analysis for different wavenumbers k, vertical diffusivity K_v and constant stratification ${N_0}^2$. The three terms in eq.2.44 are denoted by t1, t2, t3, respectively. Note that the first two are negative while the third is positive. The values of each term are given as a percentage of the total energy budget. Shown are the first two damped modes and the unstable mode for every case. The position of the unstable mode varies as the parameters in eq.3.4 vary and is not directly comparable with the exponential stratification. The values of the parameters are chosen accordingly to Fig.2.10; for each wavenumber, we computed the budget for the least growing modes ($k = 5 \times 10^{-6}$: $K_v = 5 \times 10^{-4}$ and $K_v = 4 \times 10^{-4}$; $k = 1 \times 10^{-5}$: $K_v = 4 \times 10^{-4}$ and $K_v = 3 \times 10^{-4}$ for ${N_0}^2 = 10^{-5}$) and also shown is an example of change in the background stratification ($k = 5 \times 10^{-6}$: $K_v = 4 \times 10^{-4}$ and ${N_0}^2 = 10^{-4}$; $k = 1 \times 10^{-5}$: $K_v = 3 \times 10^{-4}$ and ${N_0}^2 = 10^{-5}$).*

		$k = 5 \times 10^{-6}$			$k = 1 \times 10^{-5}$		
		$K_v = 5 \times 10^{-4}$	$K_v = 4 \times 10^{-4}$	${N_0}^2 = 10^{-4}$	$K_v = 4 \times 10^{-4}$	$K_v = 3 \times 10^{-4}$	${N_0}^2 = 10^{-4}$
mode 1	% t1	97	98	99	98	96	99
	% t2	1	1	1	1	1	1
	% t3	2	1	0	1	3	0
mode 2	% t1	96	96	99	97	92	97
	% t2	1	1	1	1	2	1
	%t3	3	3	0	2	7	2
unst. mode	% t1	15	11	26	13	5	28
	% t2	1	1	1	1	1	1
	% t3	84	88	73	86	94	71

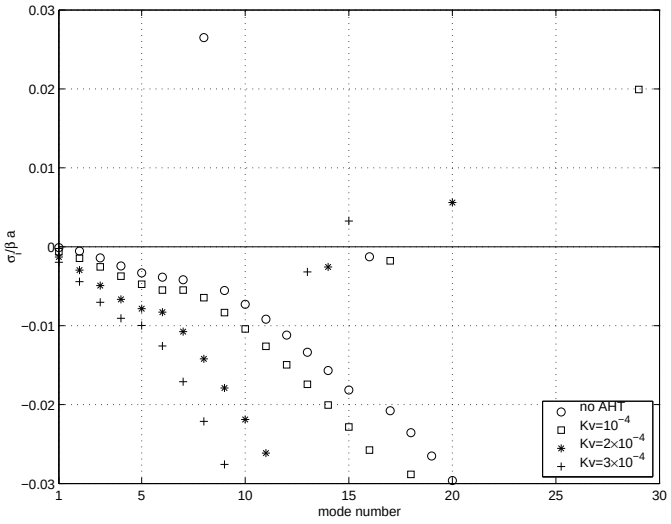

Figure 2.13: *The effects of the inclusion of horizontal atmospheric heat transport (AHT) at different vertical diffusivities for* $k = 10^{-5}m^{-1}$. *Also plotted is the result with no AHT at* $K_v = 10^{-4}m^2s^{-1}$ *(circles).*

2.4.4 The effects of atmospheric heat transport

We proved that when the EBM is coupled to the planetary geostrophic model the energy balance might be positive, generating an instability and explaining the results of the eigenmode analysis. However, this is not physically correct and therefore there must be a missing term in the energy budget able to counteract those positive contributions from the EBM and give a final damped solution.

So far, we have considered a one-dimensional model, with the spatial dimension represented by a point at midlatitudes (30^0N). Barsugli and Battisti (1998) neglect any meridional variability in both atmosphere and ocean, but atmospheric heat transport (AHT) is an important and effective damping of sea surface temperature anomalies (Pierce et al., 1996). We consider here the effects of eddy-diffusive horizontal heat transport in the atmosphere in its usual parameterization

$$\gamma_a \nabla \cdot (\nabla K_T T_a),$$

where again $\gamma_a = \rho_a C_{pa} H_a$ is the atmospheric heat capacity and K_T is the heat transport coefficient. For our model we neglect any meridional dependence in K_T and set it to $10^6 \mathrm{m}^2\mathrm{s}^{-1}$ as suggested by Huck et al. (2001). Fanning and Weaver (1996) points out that the assumption of diffusive transport is valid only for length scales bigger than 10^6 m, we therefore set the new meridional wavenumber to its minimum. Fig.2.13 shows the results for the eigenanalysis of the system where the eigenfrequencies for a selected wavenumber are compared with the previous solution without AHT at different values of vertical diffusion. The additional damping effect is clear for all modes, the unstable mode is weaker and shifted towards higher modes and the effect of K_v in damping the instability is even stronger; however the growing

mode is still present and has the same behaviour as when the AHT is missing. Moreover, calculations with different wavenumbers (both zonal and meridional) did not reveal significant differences. The introduction of horizontal diffusion in the atmosphere will imply an extra term in (2.23) but this term, together with the second term on the r.h.s., is small compared to the others and therefore does not cause any major modifications in the coupling. Applying (2.23) with no AHT and also removing the second term showed that the ocean response is not crucially dependent on the term involving the frequency and in fact the coupled growing mode maintains a growth rate fairly constant across a wide range of horizontal wavenumbers.

We conclude that, although the AHT is indeed a strong damping mechanism, and together with particular coefficients of diffusivity and stratification can diminish the growth rate, is not sufficient to balance the positive terms involved in the coupling and further physics should be included in order to compensate the mechanisms generating the unstable mode.

2.5 Conclusions

This chapter has examined the behaviour of an oceanic planetary geostrophic model coupled to an atmosphere through an EBM, by examining wave modes with a suitable boundary condition for the vertical velocity in the long wave limit for a continuously stratified, diffusive, ocean. En route, we have examined the effects on long wave motions of the diffusivity itself, and several boundary conditions.

The introduction of vertical diffusion has proved to have little effect on the propagation of planetary waves. Qiu et al. (1997) pointed out that the phase speed of the free wave remains unaltered by the inclusion of eddy processes and is also weakly sensitive to changes of its value, but horizontal diffusion can effectively damp the wave. The NF and HF case are both unable to modify the wave phase speed and also produce small damping rates for the first modes.

The introduction of sensible heat fluxes, and therefore a net loss towards the atmosphere, resulted in only small increase in the damping rates (Fig.2.2, bottom panel). Again, the first three modes seem to remain unchanged. However, this seems to be the more efficient way of damping the planetary wave. When the EBM is introduced, smaller damping rates are found and variations from the unperturbed theory are even less then in the diffusivity case. This is due to the positive contributions of sensible and latent fluxes towards the ocean.

However, when an EBM is used, an additional unstable mode is found. Robust to any change in the parameters, it presents a boundary layer due to the presence of

diffusion and a decadal growth rate, but its extremely long period (about a hundred years), while probably irrelevant for decadal processes, is clearly of importance in the interpretation of long climate model runs using a simplified atmosphere. The shape of the unstable mode resemble that of a first mode (no zero-crossings in the vertical). This means that the unstable mode found when an atmospheric EBM is coupled to a continuously stratified ocean is not negligible in those parameter settings and could be found with a simpler ocean of fewer layers. Also, its existence has been tested within an initial value problem which proved its growing behaviour.

The sensitivity of the unstable mode to the different parameters taken into account is thoroughly explored. The background stratification has been modified, an homogeneous mixed layer has been included at the surface and a possible range of the coefficient of air-sea exchange λ was used without successfully destroying the instability. Moreover, as K_v seemed to be the main factor in controlling the vertical eigenvectors and growth rate of the unstable mode, we computed the growth rate with a larger range of diffusivity values (Fig.2.14) and the unstable mode was found to exist for a relatively wide range of parameter space. When $K_v \to 0$, the ocean and atmosphere stop communicating, or the atmospheric information is not transmitted into the interior ocean; as a result of this, the growing mode cannot exist, and for significant wavelengths, the critical point appears to be at $K_v = 10^{-5}\mathrm{m}^2\mathrm{s}^{-1}$. When K_v reaches its critical value, the bifurcation takes place and the unstable mode appears with a growth rate close to the annual period. Then, as diffusivity increases, the mode is slowly destroyed (as shown in Fig.2.10) and its growth rate slows down until it becomes a decaying mode. In fact, the surface intensified disturbance generated by the EBM is rapidly distributed vertically for higher K_v values and the unstable mode no longer exists; this happens for the bottom intensified mode as well. It is difficult to give a realistic value for midlatitude diapycnal diffusivity. Munk and Wunch (1998), revisiting older studies, concluded that $10^{-4}\mathrm{m}^2\mathrm{s}^{-1}$ is the necessary averaged diffusivity, but other studies using direct estimates at midlatitudes suggest a lower value of $10^{-5}\mathrm{m}^2\mathrm{s}^{-1}$ (Ledwell et al., 1998). General revisions of the problem (see for example Webb and Suginohara (2001)) indicate a range between $3\text{-}5\times10^{-5}\mathrm{m}^2\mathrm{s}^{-1}$.

Within this range, our unstable mode has a decadal growth rate. If we increase the weak stratification to $N_0^2 = 5\times10^{-5}\mathrm{s}^{-2}$ and look for waves with $\lambda_w = 10^{-6}\mathrm{m}$, we find a phase speed corresponding to a decadal period (denoted by a star in Fig.2.10).

So far, unstable modes in the extratropics have been identified where a dynamical coupling is present in the ocean-atmosphere system (Liu, 1993; Jin, 1997; Frankignoul et al., 1997; Talley, 1999; Goodman and Marshall, 1999; Ferreira et al., 2001), or when the ocean model is coupled to the atmosphere through an EBM with no wind forcing (Huck et al., 2001), but in this case the instability relied on the

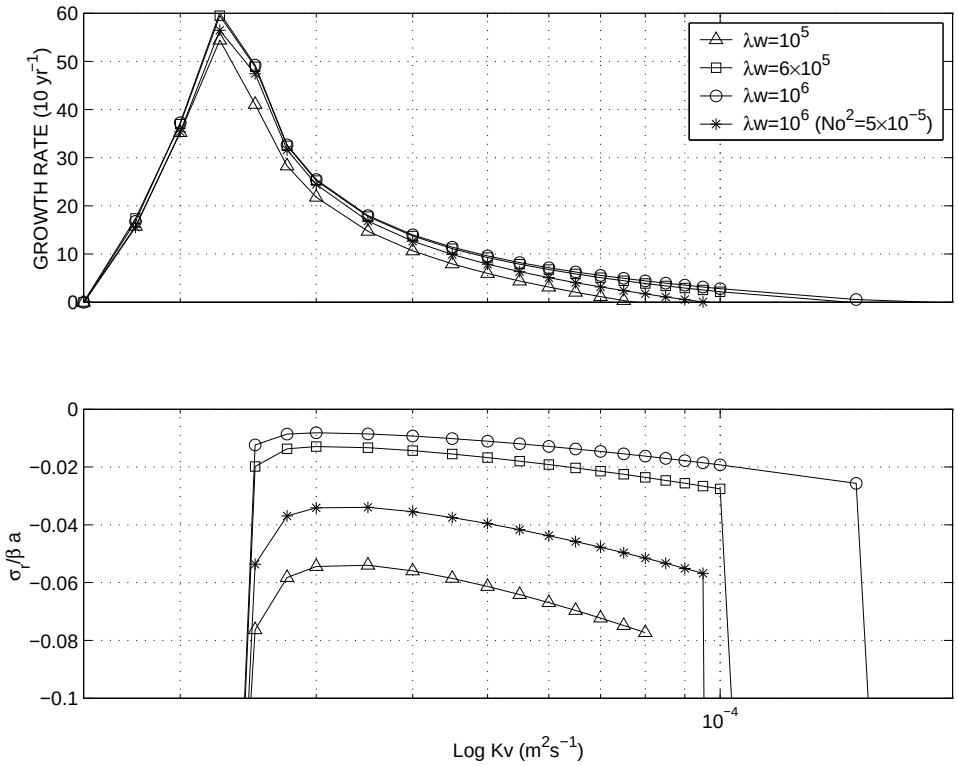

Figure 2.14: *Semilog plot of the growing rate (top) and Re(σ) (bottom) relation with vertical diffusivity for different wavelengths λ_w (m). When $K_v = 10^{-5} m^2 s^{-1}$ the growing mode appears; its growth rate rapidly increases and then slowly vanishes as K_v approaches values around $10^{-4} m^2 s^{-1}$ depending on λ_w. For K_v between 4×10^{-5} and $10^{-4} m^2 s^{-1}$ the growth rate is decadal. Note that for $\lambda_w = 10^6 m$ and $N_0^2 = 5 \times 10^{-5} s^{-2}$ (denoted by a $*$) also the period of the growing mode is decadal in that region.*

zonal background flow to grow, which is not present in our model.

In order to understand the origin of the unstable mode we studied the energetics of the system and identified a positive term that, in the case of the growing mode, is greater than the remaining negative terms and justifies the instability. The simplified atmosphere was improved with the inclusion of horizontal diffusion of heat without achieving a sufficient damping.

It is not clear whether the atmospheric EBM alone could support coupled modes or if this result is an artifact generated by the simplified atmosphere employed, raising doubts over the use of EBMs in coupled studies. Moreover, if dynamics is included in the atmospheric part of the model and the EBM retained, this unstable mode could still be present and possibly confused with a dynamically generated coupled mode.

It might be argued that the use of a constant vertical diffusivity in our ocean could be a lack of representation of the vertical fluxes generated by the EBM, but

the results obtained with different N_0^2 and with an explicit mixed layer at the top seem to indicate that the fluxes are not constraint to the top layer but rapidly transmitted to the interior of the ocean, making the use of a constant K_v a reasonable approximation.

However, our model is oversimplified. The lack of dynamics in both the atmosphere and the ocean, horizontal diffusion and meridional boundaries are big limitations in the results obtained in this study. For instance, mean flows are key factors for the development of positive ocean-atmosphere feedbacks (Qiu and Jin, 1997, for example), meridional boundaries have been proved to cancel the existence of growing modes existing in channel configurations (Goodman and Marshall, 2003), and finally horizontal diffusion, as discussed by Qiu et al. (1997), although not able to modify the phase speed, is a crucial mechanism for the dissipation of planetary waves and among the primary sinks of energy in the ocean. But our model is also missing the positive feedback of wind-stress, which can reinforce the wave against dissipation, and many studies are based on oversimplified atmospheres or oceans in climate modelling studies, which can result in similar conclusions.

Finally, we conclude that a thermal atmosphere is not efficient in damping out the planetary wave. A dynamic atmosphere needs to be coupled to the planetary wave in order to clarify whether this can be modified in its properties. The unstable mode found when an atmospheric EBM is coupled could disappear but the weakly damped modes could also be excited by wind stress as suggested in recent works (Cessi and Paparella, 2001; Cessi and Primeau, 2001). However, the null negative effects of the thermal atmospheric components leave hope for effective input of energy against any form of dissipation.

Chapter 3

The Quasi-Geostrophic Coupled Model

In this chapter we will briefly explain the model used in the following sections of the thesis, the advantages of using such a model for our purposes and the basic configurations employed. However, a detailed explanation of the model equations, derivations and the general numerical formulation can be found in Hogg et al. (2003a,b). The model is intended to be for general public use and can be downloaded from the URL `http://www.noc.soton.ac.uk/JRD/PROC/Q-GCM`, together with its users' guide, details of recent developments and related publications.

3.1 Introduction

The aim of the Quasi-Geostrophic Coupled Model (Q-GCM) is to be able to represent coupled ocean-atmosphere dynamics in a transparent and efficient way, retaining at the same time simplicity and numerical rapidity. The importance of non-linear dynamics and high-resolution in both the ocean and atmosphere is evident in the climate system; these are both present in the model thanks to its numerical configuration and equations used.

The model dynamics are based on the quasi-geostrophic (QG) equations -which are known to be a very good and widely accepted approximation for mesoscale dynamics and planetary wave propagation- in both the atmosphere and ocean. However, if a fully coupled model is to be built, incorporating both mechanical and thermodynamical interaction between the two fluids, the QG equations raise a difficulty because they do not fully resolve the vertical fluxes of heat. This problem is overcome by embedding a mixed layer in both the ocean and atmosphere through which the two fluids communicate and where the mutual interaction takes place. This technique is not new; other authors (Kravtsov and Robertson, 2002; Kravt-

sov et al., 2005b) coupled their ocean-atmosphere model through an oceanic mixed layer, but the Q-GCM employes a mixed layer in each domain, allowing for an even better representation of heat transport and a simpler numerical formulation.

The Q-GCM is forced by latitudinal variations of incoming radiation, the atmospheric part of the model is represented as a re-entrant channel of N-layers coupled to an ocean of M-layers through their respective mixed layers; the ocean can be set up as either a box or a channel ocean and topography can be added respectfully of QG approximations. A schematic representation of the model is given in Fig.3.1. The Q-GCM can not only run as a coupled ocean-atmosphere model but it can also be decomposed into a forced model, in which the atmosphere (ocean) forces the oceanic (atmospheric) circulation.

The model sits on a β-plane in which the Coriolis parameter is given by $f = f_0 + \beta y$, where f_0 is the Coriolis parameter at a central latitude ϕ and β is its meridional gradient. The Q-GCM therefore represents a mid-latitude climate system, able to

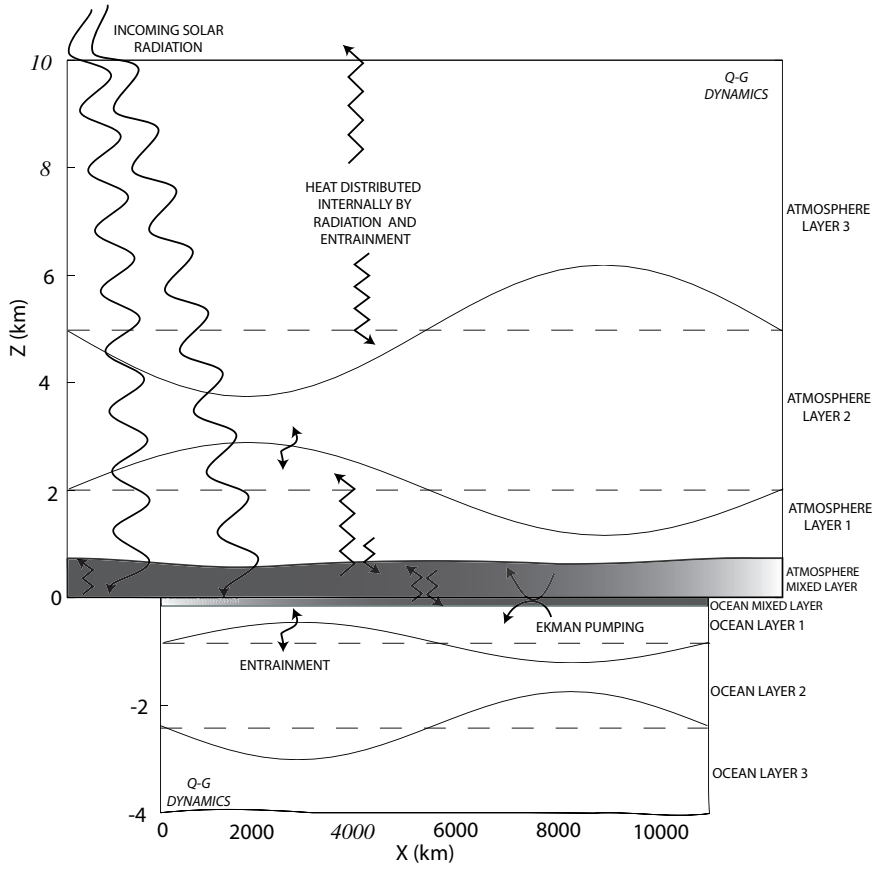

Figure 3.1: *Schematic (not to scale) of a three-layer version of the Quasi-Geostrophic Coupled Model [Adapted from Hogg et al. (2003a)]. Shaded areas correspond to the atmospheric (variable height) and oceanic (fixed height) mixed layers, which interchange momentum and heat fluxes between the two fluids. The atmospheric component is a zonally reentrant channel while the ocean is a box domain.*

reproduce the non-linearity in the atmospheric and oceanic dynamics with very high resolution at a very affordable machine time.

The only deficiencies of the model at this stage are the lack of possibility of introducing variable coastlines (other than the solid walls delimiting the ocean domain), the absence of equatorial dynamics (due to the use of QG approximations), the restricted thermodynamics employed and the parameterization of salinity or any other passive tracer. However, for idealised mid-latitude studies, these are all unimportant. Finally, we conclude that for the purposes of this study on the investigation of planetary wave propagation in a coupled ocean-atmosphere system, the Q-GCM perfectly suits our needs in terms of interaction dynamics, non-linearities in the system and versatility of the different configurations.

3.2 Model description

The model is symmetric around the ocean-atmosphere interface, with increasing layer numbering away from it. Then, the mixed layer is embedded in layer 1 for both atmosphere and ocean and the possible ocean topography would be parameterised within the last layer (Fig.3.1).

For a flat bottom 3-layer configuration, the QG potential vorticity (QGPV) equation is

$$\partial_t q_i + J(\psi_i, q_i) = f_0 \mathsf{Ae} + A_2 \nabla^4 \psi_i - A_4 \nabla^6 \psi_i \tag{3.1}$$

where q_i and ψ_i are the layer potential vorticities and stream functions respectively, $J(a,b) = a_x b_y - a_y b_x$ is the Jacobian and subscripts denote derivatives. We define

$$\mathsf{A} = \begin{bmatrix} \frac{1}{H_1} & \frac{-1}{H_1} & 0 & 0 \\ 0 & \frac{1}{H_2} & \frac{-1}{H_2} & 0 \\ 0 & 0 & \frac{1}{H_3} & \frac{-1}{H_3} \end{bmatrix}, \qquad \mathsf{e}_o = \begin{bmatrix} e_{o0} \\ e_{o1} \\ 0 \\ e_{o3} \end{bmatrix}, \qquad \mathsf{e}_a = \begin{bmatrix} e_{a0} \\ e_{a1} \\ 0 \\ 0 \end{bmatrix};$$

in the atmospheric QGPV equation the matrix A will simply be of opposite sign. The vector on the right, e, is the ocean and atmosphere entrainment vector for which $e_{o0} = w_{oek}$ and $e_{a0} = w_{aek}$ are the Ekman velocities, $e_{o1} = \frac{-\Delta_m T}{2\Delta_1 T} w_{oek}$ where $\Delta_i T$ describes the temperature difference across interfaces i and $i+1$ and finally $e_{o3} = \frac{\delta_{ek}}{2} \nabla^2 \psi_3$, with δ_{ek} a bottom drag. There is no entrainment of heat flux between other intermediate layers, i.e. $e_i = 0$ for $i > 1$, and because both the oceanic and atmospheric layers have constant potential temperature, any change in the layer's heat content will be given by modifications in its height.

The ocean and atmosphere Ekman pumpings are related through their density

difference ratio $r_\rho = \rho_a/\rho_o$ and are defined as

$$w_{oek} = r_\rho w_{aek} = r_\rho(\partial_x \tau^y - \partial_y \tau^x)/f_0$$

The last two terms on the right hand side of (3.1) correspond to Laplacian diffusion and biharmonic viscosity respectively. The latter is an effective way to remove enstrophy from small scales without damping the energy containing eddies (Rhines, 1986).

The layer PVs are given by

$$q_i = \nabla^2 \psi_i + \beta y + \mathsf{F}\Psi \tag{3.2}$$

where

$$\mathsf{F} = \begin{bmatrix} -F_{11} & F_{11} & 0 \\ F_{21} & -(F_{21}+F_{22}) & F_{22} \\ 0 & F_{32} & -F_{32} \end{bmatrix}, \qquad \Psi = \begin{bmatrix} \psi_1 \\ \psi_2 \\ \psi_3 \end{bmatrix},$$

and $F_{11} = f_0^2/(H_1 g_1')$, $F_{21} = f_0^2/(H_2 g_1')$, $F_{22} = f_0^2/(H_2 g_2')$, $F_{32} = f_0^2/(H_3 g_2')$ following the general convention $F_{n,m} = f_0^2/(H_n g_m')$ and g_i' and H_i are the reduced gravities and layer depths respectively. It is straightforward to extend the equations to any N-layer configuration.

As mentioned above, the system interacts via the two mixed layers, where stress and fluxes are parameterised and then entrained into their respective first layer.

The mixed layer temperature equations are expressed as

$$\partial_t T + \nabla \cdot (\mathbf{u}T) = \frac{T}{H_m}\begin{Bmatrix} w_{oek} \\ -w_{aek} \end{Bmatrix} + K_2 \nabla^2 T - K_4 \nabla^4 T + \frac{1}{H_m}\begin{Bmatrix} -\frac{F_{o0}-F_{om}}{\rho_o C_{po}} \\ \frac{F_{a0}-F_{am}}{\rho_a C_{pa}} \end{Bmatrix}, \tag{3.3}$$

where ρ_o and ρ_a are the ocean and atmosphere density, C_{po} and C_{pa} their specific heat capacity, H_m their mixed layer thickness and the mixed layer velocities, $\mathbf{u}$, where their quasigeostrophic and ageostrophic Ekman parts, are simply

$$(u_m, v_m) = (-\partial_y \psi_1, \partial_x \psi_1) + (\tau^y, -\tau^x)/(f_0 H_m).$$

Only the atmospheric mixed layer has a variable height due to numerical necessity whereas the depth of the oceanic mixed layer is fixed.

The second and third terms on the right hand side of (3.3) are Laplacian and biharmonic diffusions. The last term in (3.3) represent the fluxes at the top (F_m) and surface (F_0) of the mixed layer. In the case of the ocean, the heat fluxes are defined as

$$F_{o0} = F_\lambda - F_{long} - F_s, \qquad F_{om} = -\rho_o C_{po} \Delta_m T w_{oek}, \tag{3.4}$$

where F_λ encapsulates the sensible and latent heat fluxes, F_{long} is the longwave radiation, F_{om} the entrainment heat fluxes and F_s the incoming y-dependent solar

radiation. Where the atmosphere is in contact with land, the incoming shortwave radiation is absorbed by the land and reemitted as longwave radiation into the atmosphere. For a detailed derivation of heat fluxes between layers we refer to Hogg et al. (2003a,b).

The model is initialised from rest, driven by latitudinally varying solar forcing. The atmospheric stress over the ocean is computed, from which the oceanic mixed layer temperature is derived. Then, the oceanic QGPVs are found and from these the atmospheric mixed layer temperature. Finally the atmospheric QGPVs are stepped and the procedure is repeated for each time step.

For every experiment the Q-GCM is initially run for 20 years, during which the ocean spins up and reaches a steady state. Then, the run is continued for a total of 200 model years.

3.3 Experimental design and basic state solutions

Next, we describe the different parameters and configurations used in this study; modifications of any of these will be clearly stated in the next chapters. While the ocean response will be studied under different parameters, the atmospheric channel component of the model will remain constant throughout the study. The oceanic and atmospheric parameters used in the standard 3-layer basin ocean configuration are listed in Table 3.1. We opted for a relatively coarse resolution in the ocean (Δx=40 km), as we aim to identify large scale coupled ocean atmosphere interactions.

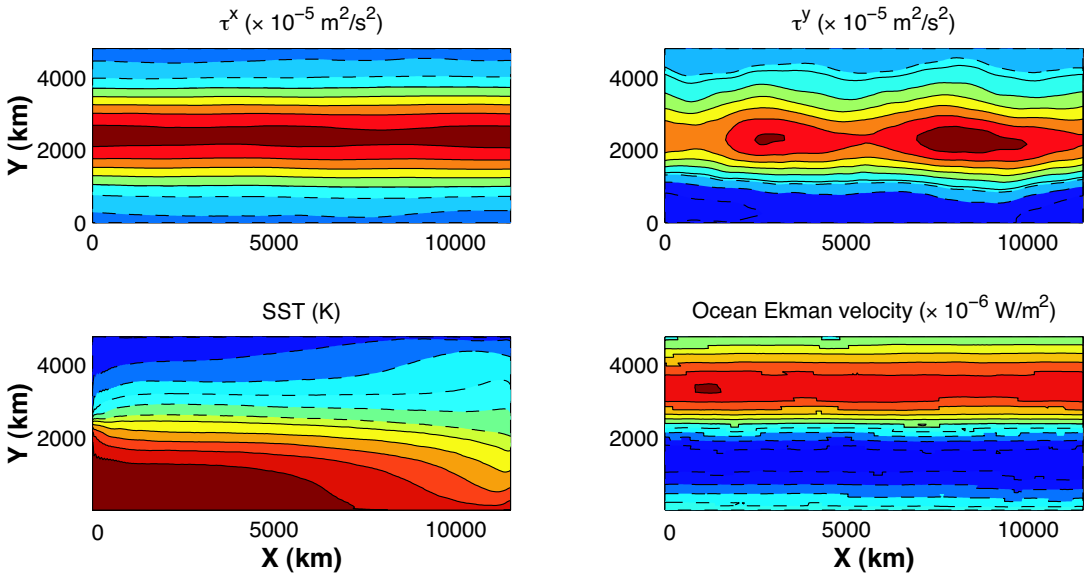

Figure 3.2: *Average of τ^x (Contour Interval=20), τ^y (CI=3), SST (CI=3) and w_{oek} (CI=0.2). Negative values are represented by dashed lines*

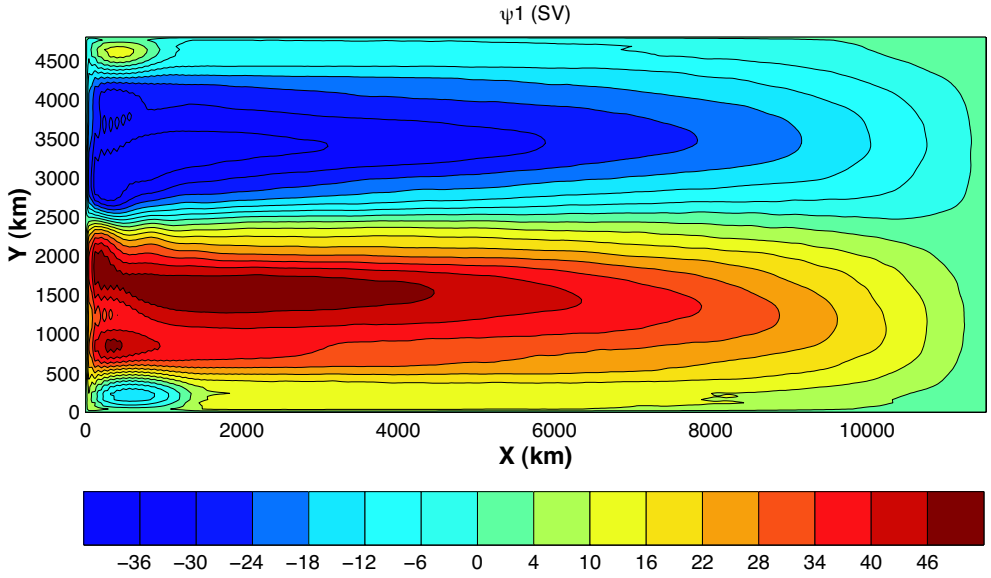

Figure 3.3: *Time-averaged ψ_1 of a 200 year run.*

We explore the response of the model at two different central latitudes, corresponding to 30^0 and 40^0; for the two cases, our model is barely resolving the first Rossby radius of deformation but not the second one. The basin dimensions are fairly large and, in particular, the ocean is very wide in order to study the zonal propagation of planetary waves under the effect of atmospheric coupling. This has the advantage of using a quasi-channel configuration but retaining the effects of meridional boundaries. In fact, Rossby waves are dissipated at the western boundary and any coupled Rossby mode will be affected by this interaction (Goodman and Marshall, 2003). Viscosities are set to their minimum value ensuring stability and no-slip boundary conditions are enforced.

The averaged ocean forcing fields, $\tau = (\tau^x, \tau^y)$, and relative Ekman pumping, w_{oek}, are shown in Fig.3.2, together with the oceanic sea surface temperature (SST). The flow responds to the wind stress in a symmetrical double-gyre solution, a subpolar and a subtropical gyre, and the gyres shrink moving down towards lower layers.

In Fig.3.3 we show the time-averaged stream function in the first layer. The Q-GCM actually computes the layer pressures and, in geostrophic balance, the oceanic stream functions are estimated from the layer pressures p_i via

$$\psi_i(x, y, z, t) = h_i\{p_i(x, y, z, t) - p_i(x_e, y, z, t)\}/f_0,$$

where x_e is the eastern longitude of the eastern coast.

We also note the presence of a strong boundary current, separating at the centre of the meridional extension of the basin, which will play a major role in damping the incident planetary waves in the model.

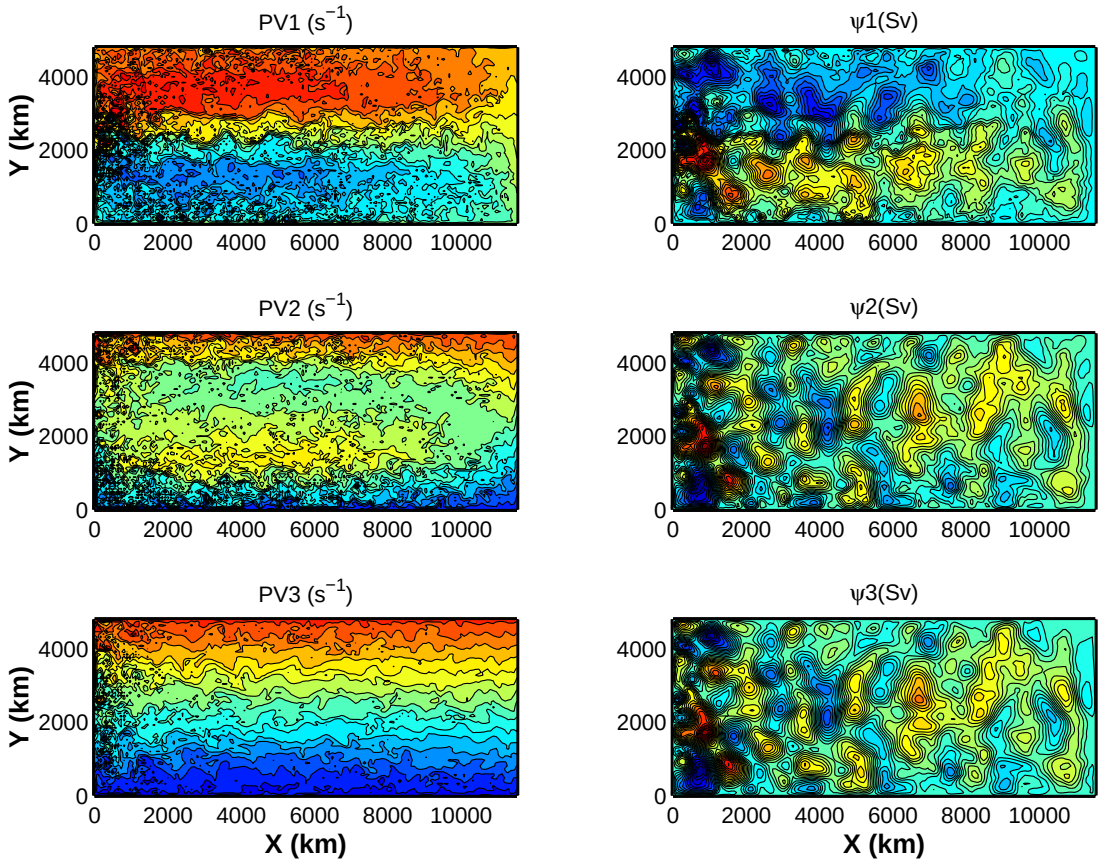

Figure 3.4: *Snapshots of PV fields (left panels) and stream functions (right panels) for each layer at the end of the run. Bluish colours are for lower values and reddish colours for higher values; contour interval is arbitrary.*

The instantaneous PV fields are shown on the left panels of Fig.3.4. In the first layer, where the wind forcing provides a source of PV, a sharp region denotes the separation of the two gyres, while in the inner layers a region of homogenised PV is formed, caused by the intense eddy activity driving an enstrophy cascade. This is clearly visible in the second layer but is shrinking in size in the deeper layers.

Snapshots of the layer stream functions can be found on the right panels of Fig.3.4. They reveal an intense eddy activity, a westward intensification of mesoscale structures in all three layers and the ability of resolving mesoscale eddies.

A 3-layer ocean model is able to better represent baroclinic instability, which is the source of these eddies on the scale of the first Rossby radius, enhancing the turbulent structure even in a coarse resolution simulation.

In order to reproduce the intense eddy activity and the dynamics of long wave-mean flow interaction, one can either increase the ocean resolution or the stratification of the layered model (Dewar and Morris, 2000). This will be discussed in Chapter 5, where the Q-GCM will be run with a 20 km resolution 6-layer ocean and the results compared with the standard configuration.

Parameters	Value	Description
	Ocean	
Z_i	3	N^o of layers
Δx	40 [km]	Horizontal grid spacing
(X, Y)	(11520,4800) [km]	Domain size
H_i	(300, 1100, 2600) [m]	Mean layer thicknesses
H_m	100 [m]	Mixed layer thickness
T_i	(278, 268, 258) [K]	Layer's potential temperature
g_i'	(0.05, 0.025) [m s^{-2}]	Reduced gravities
ρ_o	1×10^3 [kg m^{-3}]	Density
C_{po}	4×10^3 [J(kg K)$^{-1}$]	Specific heat capacity
K_2	5.7×10^2 [m^2 s^{-1}]	∇^2 diffusion coefficient
K_4	8×10^{10} [m^4 s^{-1}]	∇^4 diffusion coefficient
A_4	4×10^{10} [m^4 s^{-1}]	∇^4 viscosity coefficient
δ_{ek}	2 [m]	Bottom Ekman layer
f_0	7.292×10^{-5} [s^{-1}]	Coriolis parameter, ϕ=30^o
β	1.982×10^{-11} [(m s)$^{-1}$]	df/dy (30^o)
a_i	(53.1, 35.6) [km]	Rossby radii (30^o)
f_0	9.374×10^{-5} [s^{-1}]	Coriolis parameter, ϕ=40^o
β	1.753×10^{-11} [(m s)$^{-1}$]	df/dy (40^o)
a_i	(41.3, 27.9) [km]	Rossby radii (40^o)
	Atmosphere	
Z_i	3	N^o of layers
Δx	120 [km]	Horizontal grid spacing
(X, Y)	(15360,7680) [km]	Domain size
H_i	(2000, 3000, 4000) [m]	Mean layer thicknesses
H_m	100 [m]	Minimum mixed layer thickness
T_i	(330, 340, 350) [K]	Layer's potential temperature
g_i'	(1.2, 0.4) [m s^{-2}]	Reduced gravities
ρ_a	1 [kg m^{-3}]	Density
C_{pa}	1×10^3 [J(kg K)$^{-1}$]	Specific heat capacity
K_2	2.7×10^4 [m^2 s^{-1}]	∇^2 diffusion coefficient
K_4	3×10^14 [m^4 s^{-1}]	∇^4 diffusion coefficient
A_4	2×10^{14} [m^4 s^{-1}]	∇^4, viscosity coefficient
λ	35 [W m^{-2} K^{-1}]	Sensible and latent heat flux coefficient
a_i	(496, 259) [km]	Rossby radii

Table 3.1: *List of the standard oceanic and atmospheric parameters of the Q-GCM used in this study.*

Chapter 4

Coupled Rossby waves in the Q-GCM

Rossby wave propagation is investigated in the framework of an idealised middle-latitude coupled ocean-atmosphere model. Rossby waves are observed to be unstable according to a latitude-dependent instability process but also show resistance to this mechanism. A clear coupled Rossby wave mode is identified between a baroclinic oceanic Rossby wave and an equivalent barotropic atmospheric wave. The spatial phase relationship of the coupled wave is similar to the one predicted by Goodman and Marshall (1999) suggesting a positive ocean-atmosphere feedback. It is argued in this chapter that Rossby waves can be efficiently coupled to the overlying atmosphere allowing the waves to partially maintain themselves against dissipation and instability mechanisms so that the waves travel longer distances than those predicted by the unforced problem considered in LaCasce and Pedlosky (2004). Furthermore, evidence for a coupling speed-up is found and comparisons with previous theoretical and observational studies are given.

4.1 Introduction

In recent years there has been a growing interest in the scientific community in studying ocean-atmosphere coupled models (Liu, 1993; Frankignoul et al., 1997; Barsugli and Battisti, 1998; Goodman and Marshall, 1999; Ferreira et al., 2001; White et al., 1998; Neelin and Weng, 1999; White, 2000a; Gallego and Cessi, 2000; Cessi and Paparella, 2001; Colin de Verdière and Blanc, 2001; Kravtsov and Robertson, 2002, to mention a few). Different approaches have been used and different results, sometimes in disagreement, have been found. Nevertheless, there are a few key findings that can be pointed out. First, it is clear nowadays that the ocean does not respond passively to atmospheric forcing but interacts through feedback mechanisms (for ex-

ample, Latif and Barnett, 1994, 1996; Barsugli and Battisti, 1998; Pierce et al., 2001; Hogg et al., 2005; Kravtsov et al., 2005a). It is also well known that oceanic Rossby waves play a major role in the coupling physics (for example, Jin (1997); Goodman and Marshall (1999); Ferreira et al. (2001); Kravtsov and Robertson (2002); Arzel and Huck (2003)). A single theory for the coupling has not been reached yet because of its complexity and its geographical variations. These studies on atmosphere-ocean coupling can also help understand some questions mentioned in the first chapter of this thesis, like the differences between theoretical and observed Rossby wave phase speeds (Frankignoul et al., 1997; Qiu et al., 1997; Ferreira et al., 2001; White et al., 1998), although different answers are usually argued.

For instance, Frankignoul et al. (1997) studied the decadal variability of the extratropical ocean forced by stochastic winds. They found a baroclinic response consisting of a Rossby wave travelling at twice the theoretical speed, and concluded that this could be a reason for the fast speeds observed by Chelton and Schlax (1996). Also, they compared their results with a GCM and found good agreement in terms of frequency spectra but their conclusions did not hold above 45^oN where the mean flow velocity is comparable to the Rossby wave phase speed. The model of Frankignoul et al. (1997) was simple, with a flat bottom 2-layer ocean with neither a western boundary nor a mean flow, the latter of which has been proved to be of great importance in Rossby wave propagation (Killworth et al., 1997). Although there is a lack of reality in these models, simple models are often able to predict the basic coupling mechanisms (Barsugli and Battisti, 1998) and it seems very probable that, even if neither the mechanisms nor the magnitude are completely clear, coupling effects are able to modify Rossby wave phase speeds.

The two theoretical studies that are the most complete to date are given by Goodman and Marshall (1999) and Ferreira et al. (2001). Goodman and Marshall (1999) used a QG atmosphere overlying a QG ocean where the coupling mechanisms were both wind stress and thermal forcing. In their analytical model they found that coupled modes in which baroclinic Rossby waves can grow (unstable modes) exist under some circumstances through the linear interaction between travelling oceanic Rossby waves and forced stationary atmospheric planetary waves. The response in the atmosphere to the thermal forcing is equivalent barotropic and the resulting behaviour need not to be a first baroclinic mode. This important feature has not been considered much yet, although it has also suggested in White (2000a) where phase speeds consistent with a second mode Rossby wave have been found, though have not been pursued further. Furthermore, Goodman and Marshall (1999) pointed out that the atmosphere and the ocean need not be in phase (high pressures located above warm water) for the growing mode to exist, but that for the case of the Ant-

arctic Circumpolar Wave (ACW), growing modes occur if surface air pressure is in phase with SST, contrary to observations in White and Peterson (1996). A similar result was also found by van der Avoird et al. (2002) who, using a linear stability analysis of a 2-layer coupled model, described a coupled mode of interdecadal period originating from the interaction of a baroclinic Rossby wave and a quasi-stationary atmospheric equilibrated planetary wave with the same mechanisms as in the advective case of Goodman and Marshall (1999).

An extension to the Goodman and Marshall (1999) study is given by Ferreira et al. (2001) in which the major difference is the introduction of a boundary to the east and a radiation condition to the west. In this case similar patterns are found, like the equivalent barotropic atmosphere response leading to coupled growing modes and oceanic-atmospheric perturbations in phase. As in Frankignoul et al. (1997) the phase speed of the baroclinic Rossby wave was observed to increase due to larger wavelengths resulting from the coupling and leading to increased phase speeds. The simple atmosphere used in all these studies could be a weakness of the results but the ocean is more likely to be the cause of any misrepresentation.

Satellite observations are used by White et al. (1998) to study the interaction between the atmosphere and the ocean and analytical models are developed to be used in synergy with these studies. White et al. (1998) analysed anomalies in the sea level height (SLH), SST and meridional surface winds (MSW) signatures in the Pacific Ocean. They found a 90^o shift between SST and SLH in an advection mechanism and faster Rossby wave phase speeds in the mid-latitudes and slower in the subtropics, reducing the characteristic β-refraction of Rossby waves. In these studies the author argued that the effect of coupling was due to the introduction of a supplementary zonal phase speed component that increases the theoretical phase speed due to a SST-induced meridional anomalous heat transport by Ekman velocities. Moreover, in an identical study with the only difference of analysing data from the Indian Ocean, White (2000a) observed slower speeds arguing that in the Indian Ocean the phase relation between SST and MSW was opposite of that in the Pacific allowing for an eastward phase speed resulting in slower Rossby wave propagation. Based on Topex/Poseidon (T/P) observations, in both White et al. (1998) and White (2000a) different analytical models and theories for the two oceans are derived.

Although a general coupled Rossby wave model, describing the interaction of the oceanic Rossby wave with the overlying atmosphere and the phase relationship between the two, has not been developed yet, the literature presented here gives clear examples of the increasing interest and efforts on the study of coupled mechanisms in which oceanic Rossby waves are modified either in their structures or in

their phase speeds. In addition to modelling efforts, observations of the propagation of Rossby waves are able to characterise the wave properties as the record of satellite measurements increases. After the pioneering study of Chelton and Schlax (1996) several authors have applied satellite-based data analyses to infer Rossby wave activity (Wunsch and Zang, 1999; Cipollini et al., 2000; Hill et al., 2000; Fu and Qiu, 2002; Osychny and Cornillon, 2004; Fu, 2004). Wunsch and Zang (1999) pointed out the existence of both linear signals falling into the theoretical linear dispersion relation for Rossby waves and faster forced motions generated by other mechanisms such as those described by Killworth et al. (1997) and Qiu et al. (1997). The more thorough study of Osychny and Cornillon (2004) identifies faster phase speeds at all middle latitudes with differences increasing both moving polewards and towards shorter wavelengths; the latter characteristic is also confirmed by the recent modelling work of Killworth and Blundell (2005b).

The latitudinal dependence in the Rossby wave speed discrepancies has also been addressed by LaCasce and Pedlosky (2004), although with a different context. They considered the unforced problem with no mean flow in which Rossby waves are unstable due to a β-dependent baroclinic instability mechanism. Hence, baroclinic Rossby waves were easily breaking into barotropic eddies travelling at about 2 times the baroclinic wave speed arresting the propagation of the original baroclinic wave after a few thousands of kilometres from its source. It is important to underline that in their analytical calculations they did not consider the effects of mean flow, forcing or ocean-atmosphere feedbacks.

The main goals of the study presented in this chapter are the identification of the atmospheric influence and possible positive feedback on the oceanic Rossby wave propagation. Are Rossby waves subject to the LaCasce and Pedlosky (2004) instability mechanism? What are the effects of including the atmospheric forcing and coupling and do Rossby waves couple with the overlying atmosphere as has been observed and theorised? If this feedback exists, can it explain the features observed by remote sensing devices? We will focus on the possibility of a positive coupling between the oceanic wave and the atmosphere at middle-latitudes, trying to identify a coupled wave mode in a fully coupled ocean-atmosphere model and its subsequent response in the wave propagation. Comparisons with previous theories and observations will follow.

In Section 2 we identify the Rossby wave activities in the model and characterise their main properties with the help of statistical analyses in Section 3. We then proceed to isolate a coupled Rossby wave explaining the relationships with the atmospheric variables in Section 4 and conclude with a discussion of the results in Section 5.

4.2 Detection and identification of Rossby waves

The Q-GCM is run for 200 model years at two central latitudes $\phi = 30°$ and $40°$, for the parameters listed in Table 3.1. Oceanic and atmospheric variables are saved every 10 days in order to have a dense temporal sampling, useful for the statistical techniques used later on in the study and enabling direct comparisons with satellite measurements such as TOPEX/Poseidon, which provides observations approximately every 10 days.

We are then ready to identify the propagation of the oceanic Rossby waves generated by the unsteady winds in the model (Fig.3.2) and their basic properties. We begin by plotting Hovmöller diagrams (time-longitude plots at a given meridional position in the ocean basin domain) of the second interface height (OCH2), corresponding to thermocline displacements. The Hovmöller shown are for the north subtropical gyre, for correspondence with the real oceans at these latitudes; nevertheless, they show similar patterns at different locations.

As we are interested in westward propagating waves, we apply a westward filter to the data (Cipollini et al., 2000), the results of which are shown in Fig.4.1 for a particular time interval. Here, clear signals of crests and troughs are visible with a strong zonal variation in both amplitude and propagating speed. For comparison purposes, we also plotted the results from a previous run, with the same characteristics, at $\phi = 20°$. By following crests we can estimate an approximate velocity of the dominant signals, and a simple inspection of the diagrams reveals the theoretical increase in phase speed as we move towards lower latitudes. With this crude estimation, at $\phi = 30°$ the phase speed is around 6.5 cm/s and at $\phi = 40°$ around 5 cm/s. These are relatively high phase speeds since in the simulations our Rossby radii give us velocities of 5.2 and 2.9 cm/s at 30° and 40° respectively for the first baroclinic Rossby wave mode.

The high phase speeds identified seem to agree with some observations, for instance Osychny and Cornillon (2004), who find differences in wave propagation stronger at higher latitudes. Hovmöller plots of SST anomalies reveal similar results for all central latitudes.

Another fundamental feature in Fig.4.1 is the apparent breaking and instability of waves, which is stronger as we move away from the Equator. In fact, at lower latitudes crests and troughs are very well defined and consistent throughout their propagation in single beams. However, as we increase the central latitudes in our simulations, faster waves start to appear, generated from an original "mother wave", breaking and destroying their source as they get stronger with latitude.

This result recalls the instability mechanism proposed by LaCasce and Pedlosky

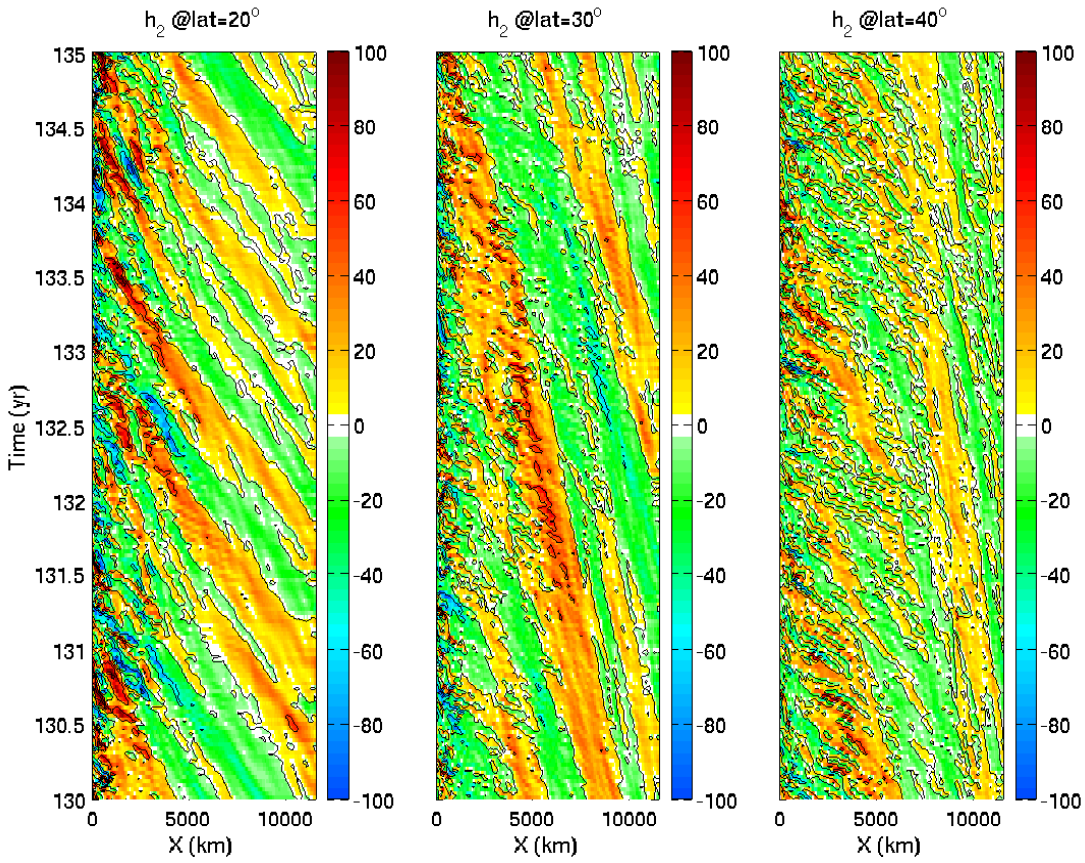

Figure 4.1: *Hovmöller plots of the second interface heights OCH2 (in meters), representative of the thermocline displacements, for three different central latitudes ($\phi = 20^o, 30^o, 40^o$). Note the increasing breaking of the waves as the latitude increases.*

(2004) in which Rossby waves are subject to a latitude-dependent baroclinic instability, resulting in faster barotropic Rossby waves. In fact, a time series of the two interface heights in a point in the western side of the basin where these faster waves are found, reveals the barotropicity of the signal, with interface height displacements travelling with a barotropic vertical structure, suggesting that we are in presence of the LaCasce-Pedlosky's instability mechanism.

A complementary and more accurate identification of the spectral characteristics of the Rossby waves identified is achieved through a Fast Fourier Transform (FFT) of the westward-filtered data, resulting in frequency-wavenumber spectra. To this purpose we applied a temporal band-pass filter to the data between 1 and 5 years at every spatial location in order to suppress the high frequencies and the decadal-interdecadal signals.

The FFT analysis plotted in Fig.4.2 reveals Rossby waves propagating much faster than the unperturbed (dashed lines) and the perturbed dispersion relation (solid lines) predict, with mean peaks showing phase speeds around twice the un-

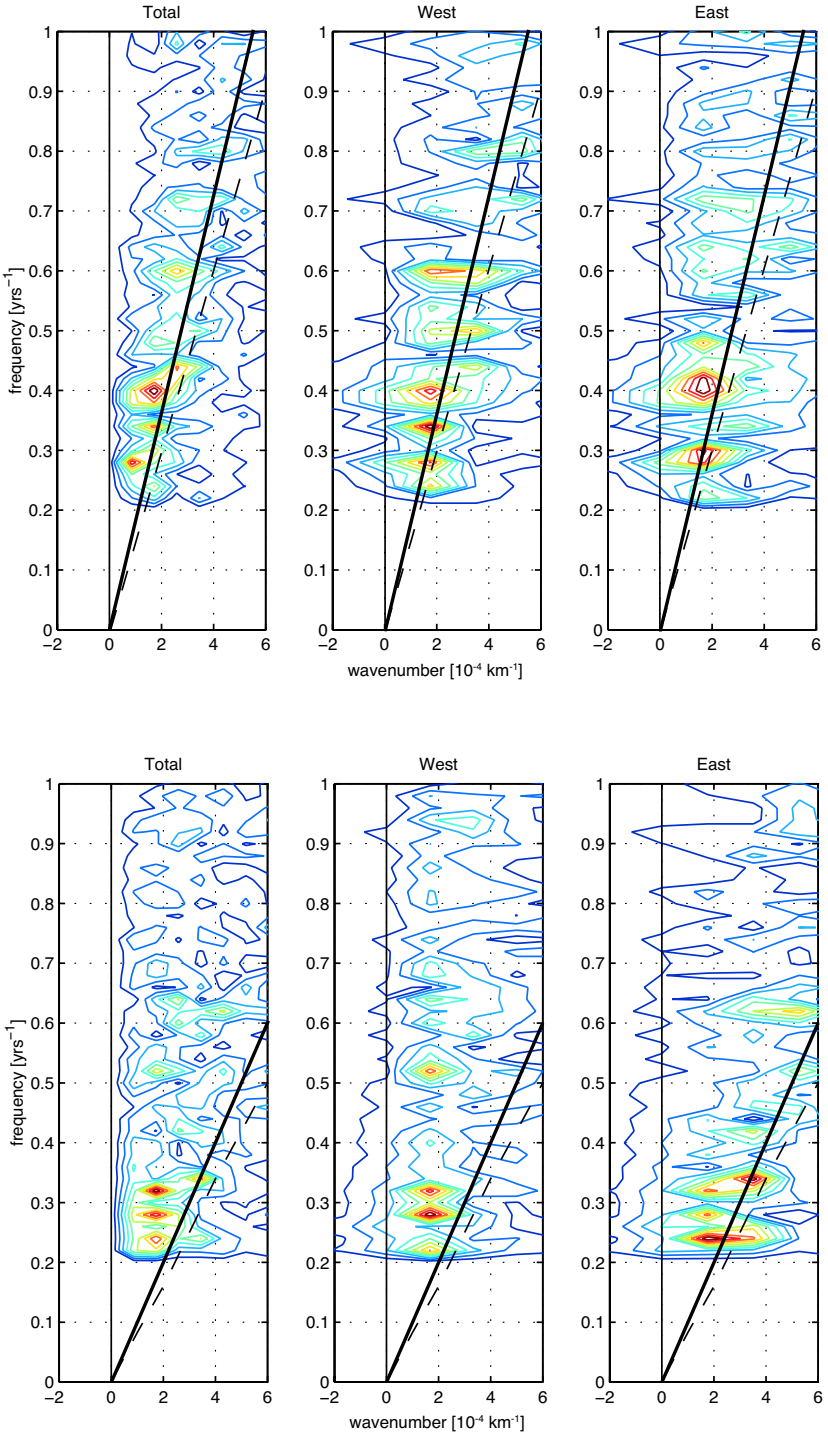

Figure 4.2: *Frequency-wavenumber spectra of OCH2 anomalies at $\phi = 30°$ (top panels) and $\phi = 40°$ (bottom panels) for the entire basin (first), the western side (second) and the eastern side (third panels). Magnitude is normalised by its maximum value for each case. The broken line represents the theoretical dispersion relation at the two central latitudes computed from the theoretical dispersion relation with the model's Rossby radii. The solid lines are the computed perturbed dispersion relation with the inclusion of a zonal mean flow (See Appendix B). The mean flow speed-up is about 1.2 for typical examples, close to the suggested value of 1.4 by de Szoeke and Chelton (1999).*

perturbed values at both central latitudes. Here, we will refer to "perturbed solution" to the dispersion relation computed with the inclusion of a zonal mean flow while the "unperturbed solution" correspond to the classical linear dispersion relation (For computations of perturbed solutions see Appendix B. The mean flow computed at the location A in Fig.B.1, typical for the latitudes considered, correspond to the solid line in Fig.4.2). In our 3-layer system we found only small variations in the dispersion relation when including the model zonal mean flows. Following the theory of de Szoeke and Chelton (1999), and making use of our density jumps and mean layer depths, we should reach a speed-up of about 1.4. However, in the calculations given in Appendix B, the maximum speed-up was found to be of around 1.22 and this corresponds to the solid lines in Fig.4.2.

As we move polewards, more and more high-frequency waves appear in the western part of the basin, indicating the generation of fast barotropic waves probably due to baroclinic instability processes. For the case at $\phi = 30°$ (upper panels of Fig.4.2) we find wave speeds ranging from 6 to 9 cm/s, all of them much higher than the unperturbed and perturbed theory would predict. The main peak in the spectra has a period, P, of about 2.5 yr and is shared by the total, western and eastern side spectrum. Another peak, with a period of about 1.5 yr and speed of 9-9.5 cm/s, is present only in the spectrum of the western side of the basin, identifying the fast barotropic waves. We can see that spectral peaks fall into the long nondispersive range, where the phase speed is well approximated by $c_x = -\beta a^2$ and tend to diverge from the linear dispersion relation as the wavelength decreases, consistently with Wunsch and Zang (1999), Osychny and Cornillon (2004) and Killworth and Blundell (2005b), meaning that shorter waves travel faster than the longer ones and there is evidence of both linear and non-linear activity in the spectrum. It is also evident from the FFT analysis that the western side is more energetic and presents more variability at all frequencies than the eastern side.

One might argue that, because the resolution is quite coarse, the phase speeds present in these data are not properly taking into account the wave-mean flow interaction and the baroclinic mean flow speed-up is not fully reflected in these results. However, if we believe the theory by LaCasce and Pedlosky (2004), the fast barotropic waves should travel at approximately the double of the linear baroclinic speed, and this is reflected in our data at both central latitudes.

For the central latitude $\phi = 40°$ (lower panels of Fig.4.2) the results are qualitatively very similar. The main peak is around P= 3-3.5 yr with phase speeds of about 4-4.5 cm/s. The extra peak in the western side of the ocean basin has a period of 2 years and phase speeds of 7.5-8 cm/s. The wavenumber of the main peaks is around $2{\times}10^{-7}\mathrm{m}^{-1}$, which corresponds to a wavelength $\lambda = 5 \times 10^6$m. Al-

though quite a long wave, Goodman and Marshall (1999) found in their analytical results k=π(5500 km)$^{-1}$=5.7×10^{-7} or $\lambda \sim 1 \times 10^7$m as the wavelength of maximum growth at a decadal period ($\omega = 2 \times 10^{-8} s^{-1}$) for their coupled Rossby mode. Our wavelengths are different because of the choice in our basin dimensions and, if an atmospheric coupling is occurring, an increase in the wavelengths of the coupled waves is expected, as suggested by Ferreira et al. (2001).

Generally, we discovered very fast Rossby waves in our model runs, all with phase speeds faster than predicted by the linear theory, with increasing differences as we move towards higher latitudes (Chelton and Schlax, 1996; Killworth et al., 1997). Also, we observed the instability mechanism proposed by LaCasce and Pedlosky (2004). However, the waves can travel much longer distances than those predicted by LaCasce and Pedlosky (2004). At the latitudes presented in this study, the baroclinic "mother wave" should no longer be able to propagate the long distance of our very wide ocean basin and leave space only to the resulting barotropic vortices. Moreover, the amplitudes of the waves, in all three central latitudes presented in Fig.4.1, seem to be enhanced as they move westward. The ability to propagate longer distances and the increase in the magnitude of the anomalies make us think of the possibility of a positive coupling with the atmosphere, sustaining the waves against dissipation and instability processes. Besides, although some peaks in the FFT analyses fall into either the unperturbed or the perturbed dispersion relation, one or two major peaks at both central latitudes are clearly too fast and are not explained by the inclusion of a sheared mean zonal flow.

Coupled Rossby modes have been identified in data (White et al., 1998; White, 2000a, 2001) and simple analytical-numerical models (Goodman and Marshall, 1999, 2003), but whether they really exist in fully coupled models of intermediate complexity is still unclear and the processes involved within a full dynamics model not completely understood.

4.3 Principal components analysis of the oceanic and atmospheric variability

We already know the ocean climatology of this model from Chapter 3. The ocean circulation is dominated by a double gyre circulation, subtropical and subpolar, separated by a narrow and strong zonal current, where the SST presents a sharp front. The channel atmosphere is instead characterised by a zonally symmetric circulation, with sloping interface heights (ATH1 and ATH2) towards the south, due to the radiation condition of heating in the southern region and cooling in the northern one.

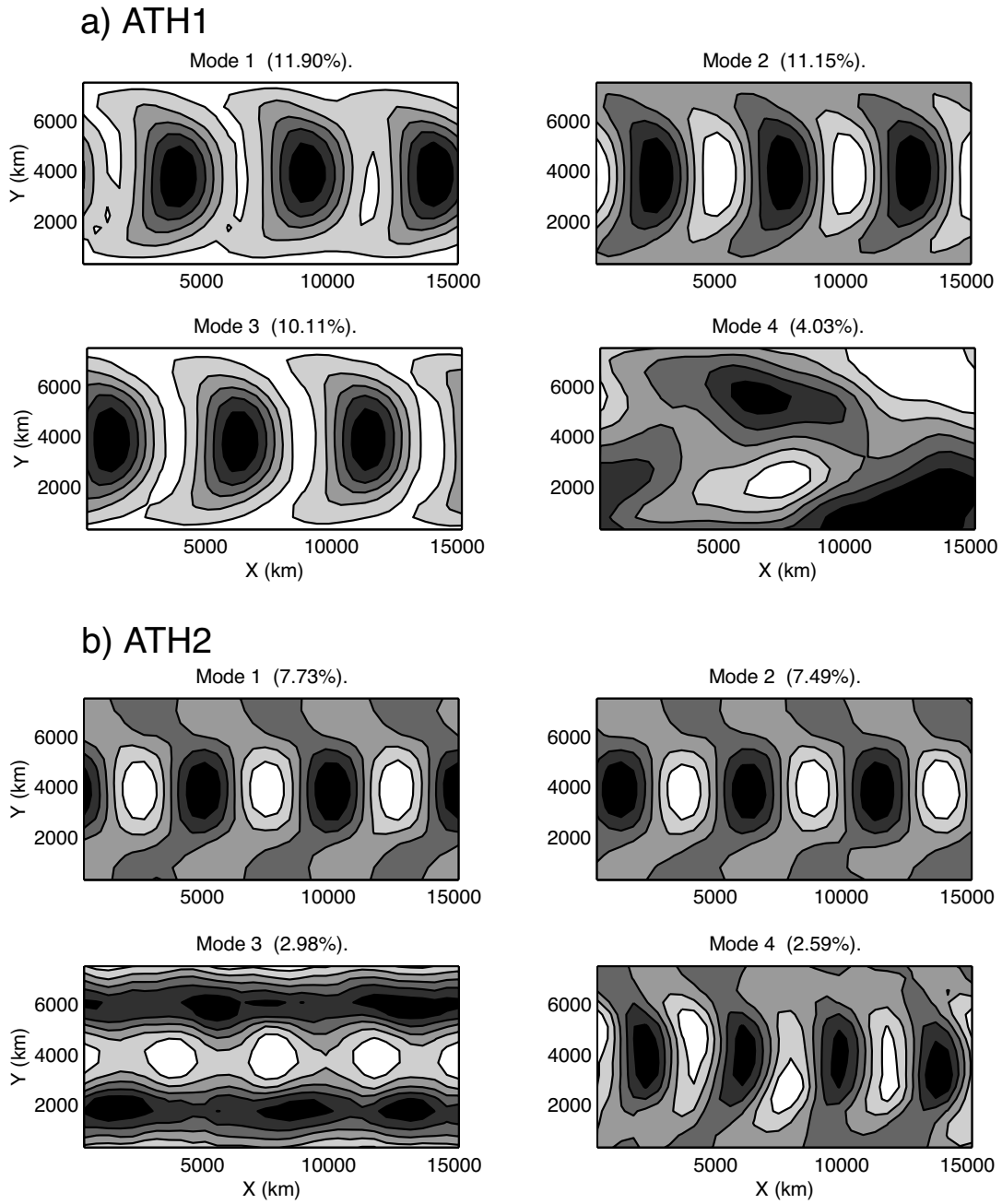

Figure 4.3: *First four Empirical Orthogonal Functions of the unfiltered ATH1 (upper panels) and ATH2 (lower panels). In the grey scale dark colours correspond to negative weights.*

The atmospheric dynamics are then inferred from an Empirical Orthogonal Functions (EOFs) analysis (Preisendorfer and Mobley, 1988). EOFs separate the data set into dominant spatial modes of variability, attributing a portion of the total variance to each one of them; the eigenvectors of the eigenvalue analysis correspond to the spatial patterns while the associated eigenvalues represent the variance explained by the mode (details of the statistical eigentechniques used in this chapter can be found in Appendix A). In Fig.4.3 we show the first four EOFs of the two unfiltered

interface heights, ATH1 and ATH2, at the central latitude of 40°. The four ATH1 EOFs explain around 37% of the variance of the unfiltered data; when a low-pass filter is applied to the data the percentage explained is increased to around 65%. EOF-1 has a wavenumber-3 structure, apparently propagating westward, in quadrature with EOF-2 of similar eigenvalue. EOF-3 is dominated by a wavenumber-3 eastward-propagating signal, paired with EOF-5. A mode-1 in meridional and zonal wavenumber is represented by the EOF-4, paired with EOF-6 and travelling eastward.

The analysis for ATH2 results in similar patterns, with the first four EOFs accounting for the 21% of the total variance (∼45% in the filtered case). An eastward propagating wave is shown in EOF-1 and EOF-2, a standing annular/wavenumber-3 is dominating EOF-3 and a wavenumber-4 westward-propagating signal appears in EOF-4, paired with EOF5. Similar results are found when applying the principal component analysis to the unfiltered atmospheric surface temperature (AST). In fact, for both central latitudes a wavenumber-3 propagating wave and the standing annular/wavenumber-3 mode explain most of the variance.

The results obtained with the EOFs analysis of the unfiltered data are in agreement with previous similar studies (Kravtsov et al., 2003; Hogg et al., 2005; Kravtsov et al., 2005b); however, they do not shed much light on the atmospheric wave propagation and we need a more powerful technique to address the question of what are the characteristics of the wave dynamics in both ocean and atmosphere and whether they are related. To this end, we will next apply a variation of EOFs to our data, the Complex Empirical Orthogonal Functions (CEOFs) analysis, more suitable for studying propagating waves.

4.3.1 Patterns of observed Rossby waves in both ocean and atmosphere

Statistical eigenvalue analysis can be a very powerful tool for identifying particular modes of variability in a given set of data. However, EOFs can identify standing oscillations, giving only suggestions of the existence of propagating signals; these can be highlighted by a CEOFs analysis, a technique designed to characterise the propagating modes of variability with a pair of real and imaginary spatial pattern in quadrature with one another (Preisendorfer and Mobley, 1988; von Storch and Navarra, 1999), a method applied to the study of Rossby waves and basin modes in many previous works (White, 2000a, 2004; Santoso and England, 2004; Yang et al., 2004). After the CEOFs are computed, the real and imaginary eigenvectors, together with their eigenvalues, can be manipulated to obtain several useful functions

defining the mode evolution in both space and time (see Appendix A for a detailed explanation). We therefore try to identify the periods and spatial characteristics identified so far in both the atmosphere and the ocean at the two central latitudes.

Since we are interested in the propagation of Rossby waves only, and we have recognised the main periods involved at both $\phi = 30°$ and $40°$, we apply a 1-10 year band pass filter to all our variables, filtering out interannual and interdecadal frequencies before performing the CEOFs analysis on our data sets. Fig.4.4 shows the third and fourth mode of the spatial patterns of OCH2 at $\phi = 30°$. The first two modes have semi-annual periods, spatial structures not consistent with Rossby waves and believed to be low-order basin modes characterised by a north-south dipole. CEOF-3 explains ∼14.5% of the variance and propagates faster than CEOF-4, with a basin mode-like structure, whilst CEOF-4 (∼6.3%) is clearly associated with a Rossby wave propagating westward. This is visible comparing the real (left panels) and the imaginary spatial structures (right panels) in Fig.4.4. Results for SST show similar patterns, with westward propagating CEOF-3 and CEOF-4 (not shown).

Analysing the spectra of the principal components (PCs) we can extract the periods of each CEOFs mode. The spectra of the modes in Fig.4.4 and the corresponding ones for SST are plotted in Fig.4.5. Broken lines are associated with CEOF-3 and solid lines with CEOF-4. The Rossby wave in mode-4 has a pronounced peak at 0.4 years^{-1} (P= 2.5 yr), which corresponds to the strongest peak in the FFT analysis, for both OCH2 and SST; the peak at P= 3.5 yr, close to the linear theory, is given by CEOF-3. Both modes present also other peaks at shorter periods, probably associated with the high-frequency faster Rossby waves.

The same analysis was performed on the data at $\phi = 40°$. In this case the spatial

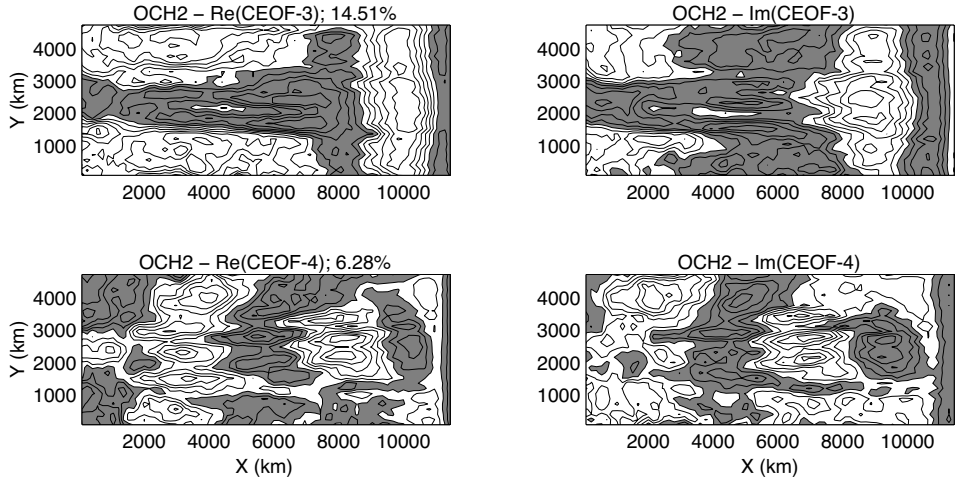

Figure 4.4: *CEOFs real and imaginary spatial patterns for OCH2 at $\phi = 30°$. Top: CEOF-3 (14.5%); bottom: CEOF-4 (6.3%). Negative weights are shaded.*

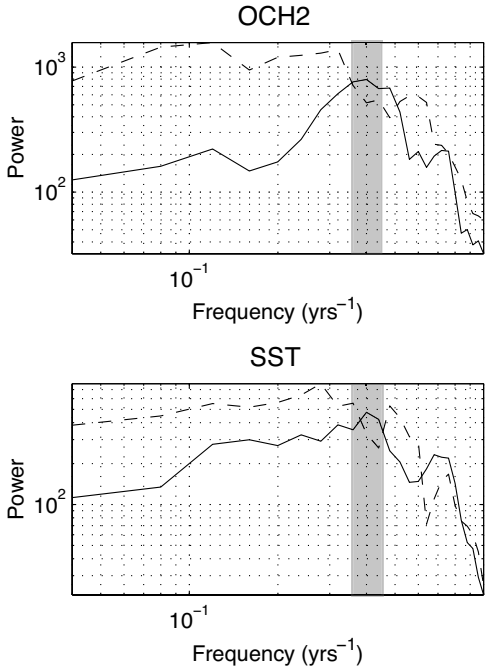

Figure 4.5: *Normalised spectra for OCH2 and SST at $\phi = 30°$. Broken lines: CEOF-3, solid lines: CEOF-4. The latter has a common peak for OCH2 and SST around P=2.5 yr, corresponding to the main Rossby wave peak. Mode-3 is characterised by a 3.5-yr period, which relates to the second peak close to the linear dispersion relation. Both modes are also energetic at shorter periods.*

patterns associated with the main Rossby wave peaks were found to be CEOF-1 and CEOF-2. In Fig.4.6 we plot the results for CEOF-2, with a similar percentage of variance as in CEOF-3 in the case of $\phi = 30°$, for OCH1, OCH2 and SST. Again the wavenumber-3 westward propagating Rossby wave is visible in all variables with an apparent baroclinic structure.

But what are the structures dominating the propagating features in the atmosphere? We find that the main atmospheric response in our simulations is a wavenumber-3 wave at all central latitudes. The first two modes in the CEOFs analysis are dominated by an annular mode but CEOF-3 and CEOF-4, plotted in Fig.4.7 for ATH1 and ATH2, show the wavenumber-3 wave structure with an important and fundamental difference between the two.

The atmospheric interface heights CEOF-3 show a wavenumber-3 wave, of relatively high percentage of variance (16.34% and 10.83%), propagating eastward. CEOF-4 for both ATH1 and ATH2 explains a much smaller amount of variance in the atmosphere (6.53% and 4.63%), but the same wavenumber-3 wave is observed to travel westward instead (bottom panels of ATH1 and ATH2 in Fig.4.7), with apparent equivalent barotropic structure. The atmospheric surface temperature (AST) has the same response in spatial patterns for both modes (not shown).

Once again, the periods of the oceanic and atmospheric modes shown so far are inferred from the spectra of the correspondent PCs. Normalised spectra of atmospheric CEOF-3 and CEOF-4 and oceanic CEOF-1 and CEOF-2 are plotted in

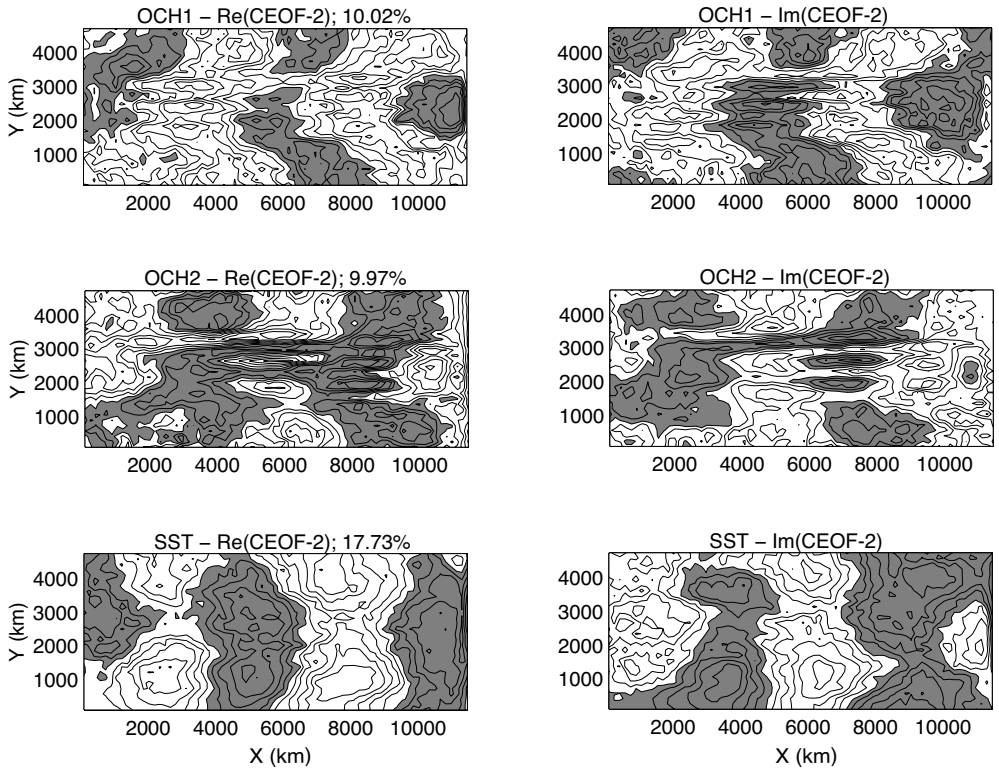

Figure 4.6: *Spatial patterns of the second CEOF modes of OCH1,OCH2 and SST at* $\phi = 40°$*. Negative weights are shaded.*

Fig.4.8. The atmospheric CEOF-3 (broken lines) are dominated by energy at short periods in all three variables and do not seem to share any relation with the oceanic spectra of CEOF-1. In contrast, the atmospheric CEOF-4 modes have a clear peak for $P \sim$3 yr, matching the oceanic CEOF-2 spectra with exactly the same period. Thus, an atmospheric equivalent barotropic wave, travelling westward with a period of around 3 years, seems to be coupled with a baroclinic Rossby wave of same period.

Some doubts can arise at this point on whether the atmospheric wave is really travelling westward or not. The plots shown in Fig.4.7 relate to the real and imaginary part of the spatial pattern for a given mode, in quadrature with each other. This however does not necessarily give a clear indication of the sense of the propagation and the eye can be misled. As discussed before, the CEOF technique can be extended from the simple description of the spatial patterns given by the eigenvectors and other useful relations can be found manipulating the eigenanalysis results.

The spatial phases can be computed from the eigenvectors of a particular mode, showing the relative phase of an oscillation in that mode, and giving a definitive sense of propagation. For the case of the oceanic Rossby waves there is no doubt we are in presence of westward propagating signals. The spatial phases of OCH1 and OCH2 CEOFs were computed as a test, showing the westward sense of propagation

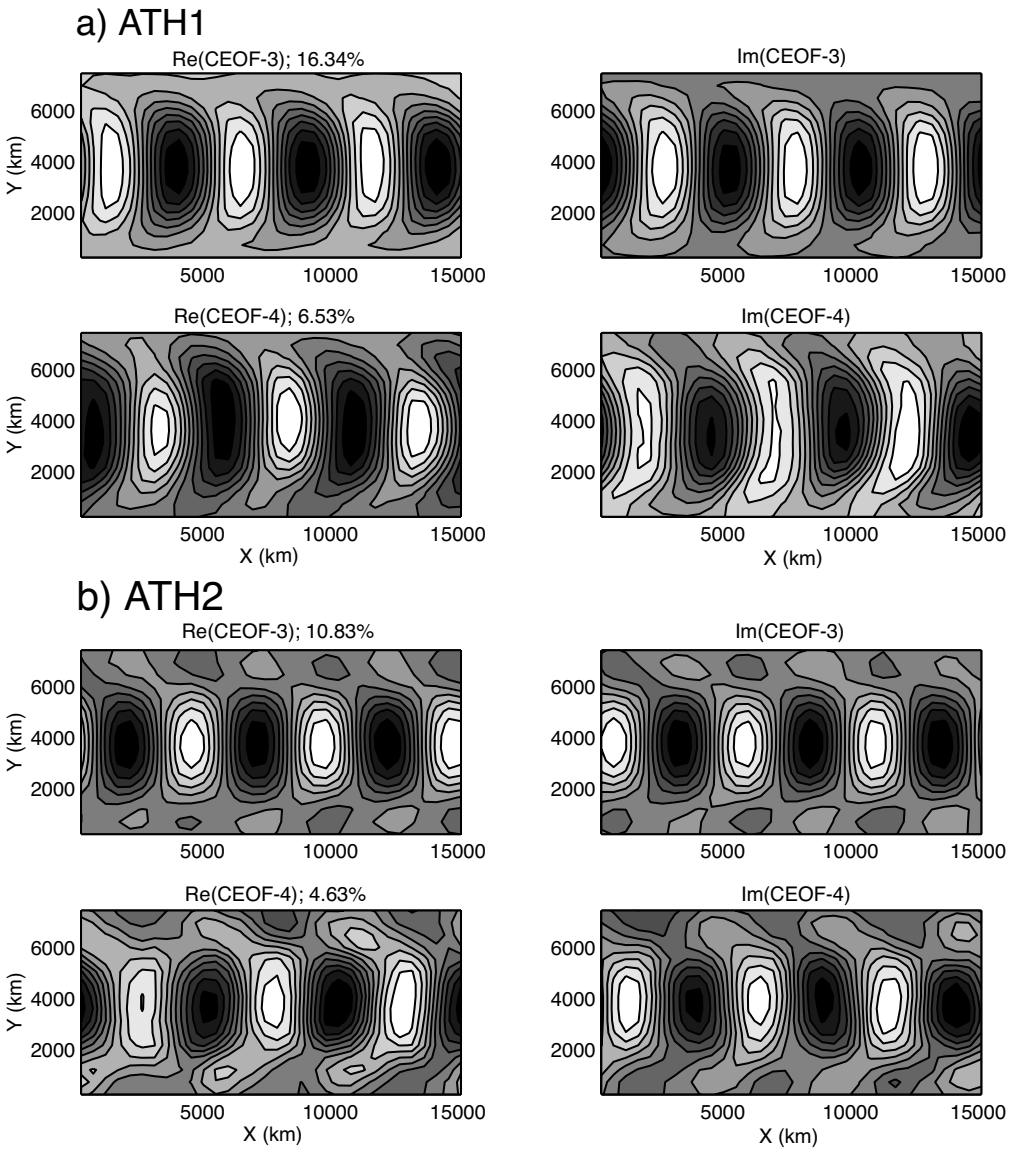

Figure 4.7: *a) CEOFs spatial patterns for the first interface height (ATH1). Top panels: CEOF-3 (16.34%) propagating eastward as a wavenumber-3 wave. Bottom panels: CEOF-4 (6.53%) propagating westward as a wavenumber-3 wave. b) Same as a) but for the second interface height (ATH2). Top panels: CEOF-3 (10.83%) propagating eastward as a wavenumber-3 wave. Bottom panels: CEOF-4 (4.63%) propagating westward as a wavenumber-3 wave.*

given by the phase degrees.

In addition to the spatial phases, we can compute the temporal phases, describing the variation of the phase of a particular oscillation with a given period. If the phase increases monotonically from 0° to 360°, it is an indication of the presence of cyclicity in the variable considered (Venegas, 2001). The temporal phases of the OCH2 CEOF-4 and CEOF-2 at $\phi = 30°$ and $\phi = 40°$ respectively represent a clear cyclicity (Fig.4.9), with similar periods as the ones given by their spectra. These

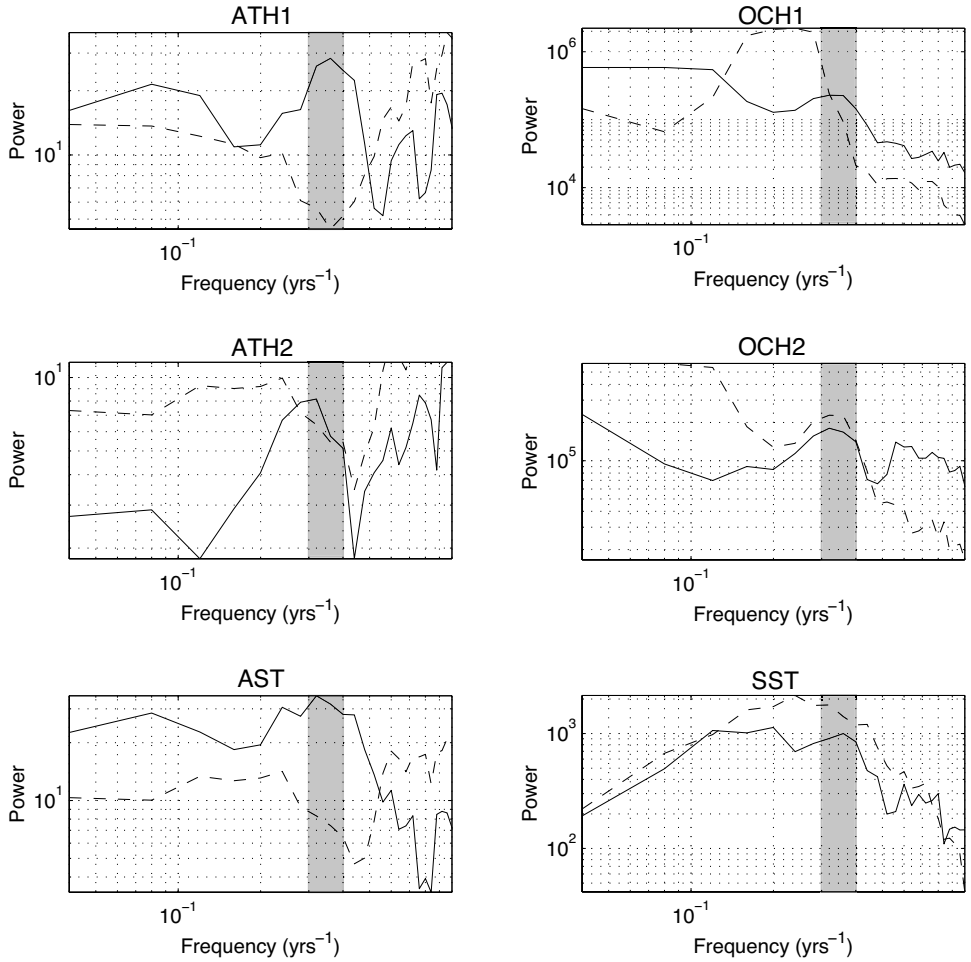

Figure 4.8: *Normalised spectra of atmospheric and oceanic h1,h2 and surface temperature. Left panels: atmospheric spectra. Broken lines are for CEOF-3, dominated by high frequencies, and solid lines for CEOF-4, with a common peak at P ∼3 yr. Right panels: oceanic spectra. Broken lines are for CEOF-1 and solid lines for CEOF-2, which shares the same peak as the atmospheric variables.*

are the two waves associated with the biggest peaks in the frequency-wavenumber dispersion relation shown in Fig.4.4 and Fig.4.6. The first is dominated by cycles of about 2.5 yr with other shorter cycles involved, whilst the second one has clear cycles oscillating between periods of 3 and 4 yr. One must remember that all the frequencies in the spectrum of a mode are captured by its temporal phases, therefore a single cyclicity will be difficult to determine. If we really wanted to isolate a single mode, we should have applied a narrower band-pass filter and in that case the results of the CEOFs analysis would have been more precise in describing a particular wave pattern.

For the more controversial case of the atmosphere, the spatial phases leave no doubt over the westward propagation of the CEOF-4 wave in ATH1 and ATH2. In Fig.4.10 the phase degrees grow as we move westward and the wave is in an apparent

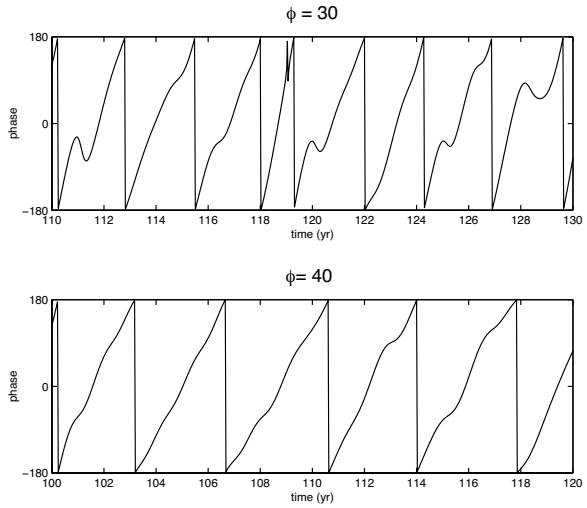

Figure 4.9: *Temporal phases of the OCH2 CEOF-4 at $\phi = 30$ (top) and CEOF-2 at $\phi = 40$ (bottom) for two selected time intervals. For the two cases, periods correspond to 2 to 2.5 and 3 to 4 yr respectively.*

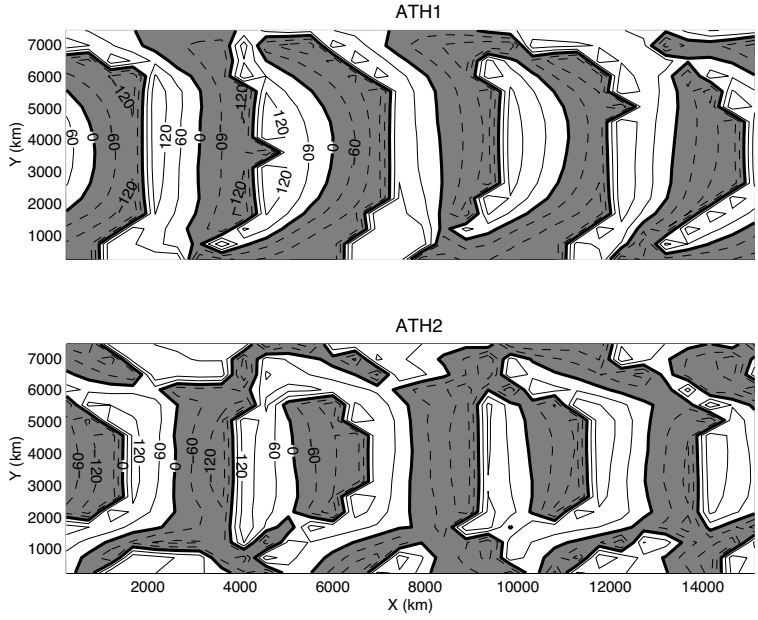

Figure 4.10: *Spatial phases for atmospheric ATH1 and ATH2. Contour interval is $\pm 60°$. Since the phase is computed over half cycle (π) the nodes appear to be the double. The phase degrees indicate a westward propagation in the two variables.*

equivalent barotropic state with the same initial arbitrary phase.

Finally we can nicely represent the propagation of the atmospheric and oceanic wave with a sequence of maps, computed at 90° intervals, multiplying the real and imaginary part of the spatial components by the cosine and sine of the phase respectively as shown in Fig.4.11.

This should be read from top to bottom, following weights of the same sign during the half cycle evolution. Each variable is initialised with the same arbitrary phase. The oceanic wave is observed to propagate as a wavenumber-2 baroclinic

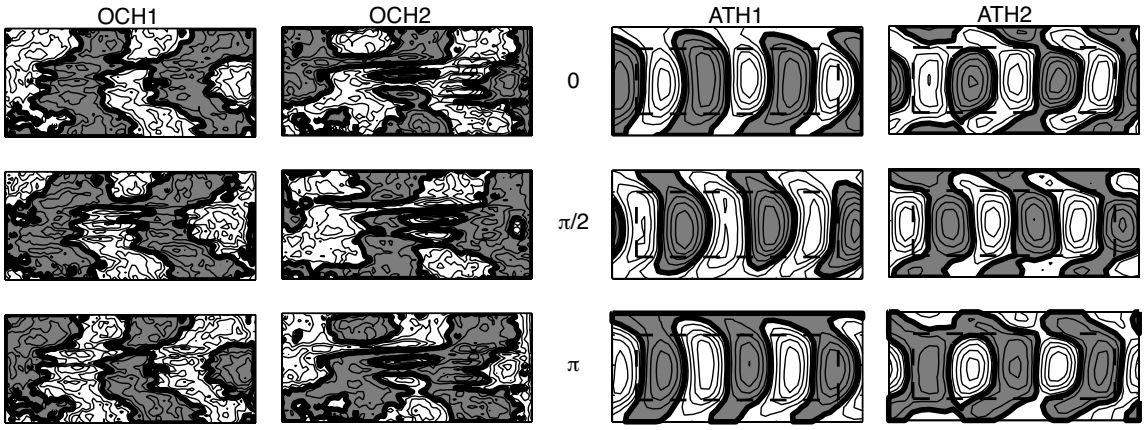

Figure 4.11: *Phase sequence of the oceanic CEOF-2 and atmospheric CEOF-4 over half cycle at ϕ=40. The plot should be read from top to bottom, following weights of the similar sign, giving a westward sense of propagation for all variables at approximately the same speed.*

wave with a defined and coherent pattern over the entire basin. The atmospheric wave is instead equivalent barotropic with a wavenumber-3 structure, following the oceanic wave at approximately the same speed. The meridional extension of the atmospheric wave is given by the dimension of the ocean basin, represented by the rectangular dashed box, and oceanic anomalies are observed to be in phase with atmospheric anomalies.

Summarising the results obtained so far, we identified Rossby waves in the Q-GCM travelling faster than the linear theory predicts. These waves are observed to break, possibly because of an instability mechanism similar to the one proposed by LaCasce and Pedlosky (2004), but are able to counteract the instability and propagate much longer reaching the western side of our extremely wide ocean basin. The baroclinic instability process involved in the inverse energy cascade driving an initial baroclinic Rossby wave to barotropic vortices would be even stronger in our 3-layer ocean, which allows mode-1/mode-2 interactions. Thus, since we are inclined to be believe the results by LaCasce and Pedlosky (2004) because Rossby waves are known to be unstable in the real ocean and are indeed observed to be so in our simulations, we must understand why they resist against dissipation processes.

After characterising the oceanic Rossby waves at both central latitudes we looked at the atmospheric response, finding atmospheric waves that are able to propagate westward. The major peak in the spectra of these waves match the oceanic Rossby wave period. From the statistical eigenanalysis employed, an oceanic wavenumber-2 baroclinic Rossby wave, dominating the frequency-wavenumber spectrum, seems to be coupled with an atmospheric equivalent barotropic wave travelling in phase with

the first oceanic interface height.

The amplitude of the baroclinic oceanic wave is given by the signals identified in the Hovmöller plots in Fig.4.1, and these are characterised by anomalies of the order of 30 meters. In the other hand, the amplitude of the equivalent barotropic atmospheric wave can be inferred by the temporal amplitudes in the CEOF analyses, revealing anomalies of the interface heights between 100 and 200 meters, increasing with height.

We also noticed when plotting the longitude-time evolution of OCH2 (Fig.4.1) that the amplitude of the wave, which corresponds to the main Rossby wave described above, seems to increase as it propagates westward indicating the existence of a positive ocean-atmosphere feedback producing an unstable mode growing in amplitude. We have not tested yet the possibility of a coupling between the oceanic and atmospheric waves although their periods give us a good reason to think so.

So is there a real coupled Rossby mode taking place in this process and is this responsible for the features observed in the oceanic Rossby waves propagation?

Following the same technique of analysis pursued in previous sections, we proceed to try correlate the signals identified in the ocean-atmosphere data sets and find a coupled mode of variability associated with the patterns described with standard and complex EOF analysis.

4.4 The coupled Rossby wave

Canonical Correlation Analysis (CCA) is a powerful multivariate linear statistical methodology that identifies and isolates correlated patterns between two fields (Bretherton et al., 1992; von Storch and Navarra, 1999; von Storch and Zwiers, 2001). A way of reducing the intrinsic noise and possible spurious patterns was first proposed by Barnett and Preisendorfer (1987), whereby the CCA is performed after transforming the original fields into a EOF space.

Hence our subset of re-normalised leading EOF patterns and PCs are used as a base for the CCA analysis. A singular value decomposition (SVD) of the cross-covariance of an oceanic and an atmospheric variable will produce pairs of patterns - the Canonical Correlation Patterns (CCP) - maximising the correlation coefficient between them. The eigenvalues of the SVD - the canonical Correlation Coefficients (CC) - are ordered in descending order and represent the strength of the linear association between each pair of spatial patterns (more details are given in Appendix A).

CCA is a technique that had been widely used in climatology studies (Barnett and Preisendorfer, 1987; Bretherton et al., 1992; Pierce et al., 2001) and has a close

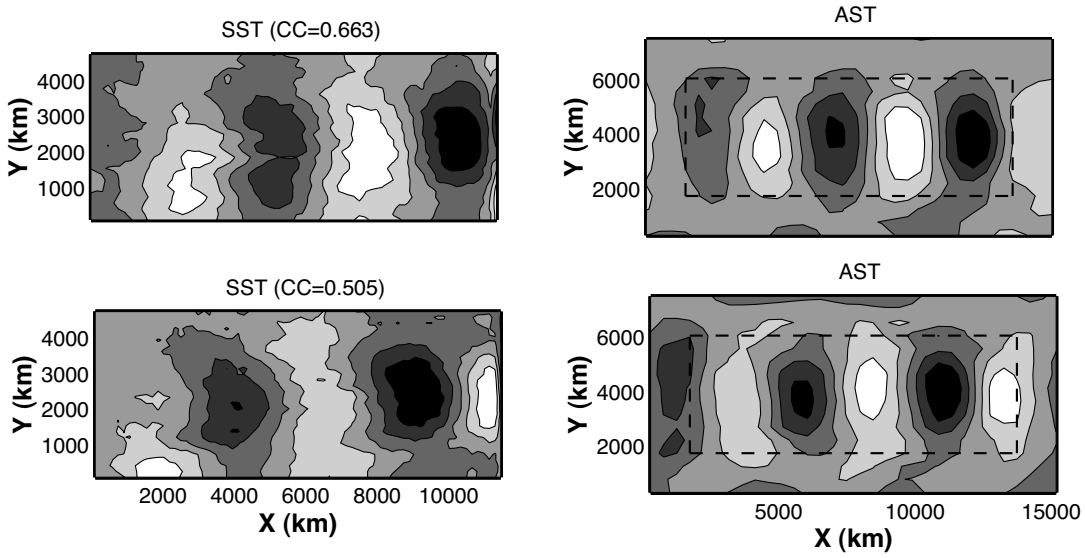

Figure 4.12: *First two Canonical Correlation Patterns of the SST-AST analysis with their respective canonical correlation values. SSTs are in phase in CCP-2. The rectangular dashed box in the atmospheric panels stands for the ocean basin domain. Negative weights are shaded.*

relationship with the standard SVD technique. When the CCA is applied to the investigation of coupled modes between two geophysical fields it is believed to be more efficient than the SVD technique because its temporal CC (equivalent to the PCs in the EOF analysis) are more correlated than the PCs from the SVD analysis for each pair of patterns (Venegas, 2001) and because the SVD has more chances of producing spurious patterns and correlations (Cherry, 1996). The CCA in EOF space is, by definition, even more accurate. However, one must be cautious when using any correlation-based analysis as the identification of a high association does not necessarily reflect any physical pattern or exclude the interaction of a third variable (Cherry, 1996; Venegas, 2001; von Storch and Zwiers, 2001).

We will again focus on the results at $\phi = 40°$ discussing only the differences for the other central latitude. We thus perform the CCA on the unfiltered EOFs and compute the first six CCP between all oceanic and atmospheric variables, ordered in descending order of importance.

The patterns obtained can be divided into two groups. A strong correlation between some oceanic and atmospheric vectors with a baroclinic response in the atmosphere, and a less strong correlation, but still very significant, where the concept of "equilibration" (Shutts, 1987) takes place and the atmosphere is equivalent barotropic. In the latter, quasi-stationary atmospheric waves are forced by an external thermal source, i.e. oceanic temperature anomalies, and can actively couple with the oceanic SST giving rise to resonance (Held, 1983; Frankignoul, 1985; Colin de

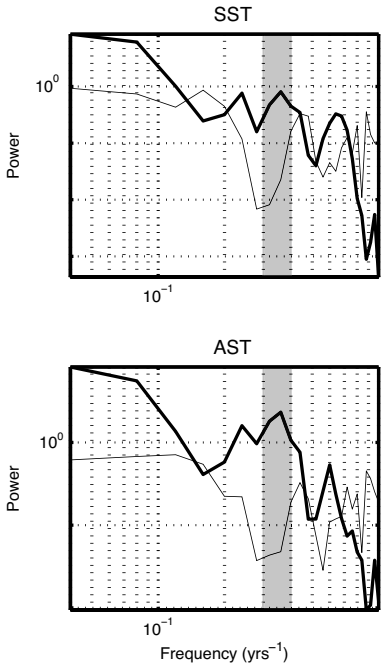

Figure 4.13: *Spectra of the modes of Fig.4.12. Thin line: first mode; thick line second mode. The first CCP correlation takes place at short periods, while the second CCP has a definite period of ∼3 yr that corresponds to the main Rossby wave propagating at* $\phi = 40°$.

Verdière and Blanc, 2001). The equilibrated atmospheric wavenumber-3 response observed so far (see for example Fig.4.11) is also found in Goodman and Marshall (1999) and **??** as the resonant regime where their coupled mode possesses maximum growth and is the wavenumber at which equivalent barotropic external Rossby waves resonate to localised thermal forcing (Held, 1983).

This is exactly the atmospheric configuration of the fastest growing mode proposed by Goodman and Marshall (1999), in which high (low) pressure anomalies are associated with warm (cold) SST, growing in amplitude with height.

Baroclinic and equivalent barotropic structures have been both modelled and observed; an appropriate simulation of the eddy feedback is believed to be crucial for the generation of equivalent barotropic responses, as reviewed by Ferreira and Frankignoul (2005). Moreover, the atmospheric structure is frequency dependent with baroclinic responses dominating at interdecadal periods and equivalent barotropic atmospheres present for interannual periods (Colin de Verdière and Blanc, 2001).

The atmospheric response to SST forcing has been studied extensively and under different approaches (Latif and Barnett, 1994, 1996; Nilsson, 2001; Liu and Wu, 2004). In our model, heat flux exchanges between the ocean and atmosphere components are directly expressed through both mixed layers by their respective temperature equations. The correlation between SST and AST is thus expected to be very high as the SST-AST feedback takes place at short time scales and locally

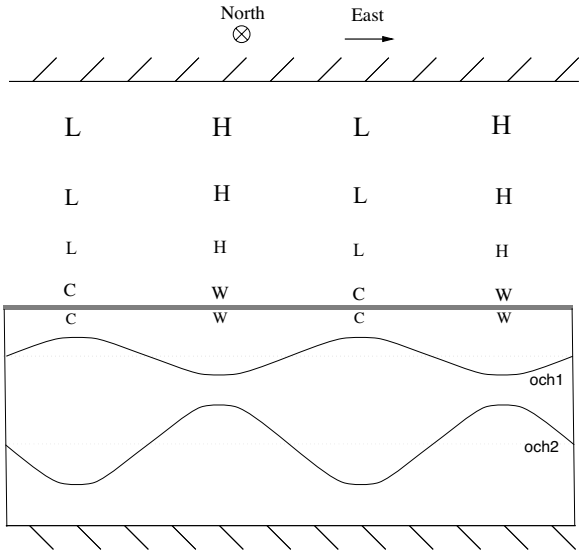

Figure 4.14: *Phase relationships between ocean and atmosphere for the fastest growing mode of Goodman and Marshall (1999) extended to our 3-layer model [adapted from Goodman and Marshall (1999)]. Atmospheric pressures are denoted by symbols H and L, the size of the symbols relates to the magnitude of the anomaly. Symbols W and C refer to warm and cold SST while the undulating lines indicate the positions of the oceanic interface heights.*

in space (Pierce et al., 2001).

Indeed in Fig.4.12 CCP-1 and CCP-2 are characterised by high correlations and in both modes SSTs are found to be in phase with ASTs.

Fig.4.13 shows the spectra of CCP-1 (thin line) and CCP-2 (thick line) for the CCA analysis between oceanic and atmospheric temperatures. CCP-1, the strongest correlated pattern, takes place at high frequencies, with peaks at P=1.5 yr and 2.5 yr, not corresponding to any particular energy peak for Rossby wave propagation at this central latitude. CCP-2 however peaks at $P \sim$3 yr, exactly like the Rossby wave identified in the CEOF analysis does. We will show that this pattern is repeated in all different CCPs, where the most correlated mode, CCP-1, has a baroclinic atmospheric response at periods unrelated to the main Rossby wave while CCP-2 has an equivalent barotropic atmosphere structure with the oceanic Rossby wave coupled underneath.

At this stage it should be useful to remember the mechanism proposed by Goodman and Marshall (1999) through which they found growing decadal Rossby waves propagating as coupled modes in the ocean-atmosphere system in their idealised analytical study. Their fastest growing coupled mode was given by the phase relationship schematised in Fig.4.14 corresponding to both their "entrainment case" and "advective case". The only situation in which a coupled mode can develop is when the atmosphere is equilibrated, or is in an equivalent barotropic structure, with amplitudes of anomalies increasing with height. High (low) pressures cause anomalous down-(up-)ward Ekman pumping that deepens (shoals) the first interface height leading to warm (cold) SST anomalies. Therefore the resulting phase

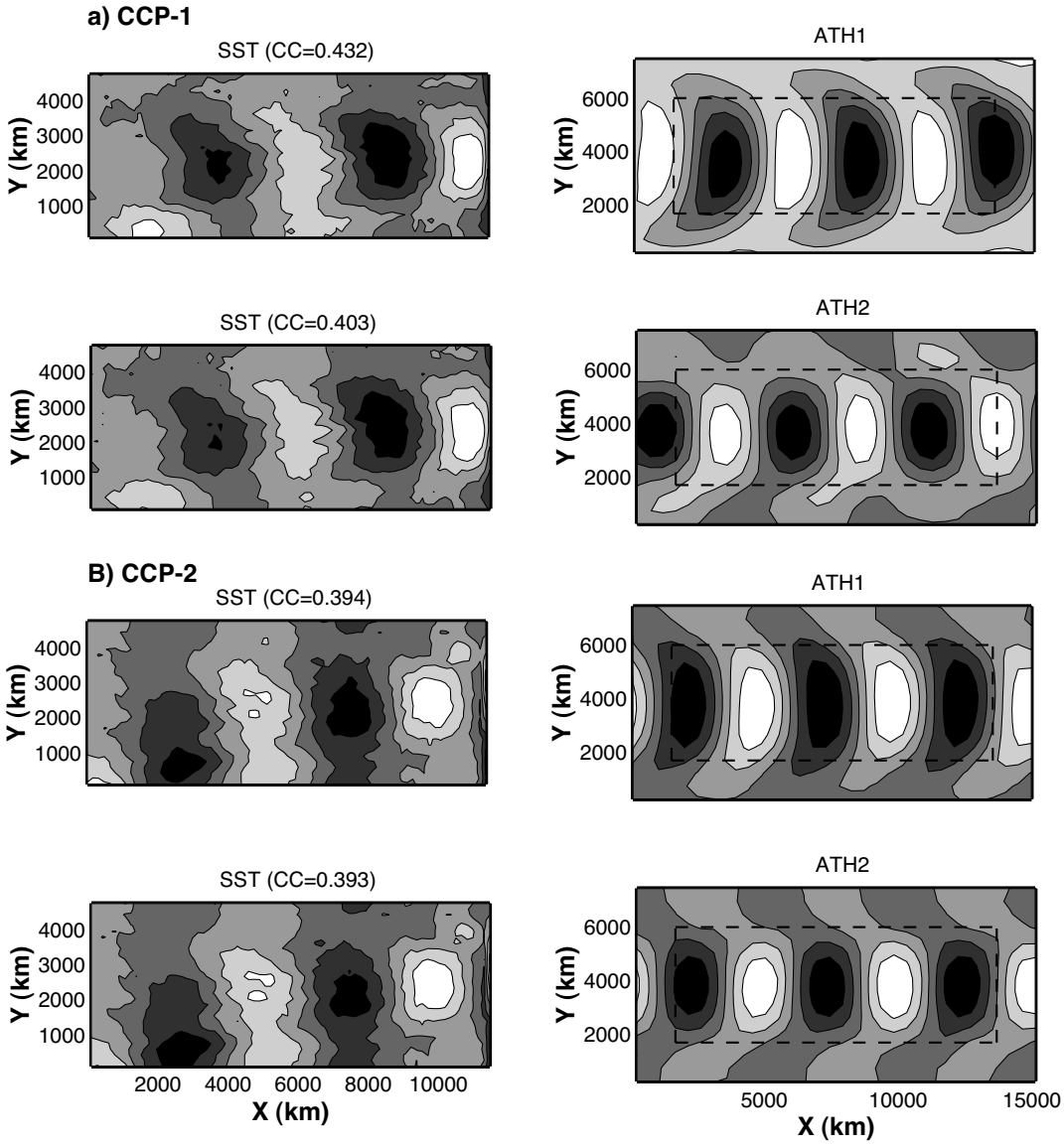

Figure 4.15: *A) Top four panels: CCP-1. Warm SSTs are 90° out of phase with high atmospheric pressures but with a phase shift while the atmospheric structure is baroclinic. B) Bottom four panels: CCP-2. Warm SSTs are in phase with high atmospheric pressures and negative atmospheric interface heights. The atmospheric structure in the first and second mode, corresponding to the coupled Rossby wave mode, is equivalent barotropic.*

relationships are equivalent barotropic positive pressure anomalies on top of warm SST and downward displacement of OCH1 and the opposite for negative atmospheric pressure anomalies. Goodman and Marshall (1999) found that both cases - entrainment and advective dominated - were equally important but the entrainment case produced the biggest growth rate. The advection mechanism, rather than the vertical entrainment, is thought to be both more important and efficient within Rossby wave dynamics and it has been theorised that anomalous meridional geo-

strophic advection of SST by westward-travelling Rossby waves is the link in the ocean-atmosphere coupling leading to growing coupled waves (White et al., 1998; White, 2000b). Later, we will try to identify which of the two mechanisms is active in our simulations by partially decoupling the SST equation in the ocean.

Inspection of the second CCPs of the SST-ATH1 and SST-ATH2 analyses (Fig.4.15) reveals that warm SSTs are indeed underneath low ATH1 (high pressures) and vice-versa with an equivalent barotropic atmosphere. This corresponds to the case described by CCP-2 of Fig.4.12 in which SSTs are in phase with ASTs and peaks at the Rossby wave period. Instead, the first CCP of the SST-ATH1 and SST-ATH2 analysis has a baroclinic atmosphere, corresponding to CCP-1 of Fig.4.12 with a clear phase shift between SST and ATH1. In both CCPs the correlation is relatively strong.

We observed that phase shifts between SST and ATH1 occur in CCP-1 (these are very small and difficult to detect with a single example). Although direct comparisons with, for example, the works of Frankignoul (1985), Shutts (1987) and Goodman and Marshall (1999) can be difficult because of the inclusion of both an atmospheric and an oceanic temperature equation in the Q-GCM, without parameterizations of a forcing function as in the aforementioned studies, the phase shift would always imply a baroclinic response in the atmospheric pressure field.

The spectra of their canonical coefficients, together with the SST-ATPA1 and SST-ATPA2 spectra, are shown in Fig.4.16 and confirm what was previously said for the SST-AST evolution. In all four pairs of spectra in Fig.4.16 the main coupled peak is characterised by a period of 3 yr for the second mode (thick line) while for the first baroclinic mode (thin line) there is evidence of a coupling taking place at decadal periods. This might be related to the interdecadal periods at which the atmosphere responds in a baroclinic way (Colin de Verdière and Blanc, 2001).

The second strongest relationship between the ocean and atmosphere is then equivalent barotropic. The ocean should always be in a baroclinic state and the phase relationships between OCH1, OCH2 and atmospheric temperature are well reproduced in the CCA analysis as depicted in Fig.4.17. Here the ocean is again baroclinic resembling the structures identified in Fig.4.6 for the Rossby wave. The first ocean interface height is out of phase with the atmospheric temperature because this last is phase-locked with SST. The correlation coefficient is diminished for OCH2 but still significantly high. The corresponding spectra are also analysed and while OCH1-AST peaks at the Rossby wave period, P=3 yr, we could not find the appropriate peak for the thermocline displacement, possibly because the strength of the correlation was weak in this case. We were able to trace the Rossby wave period in the thermocline patterns during other analysis, as for example in

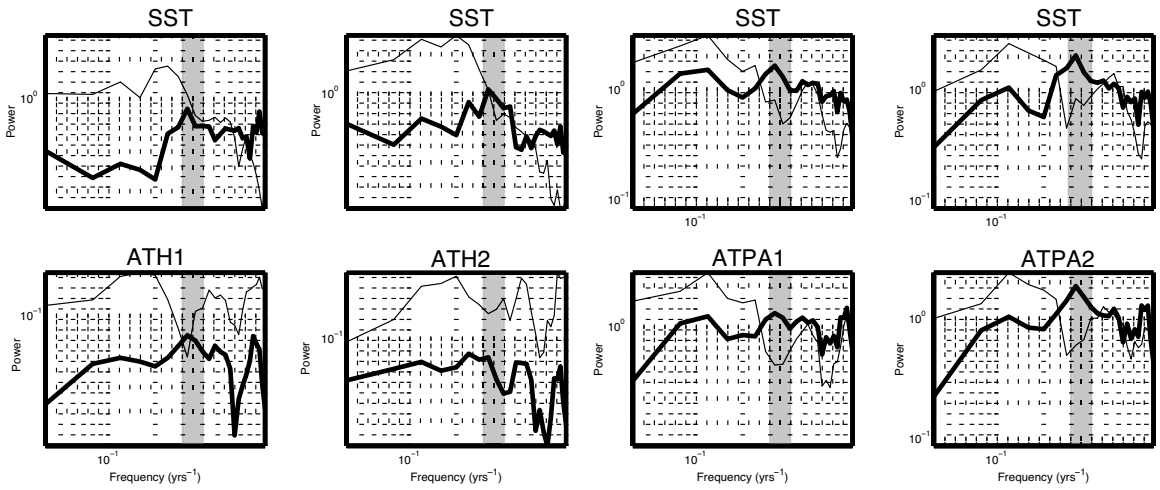

Figure 4.16: *Normalised spectra of, from left to right, SST-ATH1, SST-ATH2, SST-ATPA1 and SST-ATPA2. Thin lines are for CCP-1 and thick lines for CCP-2. The second correlation occurs at P=3 yr between an oceanic baroclinic Rossby wave and equivalent barotropic atmospheric wave. The first correlated pattern seems to have at 5 to 10 yr.*

the canonical correlation of OCH2-ATH1 and OCH2-ATH2 whose spectra are again shown in Fig.4.18, although the peak is not as sharp but distributed over a small amount of frequencies. Other results could have been shown but they all reflect the same mechanism and phase relationship described so far. An example involving both the baroclinicity of the ocean and the equivalent barotropic structure of the atmosphere is given by the OCH2-ATPA analysis. In Fig.4.19 the atmosphere is clearly responding in the "equilibrated" way while thermocline anomalies are in phase with atmospheric pressures and OCH1 (not shown) is out of phase with respect to these.

So far, we have described the behaviour of the coupled system at ϕ=40°. To include the patterns and spectra for ϕ=30° would have been most of the time repetitive as the main features remain the same; significant differences between the two runs exist though. The coupled patterns observed when the model is moved towards the Equator are less coherent and the correlations much weaker. The spectra of the canonical analysis still peak at the Rossby wave main period with an equivalent barotropic atmosphere above it but it is more difficult to differentiate the modes associated with the baroclinic Rossby wave and its relation with the equilibrated atmosphere. This seems to indicate a weaker coupling of the ocean-atmosphere system under the mechanism described for higher latitudes. An explanation might be given by the period of the main ocean wave involved in the coupling. Oceanic Rossby waves have a meridional profile for their zonal phase speed, with westward phase speeds decreasing as the inverse square of the latitude (Gill, 1982). It is possible

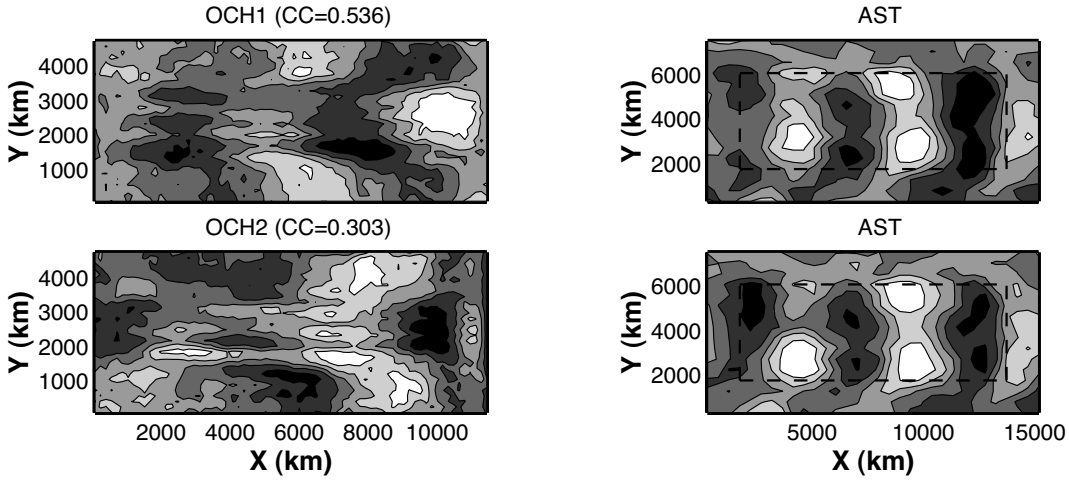

Figure 4.17: *CCP-2 of the OCH1-AST (cc=0.536) and OCH2-AST (cc=0.303) correlation. The ocean has a Rossby wave-like structure with cold atmospheric temperature anomalies over positive interface anomalies.*

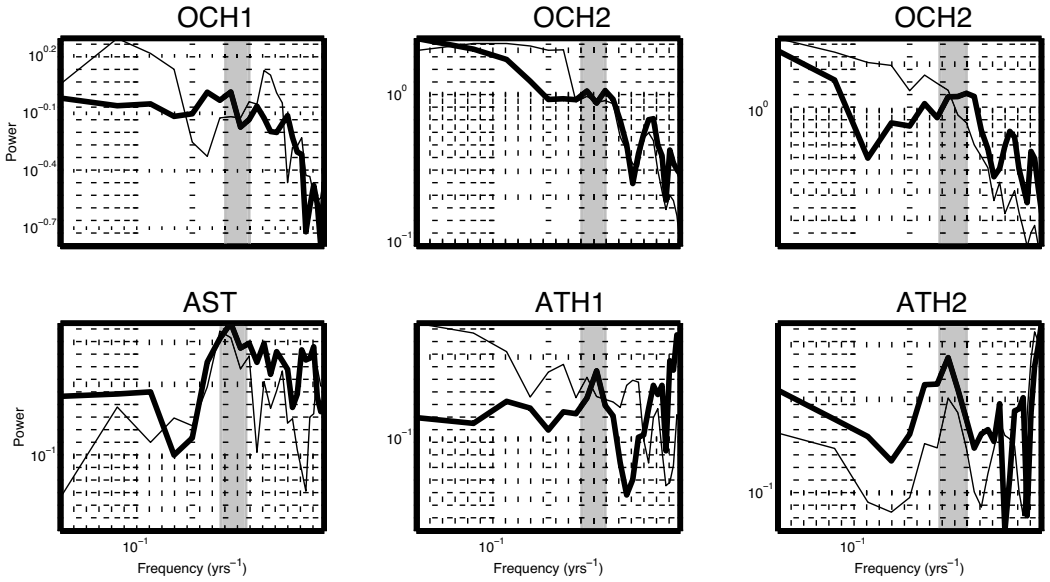

Figure 4.18: *Normalised spectra for CCP-1 (thin line) and CCP-2 (thick line) of the OCH1-AST (left panels), OCH2-ATH1 (middle panels) and OCH2-ATH2 (right panels) correlation analyses.*

that oceanic Rossby wave speeds, as we move towards the Equator, become too fast to maintain the phase relationship necessary to induce the equilibrated atmospheric waves that are able to positively couple with the external thermal forcing. In order to test this hypothesis we should perform other runs at different latitudes and confirm whether a band of latitudes at which the coupling is maximised really exists.

This however goes together with the latitude-dependent instability mechanism acting on the Rossby wave. LaCasce and Pedlosky (2004) computed the distance a

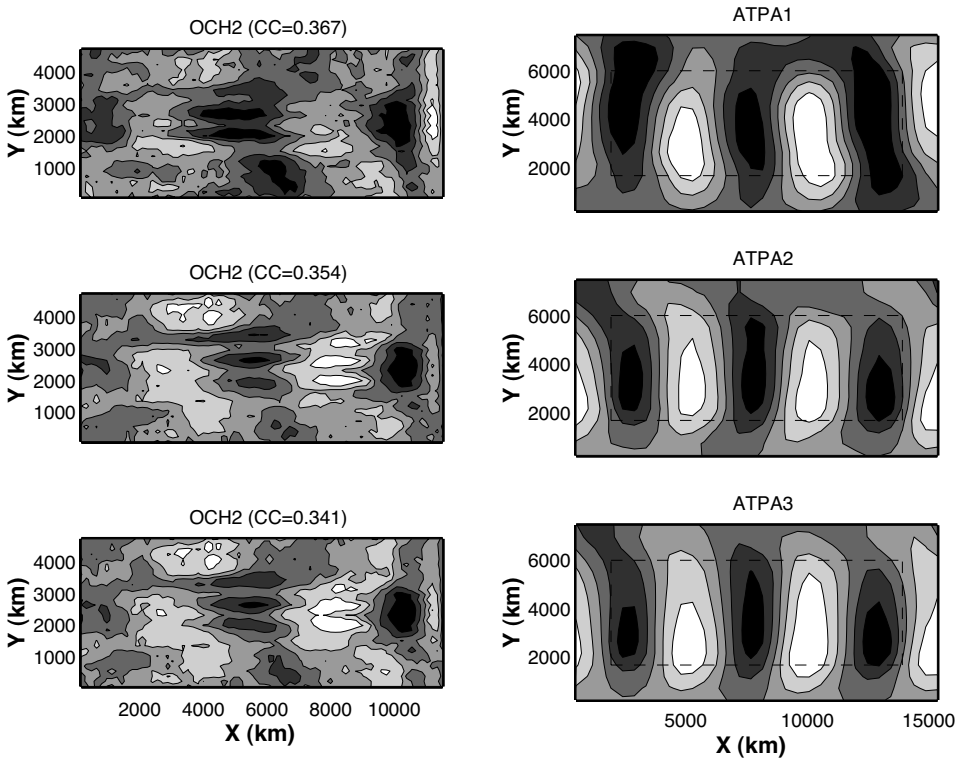

Figure 4.19: *CCP-2 of the OCH2-ATPA1, OCH2-ATPA2 and OCH2-ATPA3 correlation analyses. The baroclinic oceanic Rossby wave has positive thermocline anomalies beneath high atmospheric pressures, which have an equivalent barotropic structure. OCH1, as sketched in Fig.4.14 would be out of phase with ATPA1.*

plane wave could travel before being destroyed by the instabilities. In their best case, a wave at ϕ=40° could propagate 1×10^3km and a Rossby wave at ϕ=30° a maximum of 2.5×10^3km (their Figure 10). Inspecting several Hovmöller plots similar to the ones in Fig.4.1, we estimated distances of propagation of $\sim5\times10^3$km and $\sim7\times10^3$km for waves at ϕ=40° and 30° respectively, then the wave begins to be destroyed by the instability. This means that, although Rossby waves are clearly observed to propagate longer and with a more compact structure at lower latitudes, the biggest influence of the ocean-atmosphere coupling is acting upon waves propagating at higher latitudes increasing their resistance to instability processes. This could also be an explanation for the greater increase in phase speeds found with the FFT analysis at ϕ=40°: since the coupling is stronger there, a potential coupling speed-up should also be stronger at that latitude.

4.4.1 The importance of horizontal advection and entrainment of temperature anomalies

Goodman and Marshall (1999) proposed two different but equally important mechanisms for the generation of SST anomalies causing a positive ocean-atmosphere feedback. The first is the entrainment mode, in which vertical advection processes during the transit of the oceanic wave generate anomalous warm and cold SSTs. When the atmosphere response is equilibrated, the anomalous Ekman pumping will work to reinforce the SST anomalies and the amplitude of the wave. The second mechanism is the advection mode, in this case the horizontal advection of mean SST by geostrophic flow generated by undulations in the ocean's interfaces is responsible for establishing SST anomalies out of phase with the first interface height. The latter case was involved in the unstable coupled interactions of Qiu et al. (1997) and van der Avoird et al. (2002). For instance, the coupled instability of van der Avoird et al. (2002) was due to horizontal advective processes only, having neglected entrainment in the ocean.

By modifying the SST equation in order to suppress one or the other mechanism, we will try to understand which mode is responsible for the couple Rossby wave in our model.

The entrainment mode

We will first eliminate the horizontal advective terms in the SST tendency equation, in this case (3.3) reduces to the entrainment-only case:

$$\partial_t T = \frac{w_{oek}}{H_m} T + K_2 \nabla^2 T - K_4 \nabla^4 T - \frac{F_0 - F_m}{\rho_o C_{po} H_m}. \tag{4.1}$$

Thus, vertical entrainment through interfaces is still active but the ocean circulation is not able to advect the temperature field. We continued the previous run at ϕ=40° for another 50 years and investigated the correlation and wave response in all oceanic and atmospheric variables. The spatial patterns of the second most correlated mode between SST, ATH1 and ATH2 are shown in Fig.4.20. The SST patterns are much smoother but still resemble the patterns related to the Rossby wave propagation plotted in Fig.4.15 for CCP-2. Also, the atmospheric response is again a wavenumber-3 equilibrated wave. The spatial relationship between the different variables is maintained for the coupled Rossby mode with the same shared peak at P ∼3 yr (not shown). Only the correlation coefficients are significantly different, having decreased, for the case shown, to 0.350 for the SST-ATH1 analysis and 0.292 for the SST-ATH2 analysis.

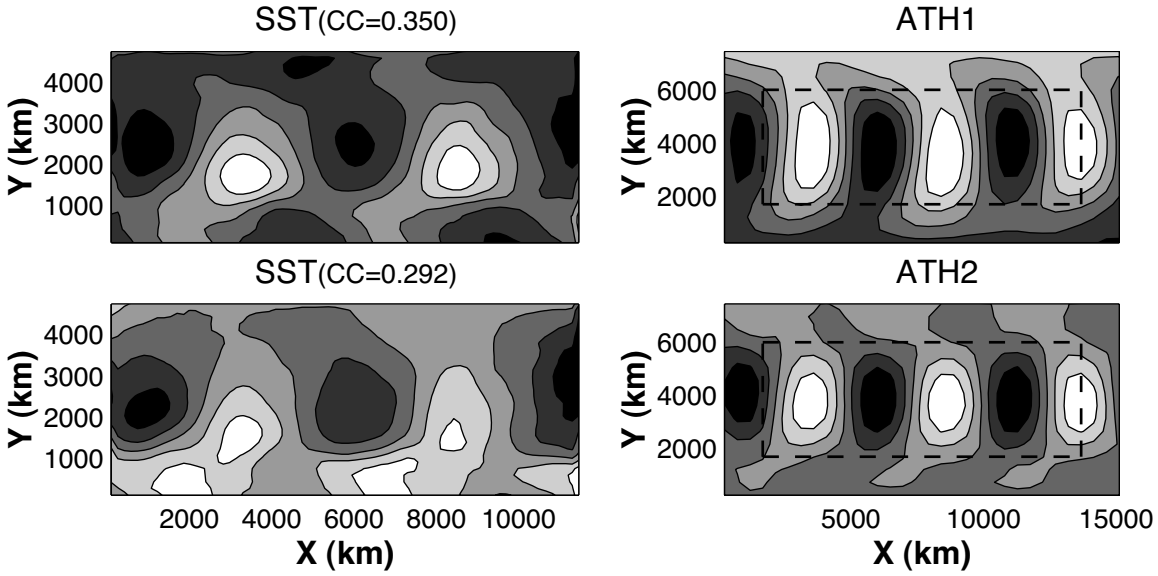

Figure 4.20: *Second canonical correlation patterns of SST-ATH1 and SST-ATH2 for the case with no advection of oceanic temperature anomalies. Phase relationship are conserved and the atmospheric response is equivalent barotropic. However, correlation coefficients are weaker (SST-ATH1 CC=0.350, SST-ATH2 CC=0.292).*

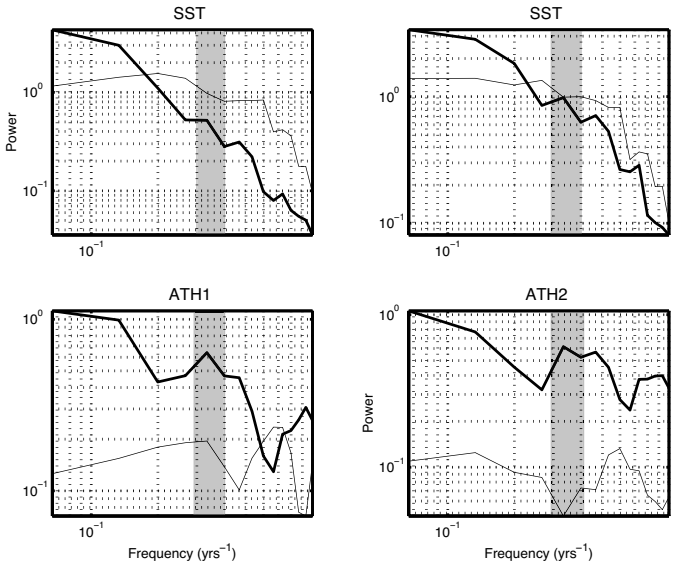

Figure 4.21: *Spectra of the SST-ATH1 and SST-ATH2 canonical correlation analyses for CCP-1 (thin lines) and CCP-2 (thick lines) of Fig.4.20. The shaded area in all plots ranges between 0.3 and 0.4 s^{-1} and highlights the common Rossby peak at $P = 3$ yr.*

The spectra of the PCs reveal the existence of the Rossby wave peak in both the oceanic and the atmospheric variables with little difference with the case for the full SST equation. Indeed, in Fig.4.21 are plotted the spectra of the first (thin lines) and second (thick lines) CCP of the SST-ATH1 and SST-ATH2 analyses: the shared Rossby peak is strong in the oceanic temperature and atmospheric heights while there has been an increase in the variance at lower frequencies.

Overall, the results obtained with the entrainment-only SST equation are very similar to the full-SST analyses and the coupled Rossby wave is still generated with similar characteristics without the horizontal advection of temperature anomalies. This result underlines the importance of the entrainment processes of SST for the generation and maintenance of the coupled mode while not requiring advection by the ocean circulation. However, the correlation between the ocean and atmosphere in the coupled mode are much weaker indicating that when both horizontal and vertical processes are present they mutually work to reinforce the equilibrated atmospheric response and the resulting positive feedback.

The advective mode

In order to suppress entrainment in the mixed layer and retain horizontal advective processes only, entrainment heat fluxes defined in (3.4) are set to zero and (3.3) now reads

$$\partial_t T + \mathbf{u} \cdot \nabla T = K_2 \nabla^2 T - K_4 \nabla^4 T - \frac{F_0}{\rho_o C_{po} H_m}. \tag{4.2}$$

Similarly as for the entrainment mode case, we continued the run for 50 years and the results of the CCA analyses between SST and ATH1-ATH2 are shown in Fig.4.22.

There is no trace left of the equilibrated response in the atmosphere and the two most correlated pattern show a baroclinic atmospheric wave with high correlation coefficients (SST-ATH1 CC=0.417 and SST-ATH2 CC=0.405 for mode-1; SST-ATH1 CC=0.396 and SST-ATH2 CC=0.353 for mode-2). The spectra of the first four most correlated patterns (bottom panels of Fig.4.22) reveal no peak at the Rossby wave period for ATH1 and ATH2.

Therefore we conclude that the advective mode alone is not able to sustain the coupled Rossby wave in our model and only in the presence of entrainment processes can the coupled oscillation develop. Following these results we believe that entrainment fluxes in the ocean cannot be neglected, as some authors did (Qiu et al., 1997; van der Avoird et al., 2002)), if a coupled instability of the Goodman and Marshall (1999) type is pursued.

A different test on the coupling could also be performed by removing the fluxes at the top of the mixed layer, F_0, and therefore testing the need of thermodynamical forcing on the existence of the coupled mode; in this case we could qualitatively define the coupled Rossby wave as thermodynamically or mechanically driven, or a mix of both.

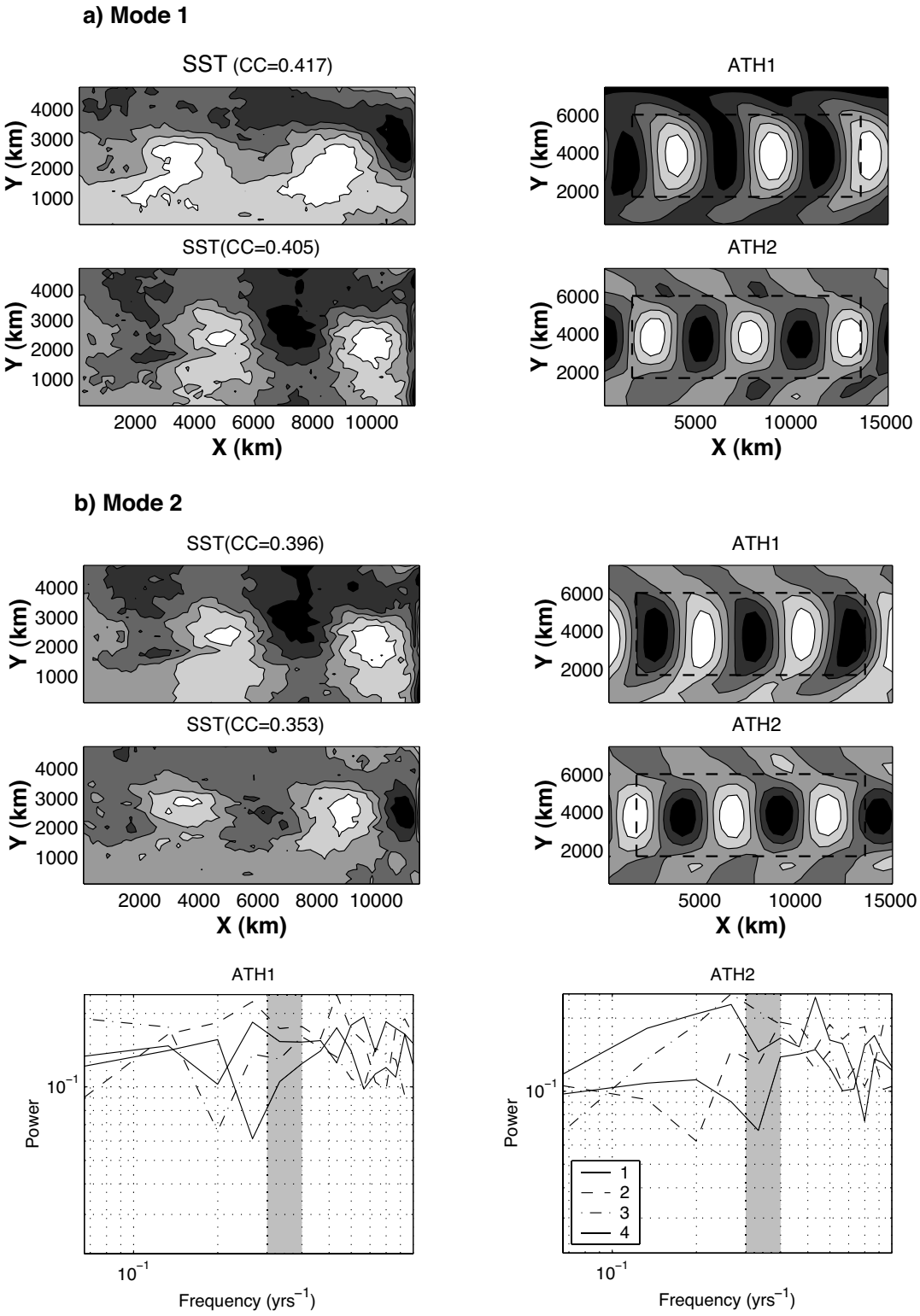

Figure 4.22: *First two most correlated patterns of the SST-ATH1 and SST-ATH2 CCA analyses for the advective-only SST. Both CCP-1 and CCP-2 show a baroclinic response in the atmosphere and the equivalent barotropic structure is absent in the remaining modes. The ATH1 and ATH2 spectra of the first four modes do not peak at the Rossby wave period as expected (bottom panels).*

4.5 Relationship with Rossby basin modes

Rossby waves reflecting in bounded basins generate the so-called Rossby basin modes. These are formed by long Rossby waves with westward group velocities and short reflected Rossby waves with eastward group velocities; the theory of unforced Rossby basin modes is well known (Pedlosky, 1987). Recently, new theoretical works addressed this problem using an equivalent integral mass conservation condition in QG dynamics (Cessi and Primeau, 2001; LaCasce and Pedlosky, 2002) resulting in a new class of weakly-dissipated basin modes. These results have attracted considerable attention and generated several theoretical studies. We will not try to address any of the issues raised in Rossby basin modes theory but only discuss the possibility of finding such modes in our model and whether they are involved in the atmospheric coupling.

The basin modes discussed in LaCasce and Pedlosky (2002) and LaCasce and Pedlosky (2004) resemble free long Rossby waves with zonal wavelengths that are multiples of the basin width. They were found to be easily excited by an analytical wind stress and are believed to be able to effeciently couple with the atmosphere because of their weak dissipation (Cessi and Paparella, 2001).

For a layered ocean, in the inviscid linear case, the PV equation reads

$$\partial_t[\nabla^2\psi - F\psi]_t + \beta\psi_x = 0 \tag{4.3}$$

with $F = a^{-2}$, where a is the Rossby radius of deformation.

Looking for solutions of the kind $\psi = \Psi exp[-i(\gamma x + \sigma t)]$, where $\gamma = \beta(2\sigma_{m,n})^{-1}$, we find the solutions for the stream functions as mode oscillations in a rectangular basin with sides a and b (Longuet-Higgins, 1965)

$$\Psi = cos(\gamma x + \sigma_{m,n}t)sin(m\pi x a^{-1})sin(n\pi y b^{-1}), \tag{4.4}$$

where m,n are the nodes in the x and y direction and whose frequencies are given by

$$\sigma_{m,n} = \beta/2\Big[m^2\pi^2a^{-2} + n^2\pi^2b^{-2} + F\Big]^{-1/2}. \tag{4.5}$$

Their phase velocities are readily found to be

$$C_x = -\sigma_{m,n}\gamma^{-1} = -\frac{\beta}{2}[\pi^2m^2a^{-2} + \pi^2n^2a^{-2} + F]^{-1}. \tag{4.6}$$

Although the group velocity of barotropic Rossby waves is much higher than the velocity of the mean circulation away from boundaries, making Rossby wave dynamics close to be linear and inviscid (Sheremet et al., 1997), this is not true in the baroclinic case and both viscosity and the mean flow modify the basin modes

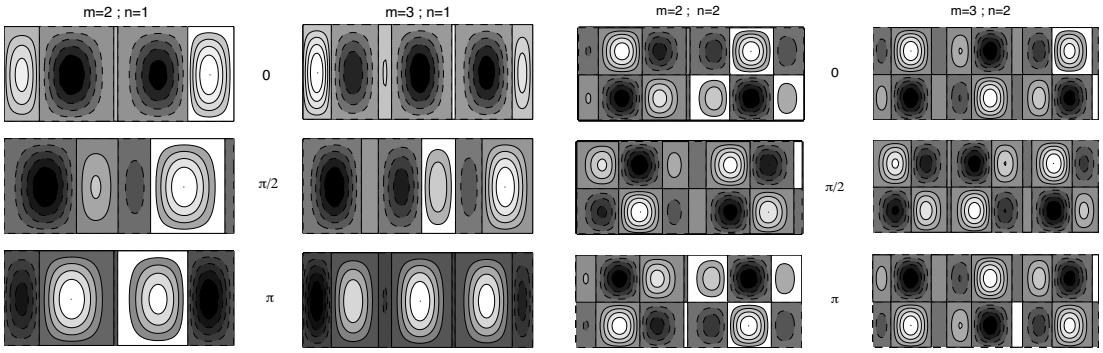

Figure 4.23: *Examples of baroclinic planetary basin modes propagating westward in an ocean domain similar to the one used in this study for* $\phi = 40°$.

of Rossby waves. We will not try to model these effects or even the mass-conseving boundary condition used in LaCasce and Pedlosky (2002), focusing on the simple free and inviscid case.

Using our first Rossby radius of deformation for both central latitudes and the dimension of our ocean basin we get phase velocities of around 2.8 and 4.9 cm/s for ϕ=30° and 40° respectively. These are approximately the phase speeds of the Rossby waves in our model and their shape can be seen in Fig.4.23 for different combinations of nodes.

LaCasce and Pedlosky (2004) points out that in QG dynamics the new class of basin modes would have meridional crests parallel to the north-south boundary and in fact we see this happening in the first CEOF of Fig.4.4, for example. But these are not the modes that we found to be involved in positive feedback with the atmosphere. The second kind of modes, with wave crests not parallel with the boundaries and found in both the CEOF and the CCA analysis, is responsible for the phase relationship highlighted so far similar to the one introduced by Goodman and Marshall (1999). We conclude that, although the basin modes shown in Fig.4.23 have similarities with the ones found in the previous studies and the mechanisms of positive coupling between these basin modes and the atmosphere might still take place, the new class of weakly damped modes made of free long Rossby waves studied by LaCasce and Pedlosky (2002, 2004) do not take part in the Rossby wave coupled mode.

4.6 A forced solution

To test the previous hypotheses that the coupled feedback between the oceanic Rossby wave and the equilibrated atmosphere can induce changes in the Rossby wave phase speed and stability, we employed the Q-GCM in an ocean-only configuration. The ocean is forced by winds and heat fluxes computed from the previous coupled simulations, the runs are continued for an extra 150 model years and the Rossby wave response is analysed in a *forced* and not *coupled* framework.

In the Hovmöller plots of Fig.4.24 there is evidence of stronger instabilities occurring at both central latitudes and the Rossby waves cannot travel as far as in the coupled case. In fact, waves are observed to travel only up to 3.5×10^3 km at $\phi = 40^o$ and 5×10^3 km at $\phi = 30^o$, which is around 2×10^3 km less than in the coupled case. However, these distances are still greater than the ones predicted by LaCasce and Pedlosky (2004), where Rossby waves propagation was studied in a two layer unforced model.

So far, the results seem to agree on the hypothesis that the coupled feedback sustains Rossby wave propagation against instabilities but can we also discern a difference in the speed of propagation? The FFT analyses of the westward filtered OCH2 from the forced runs reveal a significant slow down of the Rossby wave speed

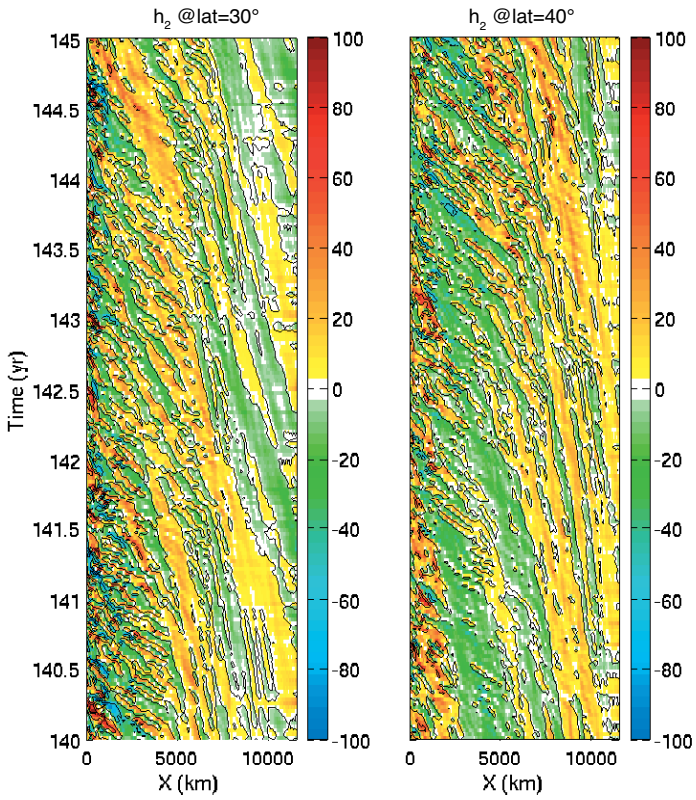

Figure 4.24: *Hovmöller plots of the second interface heights OCH2 (in meters), representative of the thermocline displacements, for $\phi = 30^o$ and 40^o. Note the increasing breaking of the waves as the latitude increases. Rossby waves are observed to break more and after shorter distances than when the waves are coupled with the atmosphere.*

(Fig.4.25). While the wavelength of the main peaks remain similar to the coupled runs, the frequencies have clearly diminished resulting, for both central latitudes, in slower phase speeds that are now very close to the perturbed dispersion relation. To allow comparison, the position of the main Rossby peak in the coupled runs is indicated by a black circle. Besides, in the western part of the basin the FFT shows higher energetic activity resulting from the intense breaking of the original baroclinic wave.

Thus, both results have been confirmed by the forced experiments. Rossby waves, when coupled to the atmosphere with the mechanism described in the previous sections, receive an energetic input which allows them to partially resist against dissipation and instabilities. The positive feedback with the equivalent barotropic atmospheric wave also induce an extra speed-up, which is added to the one generated by the vertical mean shear. The generation, mechanism and quantification of the atmospheric-induced speed-up will be the subject of future studies.

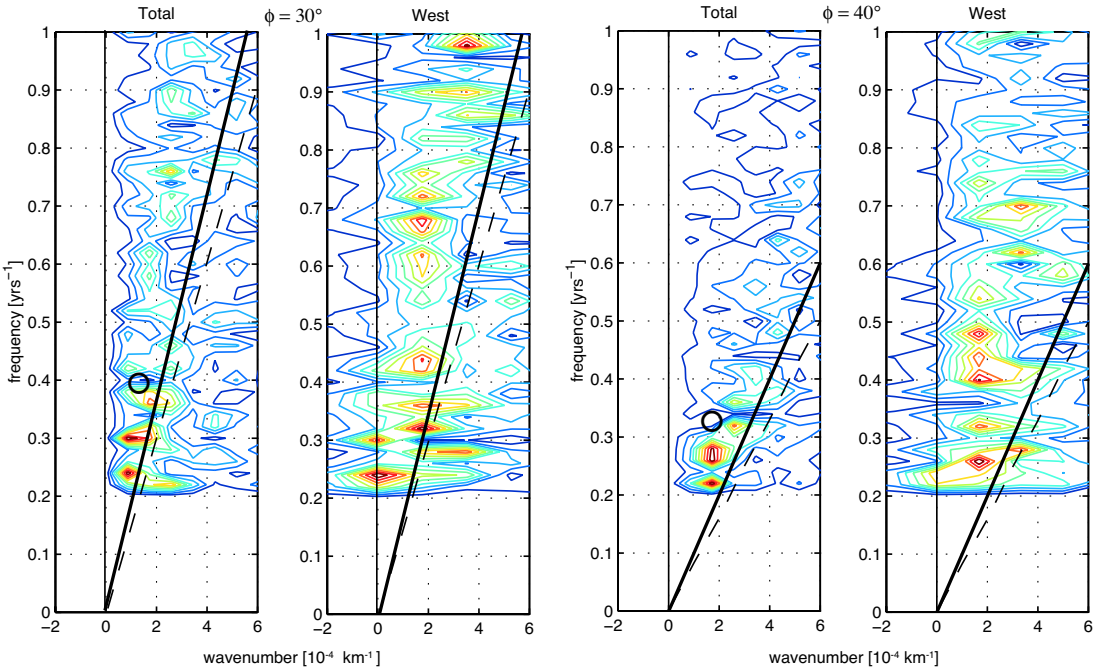

Figure 4.25: *Fast Fourier Transform of the westward filtered OCH2 in the forced runs at $\phi = 30^o$ (left panels) and $\phi = 40^o$ (right panels). The Rossby wave main peaks are considerably slower than in the coupled runs, of which the main peaks are drawn with a black circle. Also, more energetic peaks are found in the western part of the basin, where Rossby wave break into faster waves.*

4.7 Summary and conclusions

Rossby waves have been studied in the framework of a quasi-geostrophic coupled ocean-atmosphere model. The model configuration has three layers in both the oceanic and atmospheric component, the horizontal resolution in the ocean basin is relatively coarse (Δx=40 km) and viscosities between layers are chosen to be as low as possible. The oceanic domain was chosen to be relatively wide, resulting in a "Pacific-like" basin of ∼11500 km.

Two classes of waves were identified: a baroclinic slow wave and fast barotropic waves resulting from the instability and breaking of the first. These results are in partial disagreement with LaCasce and Pedlosky (2004) as the slow baroclinic Rossby wave is able to propagate far longer distances than suggested in the aforementioned theoretical work. The characteristics of Rossby waves in the ocean and atmosphere have been identified with statistical eigenvalue techniques for the two central latitudes considered (ϕ=30° and 40°). An equivalent barotropic atmospheric wave was found to travel westward with similar periods as, and in phase-lock with, the oceanic baroclinic Rossby wave suggesting a coupling between the two. Linear nearly stationary equivalent barotropic atmospheric waves can be generated by, for example, a thermal forcing (Held, 1983); in a coupled system these equilibrated waves can represent the quasi-stationary atmospheric waves that couple with the oceanic SST anomalies (Frankignoul, 1985; Goodman and Marshall, 1999; Colin de Verdière and Blanc, 2001; Kravtsov et al., 2005c).

Following a statistical correlation analysis, a clear coupled Rossby wave mode, coherent in all oceanic and atmospheric variables was found. The coupled Rossby wave mode has spatial characteristics and periods of the main baroclinic oceanic Rossby waves in the system and resemble the unstable coupled mode mechanism proposed by Goodman and Marshall (1999). The correlation coefficients are generally stronger for the case at $\phi = 40^0$ and the spatial structures are also more coherent. This is a possible indication that coupled Rossby modes are more likely to develop as we move polewards, as the Rossby wave phase speed in the ocean slows down with increasing latitude and positive phase relationships with the quasi-stationary atmospheric response are possible since slowly propagating waves have more time to develop SST anomalies that will in turn influence the overlying atmosphere.

We thus argue that a positive feedback is taking place whereby oceanic Rossby waves are efficiently coupled with an atmospheric equilibrated wave travelling in phase and with the period of the oceanic wave. This mechanism, whether generating an unstable or a weakly-damped coupled mode, is pumping energy into the oceanic Rossby wave, which uses that extra energy to counteract the baroclinic in-

stability processes acting during its propagation. Moreover, partially decoupling the SST tendency equation, the coupled Rossby mode existence has been proved to depend on entrainment processes of SST anomalies, whereas horizontal advection of temperature anomalies would only strengthen the mechanism.

Whether the coupled mode is ocean- or atmosphere-driven is difficult to say from this kind of analysis. Goodman and Marshall (1999) proposed as a source of energy for the development of the coupled mode the release of available potential energy (APE) in the ocean; whereby the atmosphere transforms thermal energy stored in the thermocline to mechanical energy through wind stress. Colin de Verdière and Blanc (2001) instead suggested the atmospheric APE as a source of energy in its thermal resonance process. Which of these is happening in our modelling study could be inferred by studying the down-gradient wave heat fluxes in the atmosphere and ocean as suggested by Colin de Verdière and Blanc (2001).

In a similar study, Kravtsov et al. (2005a) found an interdecadal coupled Rossby mode propagating westward with a time scale given by the crossing time of the oceanic Rossby wave. Using a lagged covariance analysis regressing oceanic and atmospheric fields onto ocean kinetic energy they argued that, as the SST were larger than the AST anomalies, the mode was forced by the ocean and the APE was released from the thermocline in a similar way as in Goodman and Marshall (1999). From the CCA analysis depicted in Fig.4.12 AST anomalies seem slightly larger than SST anomalies, possibly suggesting that the source of energy in our case is in the atmosphere.

The positive coupling with the atmosphere is not only providing energy to the oceanic Rossby wave. In fact, the main peaks in the FFT analysis suggest that the coupling is also able to give an extra speed-up other than the baroclinic main flow effect, as the Rossby waves were found to travel faster than the phase speed computed with the inclusion of the mean zonal flow. The calculations of the perturbed dispersion relations are roughly in agreement with the speed-up values given by de Szoeke and Chelton (1999) for our parameter values and show speed-ups of around 1.2, whereas the coupled Rossby waves are observed to propagate at about twice the unperturbed phase speed. We showed that, when the ocean is simply forced at the surface by winds and heat fluxes with no ocean-atmosphere feedback, these peaks appear at lower frequencies close to the perturbed dispersion relation, indicating that the coupling is indeed a possible mechanism in the speed-up of the observed Rossby waves. Finally, coupling speed-ups are observed to be greater for higher latitudes, because the coupled Rossby wave is stronger there.

Increased phase speeds due to atmospheric coupling have been suggested in different works (White et al., 1998; Ferreira et al., 2001; Colin de Verdière and Blanc,

2001). For instance, White et al. (1998) proposed a zonal and meridional coupling speed due to the interaction between the SST field, generated by meridional advection, and meridional wind anomalies. This extra phase speed was linearly added to the uncoupled linear wave resulting in significant speed-ups at middle and high latitudes. This seems to agree with our results, since a higher increased in phase speeds is observed for higher latitudes. In a later study, White (2000a) studied the coupled response at latitudes lower than 30°, suggesting entrainment processes controlling the negative feedback between SST and the atmospheric response resulting in slower phase speeds. The negative feedbacks proposed in White (2000a) are taking place closer to the Equator and are not possible to reproduce in our QG coupled model. However, a more detailed study of the latitudinal response, ranging from, for example, 25° to 50°, would give us a stronger indication of any variation in the strength of the coupling and subsequent effects in the Rossby wave phase speeds, allowing us also to directly compare our results to observational results such as the ones previously discussed.

Statistical eigentechniques have been useful in the identification of the properties of both oceanic and atmospheric waves. We were also able to characterise the coupled Rossby wave with its spectral and spatial components. However, we do not know if this coupled mode is unstable and at this stage we can only speculate on its most important feature, arguing that the mode is weakly-damped, with a decaying rate diminished by the coupling. This would agree with what Goodman and Marshall (2003) obtained after the inclusion of meridional boundaries for the ocean in their original model (Goodman and Marshall, 1999). They could still identify the presence of the unstable mode but in this case it was found to be weakly damped due to the reflection of Rossby waves at the western boundary.

To corroborate and shed more light onto the results obtained, a linear stability analysis is proposed as the continuation of this study. The coupled eigenmodes of the ocean-atmosphere system will be easily identified after the manipulation of the Q-GCM equations and the construction of a coupled tendency matrix; hopefully the coupled Rossby wave patterns will be reproduced and its eigenspectra will give us information on changes in both frequency and decay rates when different mean state are tested as well as the sensitivity to different parameters. This problem is currently underway. In the next chapter we set-up a high horizontal resolution, 6-layer ocean in order to test the results obtained with the "Pacific-like" basin, and carry out similar analyses. The effects of horizontal resolution and number of layers in the ocean on the coupled mode strength, resulting Rossby wave speed-up and stability are studied in an ocean of reduced dimension, which will represent our "Atlantic-like" experiments.

Chapter 5

Coupled Rossby waves in the Q-GCM: A high-resolution multilayer study

In this chapter we investigate the Rossby wave response in a high-resolution 6-layer ocean of Atlantic-like dimensions. Although the ocean is more turbulent and the responses noisier, coupled Rossby waves of the same kind identified in Chapter 4 are observed and the propagation of the waves is stable throughout the basin. Smaller oceans are therefore capable of generating faster coupled Rossby waves and the tridimensional higher resolution is not found to be enlightening in any of these processes.

5.1 Introduction

In the previous chapter we studied the response of the coupling between a "Pacific-like" ocean and the overlying atmosphere. A positive feedback involving a baroclinic Rossby wave and an equivalent barotropic atmospheric response, in which oceanic Rossby waves can sustain themselves against instabilities, was identified. Also, observations of an additional speed-up (other than the one generated by the mean flow) associated to the coupled Rossby wave were shown. The general characteristics of the model simulations were the presence of a wide oceanic basin (the so-called Pacific-ocean experiments), a 3-layer configuration for both the oceanic and atmospheric component of the coupled model and a relatively coarse resolution in the ocean (40 km). Although a thorough sensitivity study looking at different parameters such as diffusivity, viscosity and strength of the heat flux coefficients could not be carried out due to the computational cost of the lengthy simulations, results from

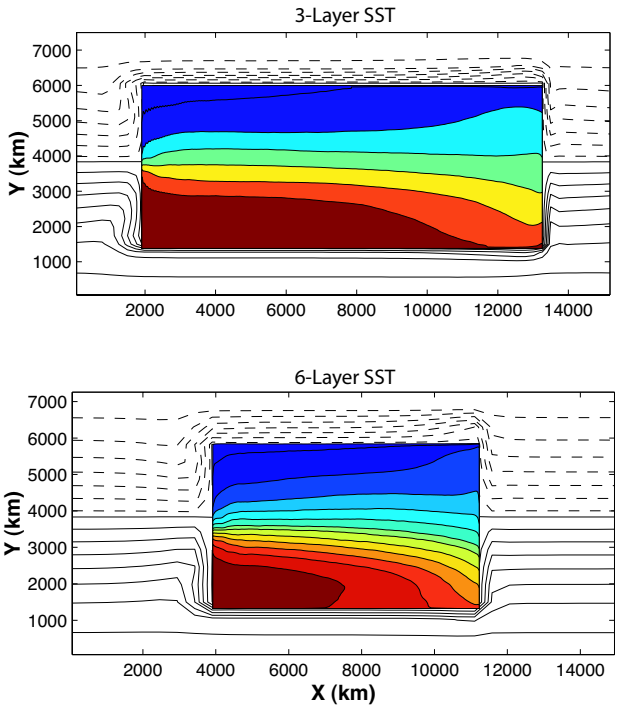

Figure 5.1: *Sea surface temperature anomalies contour for the the 3-layer low-resolution study (upper panel) and the 6-layer high-resolution study (lower panel) and the respective atmospheric temperature fields during the spin-up. Contour interval is arbitrary. The horizontal extension of the ocean basin for the 6-layer experiment is 2/3 of the basin in the 3-layer study.*

a high-resolution ocean basin in both the horizontal and the vertical are presented in this chapter.

The atmospheric component of the model will remain unaltered while the dimension of the ocean basin in the x-direction is reduced to 2/3 (Fig.5.1) and the horizontal resolution doubled (Δx=20 km), as is the number of layers (6-layer). The reasons for the aforementioned changes are very simple. First, the coupled Rossby mode identified in the previous chapter had a specific wavenumber structure in both the oceanic and atmospheric response. We will try to understand in the next configuration whether the dimensions of the oceanic basin are crucial for generating the right atmospheric response or if the equilibrated atmospheric structure can be induced by a smaller ("Atlantic-like") ocean. Second, both the baroclinic instability to which Rossby waves are subject and the mean flow speed-up are dependent on the horizontal resolution of the ocean; by doubling the spatial resolution in our ocean we will be able to test the effect of resolving the second Rossby radius of deformation on the instabilities of the wave. Finally, we will explore the results of a more accurate tridimensional representation of the ocean by using a vertical resolution of six vertical modes: though mean flow speed-ups are not expected to vary significantly (Dewar and Morris, 2000), we are able to better represent the effects of mode couplings and the inverse cascade involved in the baroclinic instabilities (Barnier et al., 1991) as well as the response of higher modes to the atmospheric coupling.

Next, we give a brief description of the changes in the Q-GCM set-up. In section 3 we perform similar analyses as in Chapter 4 for the identification of the Rossby wave and the coupled wave, again at the two central latitude of $\phi = 30^o$ and $\phi = 40^o$. Then we conclude, summarising the results and comparing them with those of the previous configuration.

5.1.1 The 6-layer high-resolution set-up

In order to test the effects of higher accuracy in the tridimensional resolution of the ocean, the Q-GCM was run with a 6-layer ocean configuration at a horizontal resolution of 20 km for 200 years. In doing so, we dramatically increased the CPU time and the size of the output data arrays. However, the importance of the horizontal extent of the ocean in generating the coupled ocean-atmosphere mode was also tested. In particular, the length of the basin was reduced to 2/3 of the original configuration. The dynamics of the model is unchanged with the only difference being in the number of layers in the oceanic domain, where the QG potential vorticity equation is now simply

$$\partial_t q_i + J(q_i, \psi_i) = 0, \qquad i = 1, ..., 6. \tag{5.1}$$

An example of the two ocean basins and their relation with the overlying atmospheric channel is given in Fig.5.1. Here, the atmospheric surface temperature anomalies are contoured during the model spin up, revealing the oceanic domains beneath them, where the SST fields are pictured. Although reduced, the ocean basin is still very wide (more than 7500 km) and with the new set-up we are still able to study the propagation of Rossby waves under the atmospheric effects over long distances. The new oceanic part of the model is schematised by the dashed black box in the right panel of Fig.5.2 together with the previous Pacific-like ocean (left

Parameters	Value	Description
Z_i	6	N^o of layers
Δx	20 [km]	Horizontal grid spacing
(X, Y)	(7680,4800) [km]	Domain size
H_i	(300, 300, 500, 500, 1000, 1400) [m]	Mean layer thicknesses
T_i	(278, 268, 258, 248, 248, 248) [K]	Layer's potential temperature
g'_i	(25, 20, 15, 6.3, 3.1)$\times 10^{-3}$ [ms^{-2}]	Reduced gravity
a_i	(55.0, 38.1, 25.5, 15.1, 8.5) [km]	Rossby radii at 30^o
a_i	(44.5, 29.5, 17.4, 12.5, 12.1) [km]	Rossby radii at 40^o

Table 5.1: *As Table 3.1, but only for the parameters that differ from the 3-layer configuration.*

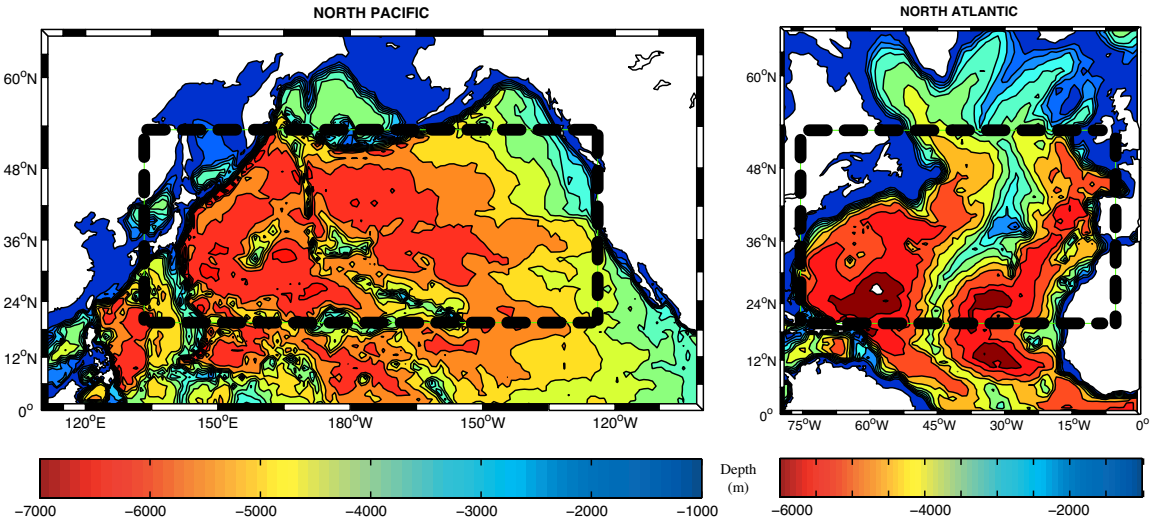

Figure 5.2: *North Pacific and North Atlantic topography, together with the ocean Q-GCM represented by the heavy dashed box in the two different configurations.*

panel) for comparison. It is evident how both configurations relate well with the realistic dimensions of the two oceans and how the addition of topography would be of particular interest in the case of the Atlantic because of the presence of the steep mid-Atlantic ridge there.

The values of the parameters that differ from the previous simulations are shown on Table5.1; the layer depths and density jumps were chosen in order to result in similar Rossby radii as in the 3-layer experiments. In fact, since the basin dimensions have changed, there is no need to reproduce the exact deformation radii, but the aim is to keep the background conditions as similar as possible.

The density profiles for the two cases and the 6 vertical modes are shown in Fig.5.3. The vertical density structure is very similar in both configurations while, inevitably, the vertical normal modes differ (not shown). In the right panels of Fig.5.3 we plot the vertical normal modes for the 6-layer case, where mode-0 is the barotropic mode. Higher modes tend to be more sensitive to vertical resolution but at the same time they are less energetic and less important for both mean flow interactions and atmospheric couplings (Barnier et al., 1991), making our vertical level depths a good approximation for our purposes.

With a higher resolution, a better identification of Rossby wave instabilities is possible thus making the comparisons with the instability theory of LaCasce and Pedlosky (2004) more significant (was the weak instability observed in the previous chapter up to a certain degree an artefact of the poor resolution?). Also, the choice of the new dimensions for the ocean will shed light on the possibility of developing such Rossby coupled modes in smaller basins such as the Atlantic ocean and on whether the horizontal extension of the ocean actively coupled to the atmosphere is

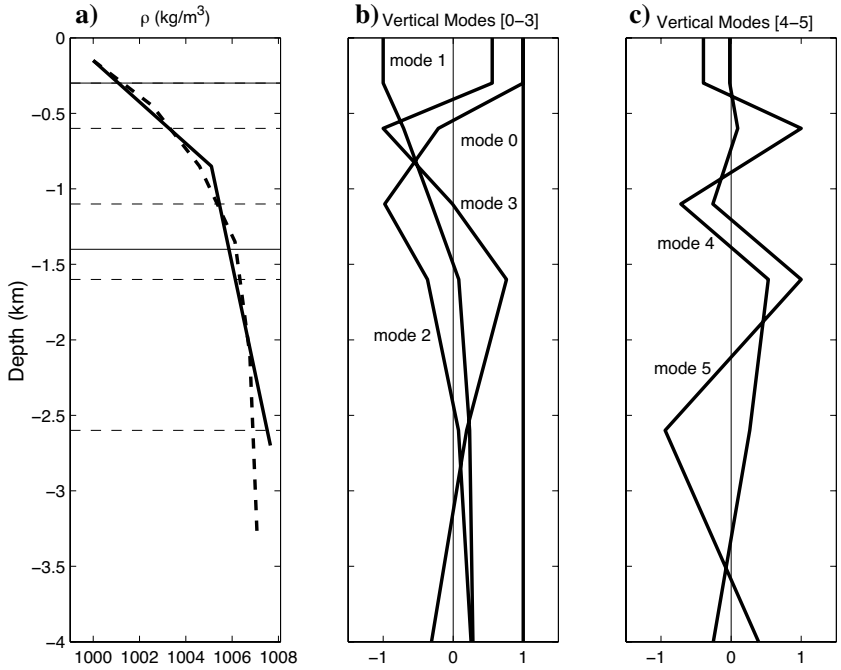

Figure 5.3: *a) The density profiles for the 3-layer (solid line) and the 6-layer (dashed line) ocean configurations. The horizontal lines denote the layers depths. b)-c) The 6 vertical modes for the 6-layer stratification. Mode 0 is the barotropic one.*

hence of crucial importance.

Dewar and Morris (2000) studied Rossby wave-mean flow interactions in a QG model forced by the time-dependent subtropical gyre Ekman pumping, using 10 km horizontal resolution in 2-, 3-, and 6-layer experiments. They suggested that a 3-layer configuration is able to capture all the essential wave-mean flow interactions. In the following sections we will test if this is still true under an active atmosphere and whether other Rossby couple modes can appear. For instance, high baroclinic modes have been shown to play a catalytic role in energy transfers and therefore in the eddy-driven circulation (Barnier et al., 1991) and this effect could possibly have an impact in any ocean-atmosphere mode coupling.

5.2 Results

As for the previous configuration, the Q-GCM is run for 200 years at the central latitudes of ϕ=30^o and ϕ=40^o for the Atlantic-like ocean. In the 6-layer resolution the thermocline displacements will be given by the evolution of the third interface height, located at a depth of 1100 m.

The identification of the Rossby wave activity is again carried out by inspection of Hovmöller diagrams and the use of FFT techniques. The westward-filtered (but

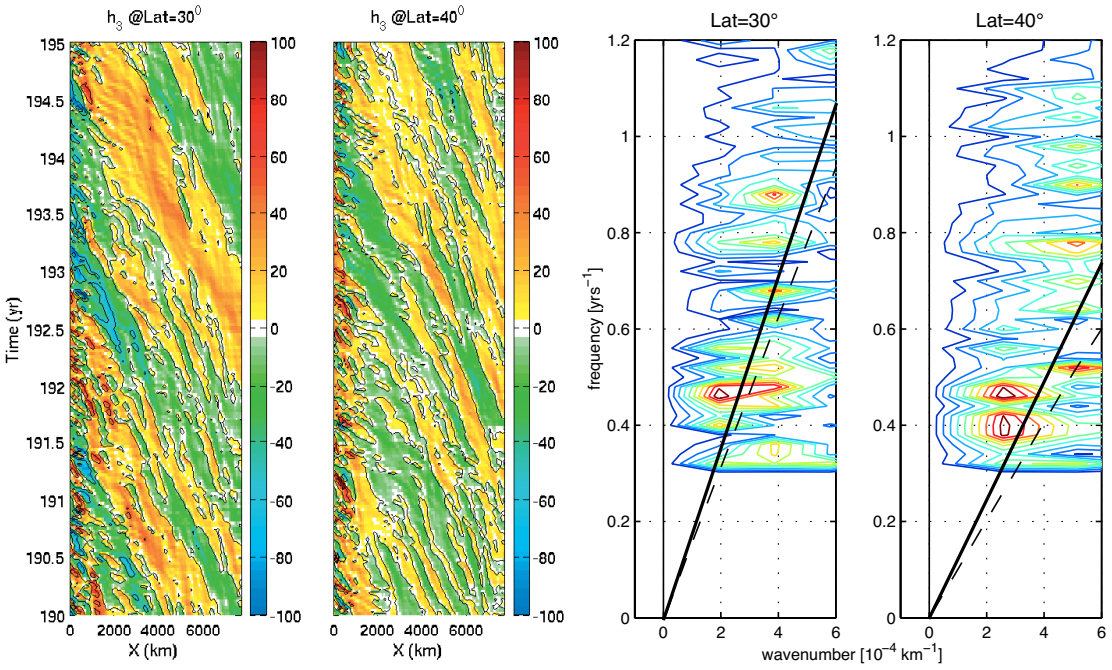

Figure 5.4: *Left panels: Hovmöller plots of the third interface height (OCH3) for $\phi = 30^o$ and 40^o. Different periods of propagation are present and waves are consistent throughout the whole basin. Right panels: FFT analyses of OCH3 at the two central latitudes. Several peaks are observed to fall into the unperturbed (dashed lines) or perturbed (solid lines) solutions. Quasi-annual peaks in both cases are much faster than predicted, while only at 40^o a biannual peak is observed to possess a further speed-up.*

unfiltered in the frequency domain) Hovmöller plots of the third interface height (OCH3) are for the period 190-195 years and the FFT analyses were carried out applying a band pass filter between 6 months and 3 years after inspection of the unfiltered results. The results for both central latitudes are plotted in Fig.5.4.

Two main characteristics arise from the Hovmöller diagrams. First, Rossby waves do not seem to break and faster waves (either barotropic or baroclinic) are not generated from an original "mother wave". Second, there is a much larger variability in wave periods at both latitudes. Both results seem to agree with middle-latitude observations in basins of these dimensions (Cipollini, pers. comm.). In fact, Rossby waves are not observed to change their characteristics abruptly and generate much faster waves. Also, different periods of propagation are generally observed and is common to lose track of a particular crest or trough in the middle of the basin to then recover the signal (of similar frequency) in the western part of the basin. All these features are visible in the left panels of Fig.5.4 for both central latitudes.

The FFT analyses indeed confirm the results previously observed (right panels

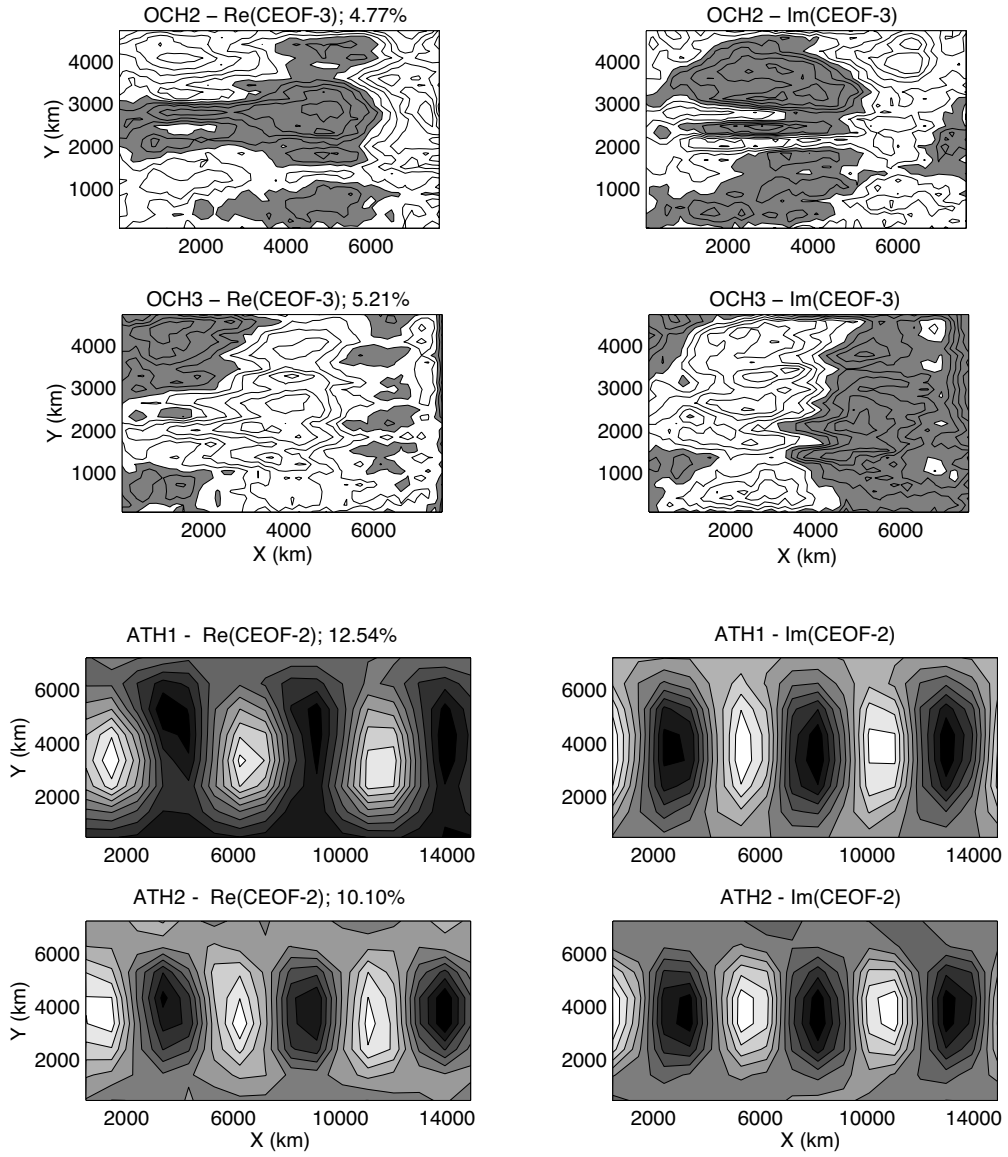

Figure 5.5: *Unfiltered CEOF of the second and third ocean interface heights (OCH2, OCH3) and of the first and second atmospheric interface heights (ATH2, ATH3). The third CEOF mode in the ocean is characterised by a baroclinic Rossby wave and the second CEOF mode in the atmosphere corresponds to westward-propagating wave response.*

of Fig.5.4). Here, we did not divide the basin into a western and eastern side as done in the previous chapter because there is no evidence of significantly different peaks away from the boundaries in the two parts of the basins. For the two latitudes considered, two main peaks of quasi-annual and biannual period are present. Peaks of different periods are observed to either fall into the unperturbed (dashed line) or the perturbed[1] (solid line) theory for the two cases considered, suggesting a variety

[1]As in Chapter 4, we refer here to "perturbed solution" to the dispersion relation computed with the inclusion of a zonal mean flow. For computations of perturbed solutions see Appendix B.

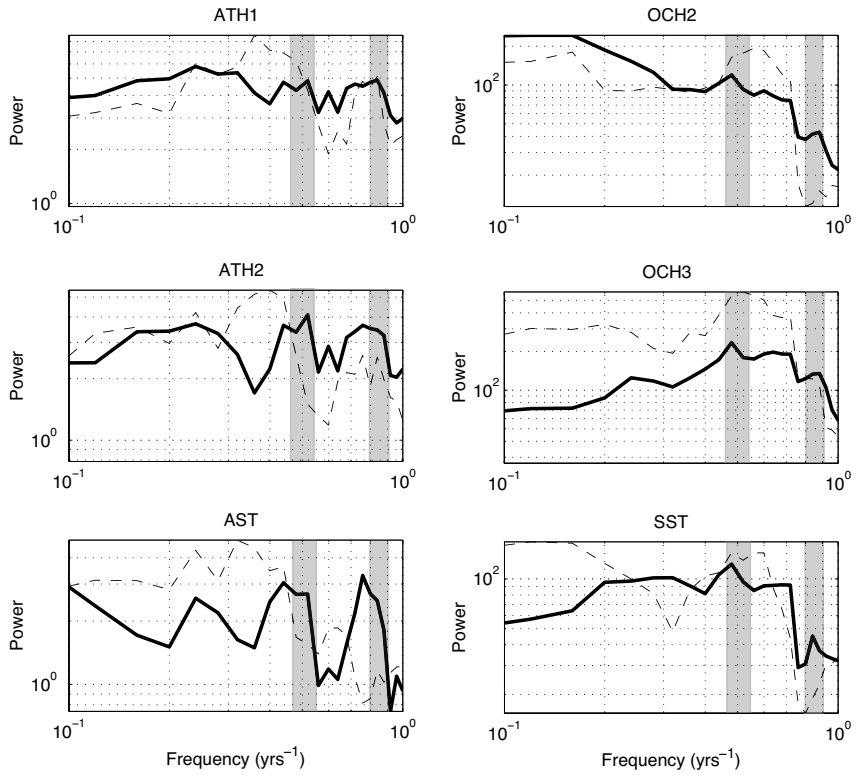

Figure 5.6: *Unfiltered spectra of the CEOF modes plotted in Fig.5.5 and of the same modes for SST and AST. Dashed areas highlights the periods of the two main peaks (P ∼2 and 1.2 yr).*

of different responses. The quasi-annual and biannual peaks are both faster than the unperturbed theory (with a general speed-up of about 1.6-1.7) but only in the case of ϕ=40^o the biannual peak has a significantly greater frequency than the predicted by the perturbed solution. Also, speed-ups of the coupled waves are observed to be greater at ϕ=40^o as found in the Pacific-like configuration of Chapter 4.

The spatial structures of the Rossby wave corresponding to the main peaks previously identified are extracted from a CEOF analysis. An example for ϕ=40^o is given in Fig.5.5, where a baroclinic Rossby wave corresponding to the third CEOF mode of OCH2 and OCH3 is showing the quasi-annual (P ∼1.2 yr) and biannual (P ∼2 yr) peaks in its spectrum (Fig.5.6). The westward propagating atmospheric response is present at both central latitudes and is given by the second CEOF mode of the atmospheric interface heights (bottom panels of Fig.5.5). Moreover, the spectra in the equilibrated atmospheric response match once again the peaks of the oceanic Rossby wave (Fig.5.6). In the case of ϕ=30^o only the peak at P ∼1.2 yr appears in both the oceanic and atmospheric CEOFs, showing that the biannual wave in this case does not trigger a coupled response and its phase velocity stays in the range predicted by the perturbed solution.

5.2.1 The coupled Rossby waves

We performed a CCA analysis on the data sets obtained from the two runs similarly to the Pacific-like configuration. The results are qualitatively similar at both latitudes: for ϕ=30^o a coupled Rossby wave with the characteristics described in Chapter 4 is found for the main peak of quasi-annual period, while at ϕ=40^o two coupled modes are captured by the CCA, one of quasi-annual period and one of biannual period. The spatial relationships between all the oceanic and atmospheric variables in the coupled modes of the Atlantic-like experiments are again the ones given by Goodman and Marshall (1999) model, as described in detail in the previous chapter.

We will focus from now on on the existence of the two separate coupled modes present at ϕ=40^o with biannual and quasi-annual period. We did not find a baroclinic atmospheric response, leading to a possible damped mode through temperature anomalies, as we did in the Pacific-like simulations. Here, the only oceanic and atmospheric temperature anomaly CCPs with propagating-like structures possess energy peaks at the Rossby wave periods as shown in Fig.5.7 and will be associated with an equivalent barotropic response in the atmospheric column. However, as previously mentioned, we found two separate ocean-atmosphere modes carrying the characteristics of the growing mode described by Goodman and Marshall (1999), both sharing the quasi-annual and the biannual peak but preferentiating one of them in each case.

In Fig.5.8 the third CCPs mode between SST and the atmospheric pressure anomalies are plotted together with their respective spectra. The phase relationship are the ones described in the positive feedback of Goodman and Marshall (1999), i.e. positive SST anomalies lying under positive pressure anomalies and vice-versa. The atmospheric response is equilibrated and, although we modified the extension of the ocean basin, the coupled response has the same wavenumber. The spectra at the bottom of Fig.5.8 show the common peaks at both Rossby wave periods but that of the biannual period seems to be the strongest.

The second coupled mode between SST and ATPA, CCP-4, is shown in Fig.5.9. It has the same characteristics as the previous one, and therefore satisfies the spatial relationships of the positive ocean-atmosphere feedback with weaker correlation coefficients. The spectra of CCP-4, although showing a weak common peak at P $\sim$2 yr, are dominated by the quasi-annual period. Thus, we are in presence of two coupled baroclinic Rossby waves of different periods, generated by the same mechanisms and identified by two separate coupled ocean-atmosphere modes that retain the signature of the propagation of both waves but are mainly defined by one

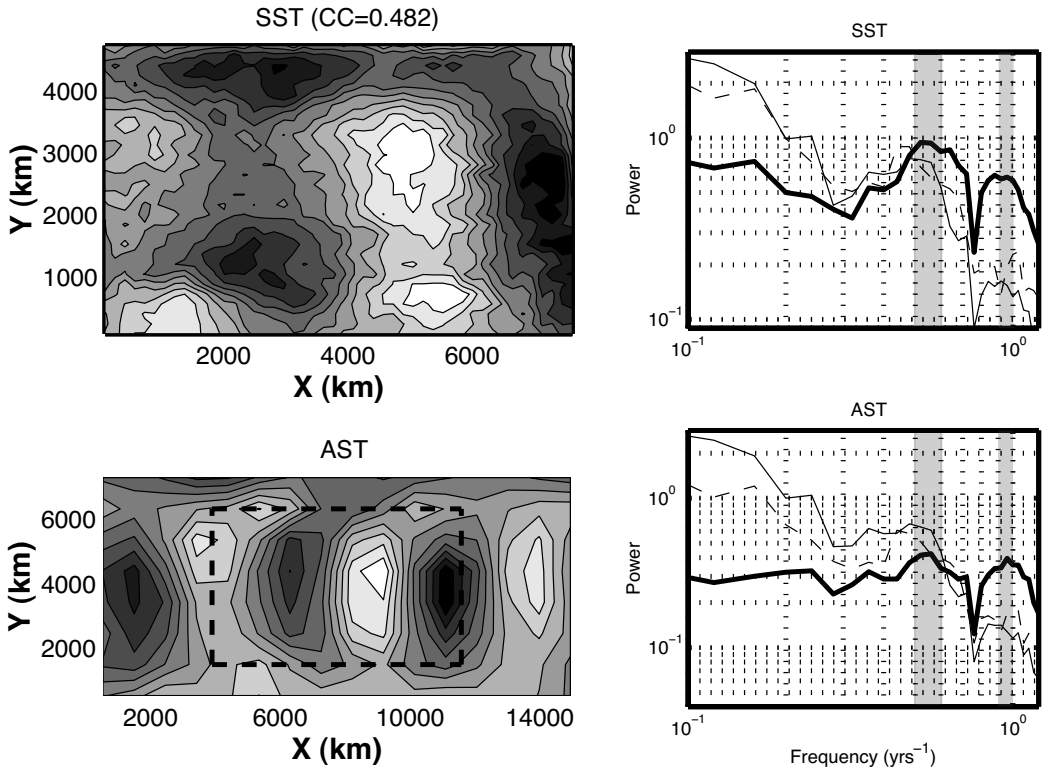

Figure 5.7: *Unfiltered Canonical Correlation Analysis between SST and AST. Shown is the third Canonical Correlation Pattern (CCP-3) mode with correlation coefficient 0.482. The dashed box in the atmospheric panel represent the oceanic domain sitting underneath. Negative weights are shaded. On the right panels, in bold lines, the spectra of the temporal coefficients showing coupled peaks at the Rossby wave period (P ∼2 and 1.2 yr) for CCP-3; other lines correspond to the spectra of CCP-1 and CCP-2.*

of them. The CCA analyses gave conclusive results for all variables in the case of the two coupled modes, showing the presence of the mechanisms described schematically in Fig.4.14, but the canonical patterns and associated spectra are not shown since they have been described in detail in Chapter 4.

The correlation analyses on the data set at ϕ=30^o showed the existence of one coupled mode, with the quasi-annual period of the Rossby wave. In general, spatial patterns have been found to be less coherent for the Atlantic-like ocean than for the Pacific-like experiment and correlation coefficients in the CCA analyses weaker. This is due to many factors. First the ocean is considerably shorter and the coupled wave does not have as much time as before to propagate. Then, the existence of different periods in the propagation of Rossby waves in the ocean generate not a single atmospheric response but two - and possibly more - coupled modes partitioning different levels of correlation between the ocean and atmosphere. Last, the use of a 6-layer ocean model, although giving us insight into the response of the wave-

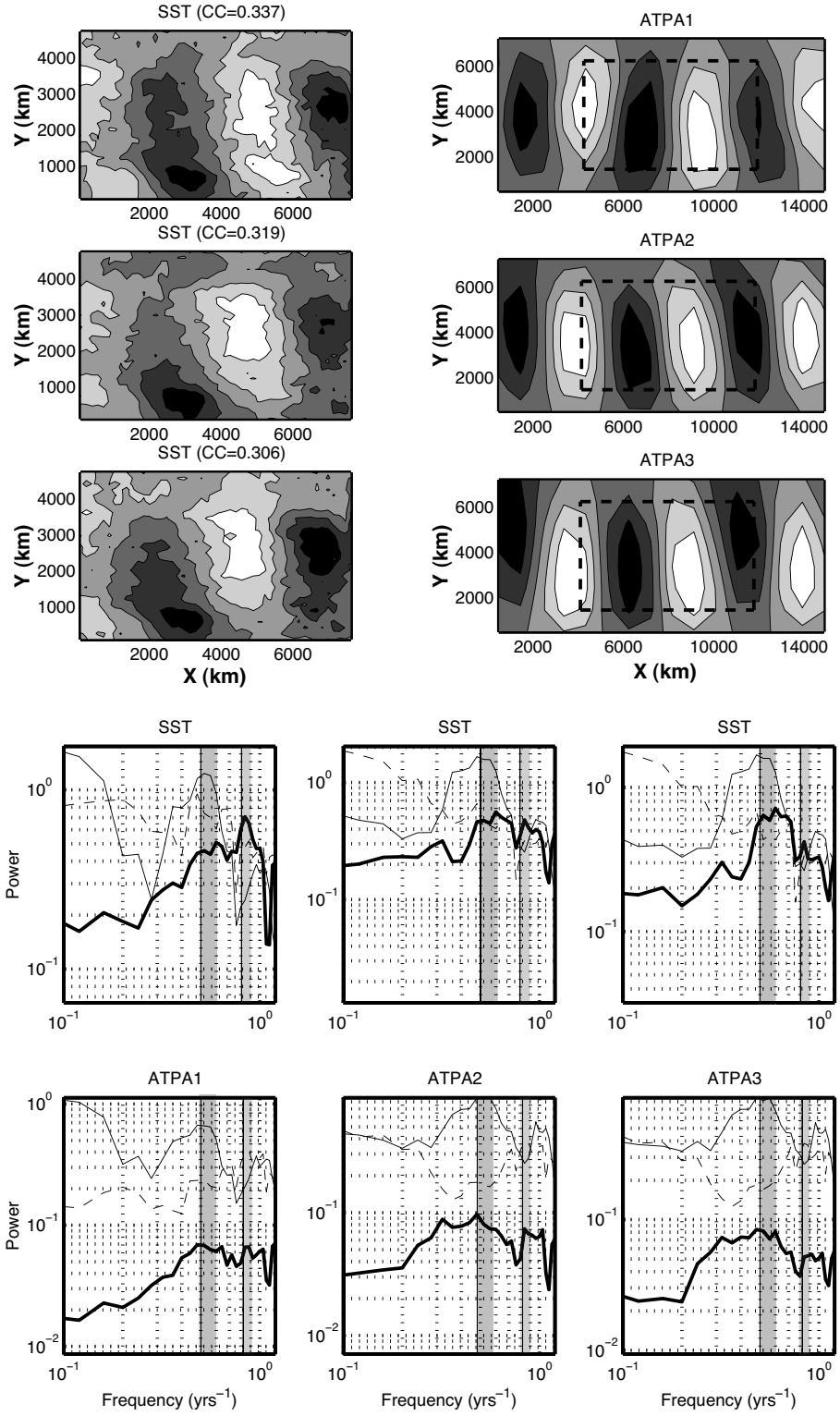

Figure 5.8: *CCP-3 of the SST-ATPA unfiltered CCA analysis. SSTs are in phase with atmospheric pressure anomalies and these have an equivalent barotropic structure. In the bottom panels, the corresponding spectra in bold lines. The common peaks at P ∼2 and 1.2 yr (shaded areas) are both present but the biannual period seems predominant. Thin solid line is for CCP-1 and the dotted line for CCP-2.*

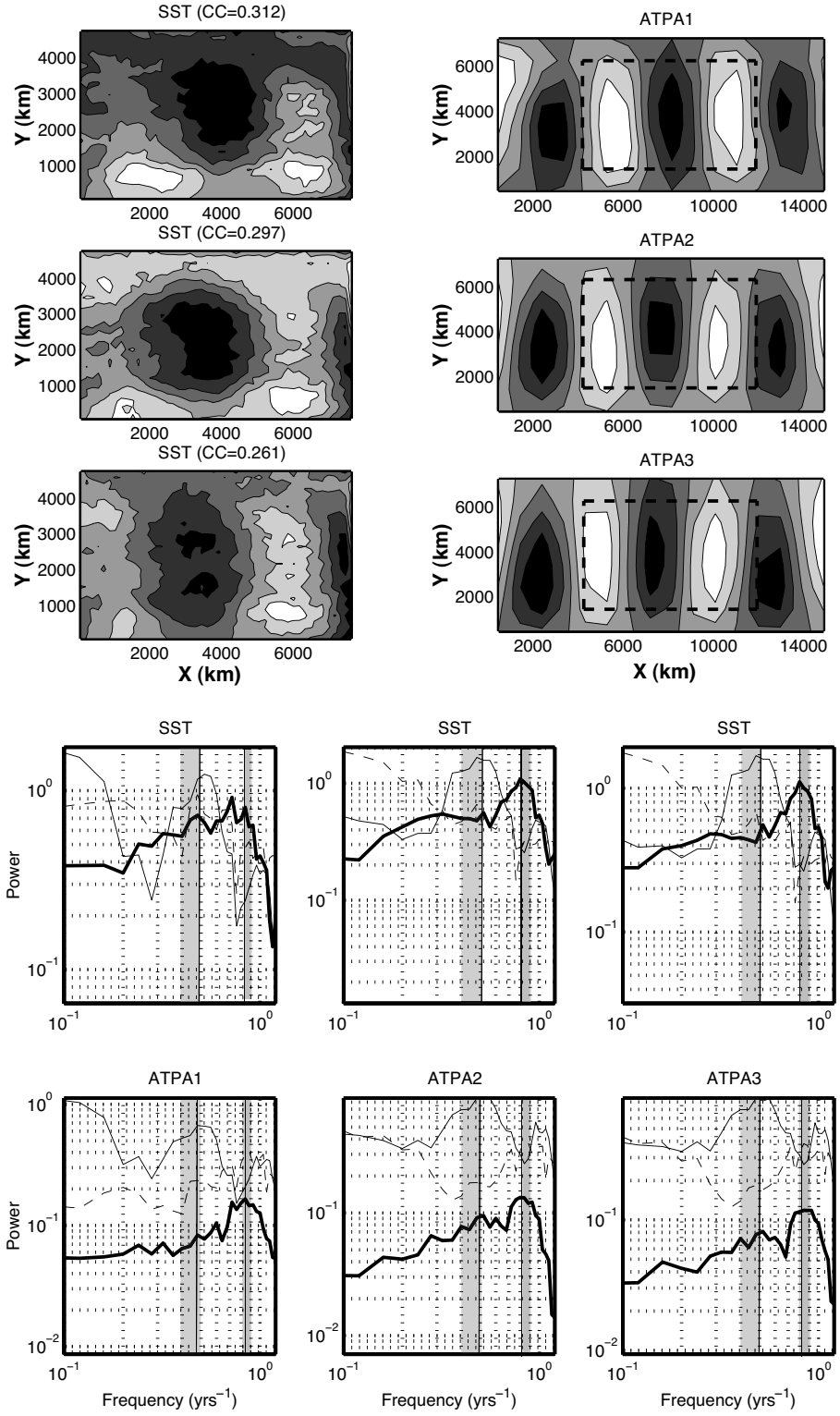

Figure 5.9: *As in Fig.5.8 but for the CCP-4 of the SST-ATPA analysis. The correlation coefficients are slightly weaker but the overall patterns are similar. The spectra (bold lines) share again the common Rossby wave periods but in this case the interannual peak is the dominant. Thin solid line is for CCP-1 and the dotted line for CCP-2.*

mean flow and ocean-atmosphere interactions in a tridimensional consistent ocean configuration, introduced more degrees of freedom in the multivariate analyses.

5.3 Conclusions

In this chapter a different experiment was carried out in which the strength of the coupled Rossby wave was tested. An Atlantic-like ocean underneath the same atmospheric model as used in Chapter 4 was set up. Both horizontal and vertical resolution have been doubled, resulting in an horizontal grid space of 20 km and 6 vertical levels. Rossby waves were characterised in the ocean at the two central latitudes of ϕ=30^o and ϕ=40^o and the coupled Rossby modes identified with the help of the statistical eigentechniques introduced in the previous chapter and formulated in Appendix A.

First we noted how Rossby waves, despite the high tridimensional resolution, were not revealing the instability mechanism proposed by LaCasce and Pedlosky (2004) in a smaller basin. Only at ϕ=40^o do waves seem to break into faster waves but only very close to the western boundary, managing to travel more than double the distance predicted by LaCasce and Pedlosky (2004) at those latitudes. The frequency-wavenumber analyses did not show any new energy peak generated at the western side of the domain contrary to the Pacific-like experiments.

The ocean was rich in waves of different periods, some of them characterised by the unperturbed linear dispersion relation, others by the perturbed dispersion relation computed with the addition of the effect of the mean zonal flow, and finally waves of quasi-annual and biannual period were seen to propagate at a higher phase speed than that predicted by any dispersion relation at both central latitudes. In particular, at ϕ=40^o we identified both quasi-annual and biannual waves to be coupled with the atmosphere following the mechanism proposed by Goodman and Marshall (1999) and described in the previous chapter. At ϕ=30^o, only the quasi-annual wave presented an additional speed up and a coupling with the equilibrated atmosphere, while the biannual period wave followed the perturbed dispersion relation.

Making use of the statistical eigentechniques applied in the former experiments, we described the spatial relationships and strength of correlation between the baroclinic Rossby waves and the equivalent barotropic atmospheric response through thermal coupling. Different coupled modes carrying the periods of the oceanic Rossby waves involved in the coupling are present, each mode identifying one wave in particular.

As in the Pacific-like configuration, it is argued for the Atlantic-like experiments

that the ocean-atmosphere coupling is responsible for the additional speed up observed in some of the Rossby waves present in the basin. Therefore the modifications applied to the model were not crucial for the existence of the coupled feedback. An ocean of similar dimension to the Atlantic, and thus much smaller than a Pacific ocean, is capable of developing such coupled modes and generating faster Rossby waves. Also, the coupling is involved in the stability of the waves, as they are observed to propagate coherently to the western boundary with small modifications, contrary to LaCasce and Pedlosky (2004) predictions.

The tridimensional consistency of the resolution in the Atlantic-like ocean, able to better capture the wave-mean flow interaction and represent the higher modes role in the ocean dynamics, was probably responsible for introducing more variety in the wave propagation and confirmed the results obtained with a coarser horizontal and vertical resolution. However, the increased degrees of freedom in the 6 layer experiments made the identification of spatial patterns and correlation between variables in the statistical analysis poorer, without introducing new information or modifying the coupling mechanism. Thus we conclude that, as for the propagation of forced Rossby waves in a mean flow (Dewar and Morris, 2000), a high horizontal resolution 3-layer experiment is the most suitable set up for determining coupled Rossby waves in the model.

Chapter 6

Summary and future projects

6.1 Summary

In the last years, the basic characteristics and properties of Rossby waves in a realistic ocean have been the interest of many authors. Especially, the phase speed and stability of the waves have gained a particular attention. So far, the problem has been addressed in two ways: analytical and modelling efforts have concentrated on ocean-only studies or highly idealised coupled models, while fully non linear ocean-atmosphere interaction studies have been the focus of observational and data analyses. Modelling studies on the propagation of Rossby waves in eddy-resolving coupled models are scarce in the literature and the subject of this thesis is an attempt to partially fill this gap.

We begun by analysing simple couplings with the atmosphere in Chapter 2. In order to gain insight into the response of a wave under different boundary conditions, simple thermodynamical couplings were formulated, ranging from a simple heat flux to an atmospheric energy balance model. We found that few modifications occurred on the structure and propagation speed of the first modes for all the cases. Furthermore, we identified a growing mode in the case where the energy balance model is present, which has no physical energy source. It was argued in Chapter 2 that the simplified atmosphere was the responsible for the existence of such unstable modes; in fact, when we added physical mechanisms to the energy balance model the unstable mode responded by damping out. The decadal period and growth rate of the growing mode might mislead climate modellers using simplified atmospheres coupled to an ocean model, and the low order in the vertical might highlight this mode and be mistakenly believed to be a Rossby mode responding to the atmospheric forcing.

The poor damping of the first Rossby wave modes by thermodynamical processes

encouraged us to look for positive effects due to the atmospheric dynamics, as also suggested in previous theoretical and simple coupled models. We employed a fully non linear, fully coupled ocean-atmosphere model with quasi-geostrophic dynamics (Hogg et al., 2003b). The model was recently developed and has the ability of performing fast computation of coupled runs, resolving the turbulent characteristics of the ocean and variability of the climate system (Hogg et al., 2005). A review of the model formulation and the set-up utilised in this thesis is given in Chapter 3.

In Chapter 4 we looked for the Rossby wave response in a coupled ocean-atmosphere system at the two central latitudes of 30^o and 40^o. The identification of the Rossby wave properties in the model showed fast waves, travelling faster than the speed computed with the inclusion of the zonal mean flow, capable of propagating very long distances against dissipation and instability processes. The phase speed of the main Rossby waves at both latitudes were approximately double the unperturbed speed, while the speed-up by the mean shear accounted for only 20% of the discrepancies. The waves were observed to break into faster barotropic waves, with increasing effect with latitude, with the instability taking place at 3 to 4 times the distance predicted by LaCasce and Pedlosky (2004). Since topography is absent from the model and the mean flow effects have been already taken into account, the only mechanism that could be responsible to significantly modifying the planetary wave propagation was the atmospheric forcing and coupling.

We then looked for the role of the atmosphere in the wave response. With the help of statistical eigenanalysis, we identified a clear coupled Rossby wave mode of the kind proposed by Goodman and Marshall (1999). The coupled mechanism, extensively studied in Goodman (2001), works as follows: the westward propagation of the Rossby wave produces SST anomalies through both advection and entrainment - although we proved the latter to be critical for the development of the coupled mode - exciting an equivalent barotropic stationary atmospheric wave response. The atmospheric wind stress feeds back to the ocean through Ekman pumping, enhancing the ocean anomalies. The stationary atmospheric wave then moves westward, phase-locked with the oceanic Rossby wave, resulting in a coupled Rossby mode with the period of the oceanic component. The coupling permits the Rossby wave to resist longer distances against instability processes and adds an extra speed up other than the baroclinic mean flow. In fact, when the model was simply forced by the atmosphere, Rossby waves were observed to slow down and break sooner than when coupling effects are present.

Unfortunately, the statistical techniques did not allow for an inspection of the stability of the coupled mode. Is this an unstable coupled mode? it is more probable that we are looking at a decaying mode. The original Goodman and Marshall

(1999) coupled mode was in fact found to be a growing mode, but when several simplifications were addressed and notably meridional boundaries added in the ocean basin, the coupled mode became damped because of the western boundary effect on the Rossby wave.

The model used in Chapter 4 was set up for a "Pacific-like" ocean of coarse resolution in both the horizontal and vertical. These characteristics of the model configuration, possibly influencing both the coupled mode and the oceanic Rossby waves, were tested in Chapter 5. In this chapter, an "Atlantic-like" ocean with tridimensional high resolution was employed for the ocean component of the model, while the atmospheric channel remained unmodified. The high resolution resulted in a broad range of Rossby waves of different periods in the runs. Some of these were coupled to the atmosphere in the same way as in the previous configuration, and manifested the extra speed up together with a coherent propagation throughout the basin. The results demonstrated the ability of generating such coupled modes in smaller basins with similar dimensions to the Atlantic ocean; moreover, while the increased horizontal resolution generated a better representation of the Rossby waves propagation and of the wave-mean flow effects, the vertical consistency in the resolution added degrees of freedom to the system resulting only in a reduced correlation between the oceanic and atmospheric variables.

We think this study was successful in many ways, although in depth analyses of the atmospheric effects on the Rossby wave propagation with the help of simpler semi-analytical models are still needed. First of all, the Goodman and Marshall (1999) coupled mechanism was identified, and confirmed, in a non linear coupled climate model, being this the primary future project planned by Goodman (2001). Secondly, we emphasised the role of the atmosphere on the Rossby wave phase speed discrepancy, which has been tackled so far in simple idealised coupled models and mainly in observations (several studies by W.B. White, for instance). Even though we did not give an explanation for the atmospheric-generated speed up (which will be the scope of future studies), we clearly showed its existence under different configurations, where no other factors might be involved in the process. We also observed the instability mechanism of LaCasce and Pedlosky (2004) take place as well as the different repercussion on the Rossby wave propagation when these are coupled or not.

As expected, the modelling work presented here gives rise to many questions, which can be tackled theoretically, with the use of a more complete coupled general circulation model and by looking at observations. We try to suggest some of these projects in the next section.

6.2 Future work

Several different projects could be suggested in the light of the results presented in this thesis. The most pressing studies are the confirmation and understanding of the effects of the atmospheric coupling on the Rossby wave phase speed and stability.

A detailed study of the baroclinic instability processes occurring in the model, and its relation with the continuously stratified theory, should be addressed, in both coupled and forced configurations. This would enable us to thoroughly compare the idealised theory and results proposed by LaCasce and Pedlosky (2004) with our coupled solutions, giving estimates for the atmospheric input. The study of the enhanced phase speed of the oceanic Rossby wave needs modelling work at different latitudes. In this case, running the model in a wide range of central latitudes, with both the coupled and forced configuration, would present us with the familiar latitudinal dependence of the propagation speed, resulting in a wide spectrum of phase speeds for the coupled and forced waves. Both lines of research should be implemented with the use of a different, and more complete, coupled general circulation model (CGCM). In particular, a CGCM would allow us to directly compare the results with observations of both the phase speeds and stability of the waves and test the numerous hypotheses brought forward by W.B. White in his observational studies.

The coupled Rossby mode identified in our model was clearly of the type proposed by Goodman and Marshall (1999). However, as pointed out in Chapter 4, the tools employed here for its detection could not give information on whether the couple mode is unstable or damped. To this end, we are carrying out a linear stability analysis on our model and a simplified version of the Q-GCM equations have been developed for analytical purposes. The eigenmodes of the coupled system will be compared to the previous results and tests on the parameter dependence and coupling strength will be performed. The system is cast into $\partial_t \phi = \mathsf{M}\phi$, where ϕ is the state vector consisting of the unknowns (ψ_{a1},ψ_{a2},ψ_{a3},ψ_{o1},ψ_{o2},ψ_{o3},T_a,T_o) and M is the coupled tendency matrix. A linear stability analysis is pursued and numerically solved with the ARPACK package (Lehoucq et al., 1998). Solutions of the form $\phi = e^{\sigma t}\hat{\phi}(x, y)$ are considered, where ϕ is any of the oceanic and atmospheric variables and $\sigma = (\sigma_r + i\sigma_i)$. The coupled modes are given by the eigenmodes of the linear operator M; the real part of the growth rate σ_r will determine whether perturbations will grow or decay with time, and thus whether the stationary flow is stable or unstable respect to these perturbations (Katsman, 2001). The eigenmodes are sorted by the most positive real part and the system is unstable when $\sigma_r > 0$. A complex conjugate eigenvector is associated with each pair of complex conjugate eigenvalues and the

spatial patterns of the modes are given by the real part of the eigenvectors and the time periodic pattern evolution of the unstable/stable solutions during a cycle by $\phi(x, y, t) = [\phi_r cos(\sigma_i t) - \phi_i sin(\sigma_i t)]e^{\sigma_r t}$ (Simonnet and Dijkstra, 2002), where $\phi = (\phi_r + i\phi_i)$ and the period of the oscillation is given by $P = 2\pi/\sigma_i$ (Dijkstra and Katsman, 1997). In summary, this technique will permit us to compare the coupled mode behaviour with the one previously identified, to understand what kind of couple mode is been generated (stable/unstable) and under what conditions, and finally to test its dependence on different background mean flows. A useful technique to identify ocean-atmosphere patterns could also be the computation of the neutral vectors in the system as suggested by different authors (Navarra, 1993; Marshall and Molteni, 1993; Goodman and Marshall, 2002, 2003) and this might be an extension of the linear stability study.

As explained in Chapter 3, the oceanic component of the Q-GCM might be set up for a channel configuration. This would have two advantages. First, to study the coupled Rossby waves in a meridionally unbounded basin and second, to reproduce coupled ocean-atmosphere interaction in the Antarctic circumpolar belt and look for signals related to the so called Antarctic Circumpolar Wave (ACW, White and Peterson, 1996).

There are many other possible issues to address, for instance, the atmospheric response to SST forcing, which is still subject to controversy (for a review see Ferreira and Frankignoul, 2005). This would involve decoupling the Q-GCM and let the atmospheric component be forced by SST anomalies to see whether we can excite an equivalent barotropic atmospheric response similar to the one observed in the coupled runs. The model also allows the introduction of variable topography in the ocean: in that case the idealised topographic effects on the propagation of Rossby waves could be addressed.

Finally, in the context of oceanic Rossby wave propagation, we feel that more effort is needed in the analysis of realistic models and that the role of atmospheric influences cannot be ignored any longer.

Appendix A

Statistical Eigentechniques

In this appendix we give a brief overview of the statistical eigentechniques used in the previous chapters. More detailed and accurate derivations and explanations, as applied in the case of climate analysis, are given by Preisendorfer and Mobley (1988), von Storch and Navarra (1999), von Storch and Zwiers (2001) and Venegas (2001), to cite only a few.

A.1 Empirical Orthogonal Functions

When dealing with a large data set we are obliged to find a way of compressing the information and we want to be able to identify its main features and variability in both space and time.

The most common multivariate analyses applied in these cases are Empirical Orthogonal Functions (EOFs) as they provide a succinct information of the dominant spatial and temporal variability of the original data set in terms of uncorrelated modes, each representing a fraction of the variance explained.

Having a time series of data $F(t)$, we need to form the anomalies by de-meaning the field and normalise it to variance one. Then, once our matrix $\mathbf{F}$ containing time series at each location is ready, we construct the spatial covariance matrix as

$$\mathbf{R_{FF}} = \mathbf{F} * \mathbf{F}^{\dagger}, \tag{A.1}$$

where $\mathbf{F}^{\dagger}$ denotes the transpose of $\mathbf{F}$. In fact, since $\mathbf{F}$ has been previously normalised by its standard deviation, $\mathbf{R_{FF}}$ is defined as a correlation matrix.

At this point we need to solve the eigenproblem

$$\mathbf{R_{FF}} * \mathbf{E} = \mathbf{E} * \mathbf{\Lambda}. \tag{A.2}$$

The decomposition leads to two matrices: matrix $\mathbf{E}$ is the squared eigenvectors matrix, whose k columns represent the modes. The eigenvectors are spatially uncorrelated, that is, orthogonal to one another and represent the spatial EOF pattern

of each mode k. The diagonal matrix $\mathbf{\Lambda}$ contains the associated k non-negative eigenvalues λ_k, ordered in decreasing order.

The temporal evolution of a particular mode is given by its principal components (PCs), resulting from the projection of the original data onto the eigenvector E^k, i.e.

$$\mathbf{P} = \mathbf{E}^{\dagger} * \mathbf{F}. \tag{A.3}$$

Each EOF mode k represents a portion of the variability present in the original data and this is given by its eigenvalue λ_k, which can be expressed in term of a percentage of the variance of the total field F.

Finally, the original field $F(t)$ can be reconstructed. Generally only the first j modes ($j < k$) are sufficient in explaining the inner variability so that a truncation of $F(t)$ to a compressed field $\tilde{F}(t)$, that explain most of the variance, is used to recover the initial field. This is achieved simply with the sum of the j EOF patterns multiplied by their PCs:

$$\tilde{F}(t) = \sum_{k=1}^{j} E^k A^k(t) \tag{A.4}$$

A.2 Complex Empirical Orthogonal Functions

Traditional EOF analysis can only detect standing oscillations. However, two consecutive modes can vary coherently and be in quadrature (90 degrees out of phase), giving a hint of the existence of a propagating feature in space. In this case, it is useful to turn to Complex (or Hilbert) Empirical Orthogonal Functions (CEOFs) analysis.

Here, we artificially complexify the original field $F(t)$ by adding its Hilbert transform $\hat{F}(t)$, namely:

$$\phi(t) = F(t) + i\hat{F}(t). \tag{A.5}$$

The Hilbert transform of a vector field is also called its "quadrature function", as it is identical to the original time series except for a $\pi/2$ phase-shift.

The complexified field is de-meaned and normalised as for standard EOFs and a new matrix $\mathbf{F}$ is built. As before, we compute the complex correlation matrix

$$\mathbf{R_{FF}} = \mathbf{F} * \mathbf{F}^*, \tag{A.6}$$

where the asterisk denotes complex conjugation. The eigenproblem to solve is once again

$$\mathbf{R_{FF}} * \mathbf{E} = \mathbf{E} * \mathbf{\Lambda}. \tag{A.7}$$

The complex eigenvectors E^k can be expressed in term of a spatial amplitude B^k and a spatial phase Θ^k:

$$E^k = B^k e^{i\Theta^k}. \tag{A.8}$$

The principal components are constructed by projecting the spatial CEOFs onto the original data set; the resulting time series $A^k(t)$ are also complex and consist of a temporal amplitude $C^k(t)$ and a temporal phase $\Psi^k(t)$:

$$A^k(t) = C^k(t) e^{i\Psi^k(t)}. \tag{A.9}$$

The four measures (spatial amplitude, spatial phase, temporal amplitude and temporal phase) give a complete characterisation of any propagating feature and periodicity in the original field.

The spatial amplitude of each eigenmode describes its spatial distribution of variability and has the same interpretation of an EOF pattern, it is defined as:

$$B^k = (E^{k*} E^k)^{1/2}. \tag{A.10}$$

The spatial phase shows the relative phase of a fluctuation in a given mode, varying continuously from 0° to 360°:

$$\Theta^k = \arctan\left(\frac{\Im\{\mathrm{E^k}\}}{\Re\{\mathrm{E^k}\}}\right). \tag{A.11}$$

The temporal variability in magnitude of a mode, with the same interpretation of the PCs in an EOF analysis, is provided by the temporal amplitudes

$$C^k(t) = (A^{k*}(t) A^k(t))^{1/2}. \tag{A.12}$$

Finally, the temporal phases give the variation of the phases of a particular oscillation with a given period. If the phase increases monotonically from 0° to 360° is an indication of the presence of a cyclicity in the data. They are expressed as:

$$\Psi^k(t) = \arctan\left(\frac{\Im\{\mathrm{A^k(t)}\}}{\Re\{\mathrm{A^k(t)}\}}\right). \tag{A.13}$$

As in standard EOF analysis, the complex field can be reconstructed as the sum of the contributions of the leading j CEOF modes:

$$F(t) = \sum_{k=1}^{j} E^{k*} A^k(t) \tag{A.14}$$

The real field is recovered taking the real part of (A.14).

A very useful way of visualising propagating features in CEOF analyses is the presentation of a series of maps. Animation sequences of spatial components are constructed by multiplying real and imaginary CEOF spatial components E^k by the cosine and sine of the phase respectively. For example, choosing times t at which $\Psi = 0, \pi/2, \pi$, we obtain snapshots of the oscillation during half a cycle.

A.3 Canonical Correlation Analysis

So far we have dealt with a data set of one particular field. Now we are going to consider the case of two different data sets, say $S(t)$ and $P(t)$, and try to find the correlation between the two vectors. The Canonical Correlation Analysis (CCA) technique finds a linear relationship between the two fields by maximising the correlation coefficient between them. In practice, it gives the spatial patterns of both $S(t)$ and $P(t)$ that have maximum correlation.

With data sets forming two matrices $\mathbf{S}$ and $\mathbf{P}$ we construct the covariance matrices $\mathbf{R_{SS}} = \mathbf{S} * \mathbf{S}^\dagger$, $\mathbf{R_{PP}} = \mathbf{P} * \mathbf{P}^\dagger$ and the cross-covariance matrix $\mathbf{R_{SP}} = \mathbf{S} * \mathbf{P}^\dagger$.

Then, we form two matrices as combinations of the three above

$$\mathbf{Q_S} = \mathbf{R_{SS}^{-1}} * \mathbf{R_{SP}} * \mathbf{R_{PP}^{-1}} * \mathbf{R_{SP}^\dagger} \tag{A.15}$$

$$\mathbf{Q_P} = \mathbf{R_{PP}^{-1}} * \mathbf{R_{SP}^\dagger} * \mathbf{R_{SS}^{-1}} * \mathbf{R_{SP}}, \tag{A.16}$$

which are the base of the pair of eigen-equations

$$\mathbf{Q_S} * \mathbf{\Pi_s} = \mathbf{\Pi_S} * \mathbf{\Lambda} \tag{A.17}$$

$$\mathbf{Q_P} * \mathbf{\Pi_p} = \mathbf{\Pi_P} * \mathbf{\Lambda}. \tag{A.18}$$

Π_s^k, Π_p^k are the eigenvectors, or adjoint patterns, of each matrix with associated eigenvalues λ^k; in fact the two matrices share the same non-zero eigenvalues in the diagonal matrix $\mathbf{\Lambda}$.

Now, for each field, we can derive the spatial Canonical Correlation Patterns (CCP) from the adjoint patterns as:

$$\mathbf{E_S} = \mathbf{R_{SS}} * \mathbf{\Pi_S} \tag{A.19}$$

$$\mathbf{E_P} = \mathbf{R_{PP}} * \mathbf{\Pi_P}. \tag{A.20}$$

Finally, the temporal Canonical Correlation Coefficients (tCCC) are obtained from the adjoint patterns in the following way:

$$\mathbf{A_S} = \mathbf{S}^\dagger * \mathbf{\Pi_S} \tag{A.21}$$

$$\mathbf{A_P} = \mathbf{P}^\dagger * \mathbf{\Pi_P}. \tag{A.22}$$

A way of simplifying the procedure, and reducing noise variability, is to compress the data prior to performing the CCA.

Barnett and Preisendorfer (1987) proposed for the first time to perform a CCA after transforming the original fields into EOF space. The data are pre-filtered by a EOF analysis, retaining only a subset of re-normalised leading EOF patterns, and helping emphasising true correlations.

Imagine we retain only the first j leading EOFs: fields $\mathbf{S}'$ and $\mathbf{P}'$ are then built from the EOFs principal components and the corresponding matrices $\mathbf{Q_{S'}}$ and $\mathbf{Q_{P'}}$, since in these coordinates $\mathbf{R_{S'S'}} = \mathbf{R_{P'P'}} = 1$, simplify to:

$$\mathbf{Q_{S'}} = \mathbf{R_{S'P'}} * \mathbf{R^{\dagger}_{S'P'}} \tag{A.23}$$

$$\mathbf{Q_{P'}} = \mathbf{R^{\dagger}_{S'P'}} * \mathbf{R_{S'P'}}, \tag{A.24}$$

Performing a Singular Value decomposition (SVD) of the cross-covariance matrix $\mathbf{R_{S'P'}}$ results in its decomposition into three matrices, i.e. $\mathbf{R_{S'P'}} = \mathbf{U\Sigma V^{\dagger}}$. Matrix $\mathbf{\Sigma}$ is a diagonal matrix of non-negative singular values ordered in decreasing magnitude, while the columns of matrices $\mathbf{U}$ and $\mathbf{V}$ are called the left and right singular vectors.

The adjoint patterns of $\mathbf{S}'$ and $\mathbf{P}'$ are again eigenvectors of (A.23)-(A.24), or equivalently the left and right singular vectors of the SVD respectively, and the eigenvalues, the diagonal matrix of singular values $\mathbf{\Sigma}$, forming the correlation coefficient vector.

The eigenvectors computed with the SVD are given in the coordinates of the EOF space; the adjoint patterns can be expressed back to Euclidean space by reversing the EOF transformation, and the spatial CCP are recovered in the following way:

$$\mathbf{E_S} = \mathbf{S}' * \mathbf{U} * (\lambda_{S'})^{1/2} \tag{A.25}$$

$$\mathbf{E_P} = \mathbf{P}' * \mathbf{V} * (\lambda_{P'})^{1/2}, \tag{A.26}$$

where $\lambda_{S'}$ and $\lambda_{P'}$ are the eigenvalues associated with the EOF-transformed fields. Similarly, the CCC are given by:

$$\mathbf{A_S} = \mathbf{P^{\dagger}_S} * \mathbf{U} \tag{A.27}$$

$$\mathbf{A_P} = \mathbf{P^{\dagger}_P} * \mathbf{V}, \tag{A.28}$$

where $\mathbf{P_S}$ and $\mathbf{P_P}$ are the PC computed during the EOF analysis of fields $S(t)$ and $P(t)$.

Appendix B

Rossby waves in a zonal mean flow

The dispersion relation of Rossby waves in the unperturbed problem was given in Chapter 1. We are now going to compute the dispersion relations of Rossby waves in different zonal mean flows extracted from the model runs. The problem is standard and full derivations of the normal modes in mean flows are given by several authors (Leblond and Mysak, 1978; Pedlosky, 1987; de Szoeke and Chelton, 1999).

We are interested in whether the Rossby wave activity observed in the quasi-geostrophic coupled model is mainly explained by the inclusion of a mean zonal flow in the phase speed calculation. The effect of a baroclinic mean flow on the phase speed of planetary waves has been tackled by many theoretical studies (Killworth et al., 1997; Dewar, 1998; de Szoeke and Chelton, 1999; Liu, 1999a,b; Dewar and Morris, 2000; Tailleux and McWilliams, 2001; Killworth and Blundell, 2005a,b; Colin de Verdière and Tailleux, 2005). However, we will not attempt to do a thorough study on this subject, which would include taking into account boundary layers, short wave propagation, the presence of advective modes and other effects, which are still currently being investigated. Here, we will use standard QG theory and derive the dispersion relation of a Rossby wave in a 3-layer model in the presence of a zonal mean flow taken at different locations of the ocean basin in the model employed in this thesis. The resulting perturbed frequency-wavenumber relation will be tested against the observations.

For a 3-layer system, the inviscid quasi-geostrophic potential vorticity (QGPV) equation is

$$\partial_t q_i + J(\psi_i, q_i) = 0, \qquad i = 1, 3. \tag{B.1}$$

If we consider the basic flow $\psi_n = \Psi_n(y)$ of a purely zonal flow $U_n(y) = -\partial\Psi_n/\partial y$ and look for disturbances so that $\psi_n = \Psi_n(y) + \phi_n(x, y, t)$, substituting into (B.1) gives

$$(\partial_t + U_n\partial_x)q_n + \partial_x\phi_n\partial_y\Pi_n + J(\phi_n, q_n) = 0, \tag{B.2}$$

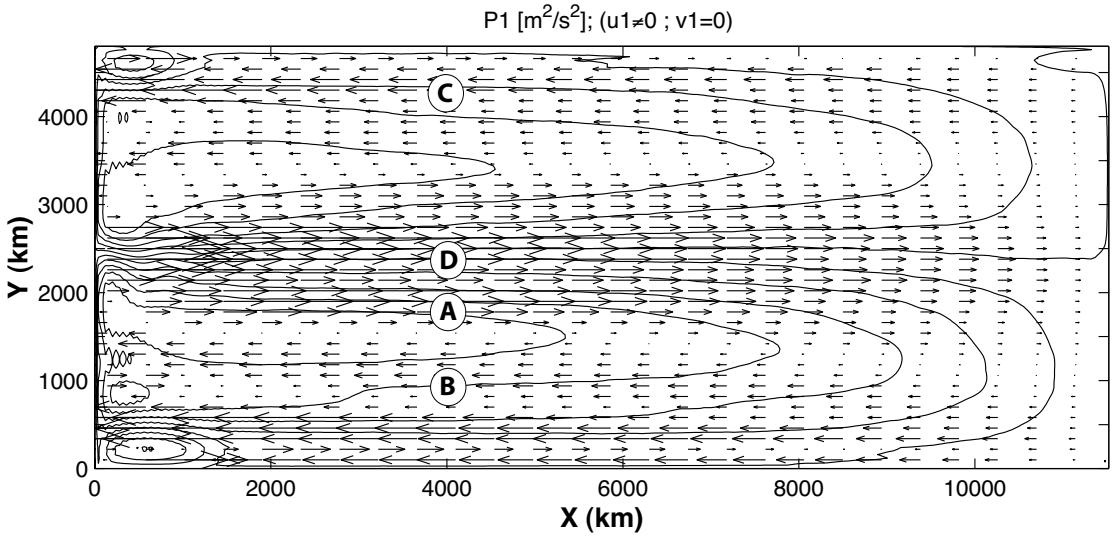

Figure B.1: *First layer mean zonal flow, $\bar{u}_1$ (in arrows), computed from pressure meridional gradients by the geostrophic relation $f_0 u = -\partial_y P_1$. The P_1 field is contoured (Contour interval 10Sv). Four different locations, where the dispersion relation of Rossby waves has been computed, are shown by letters A, B, C and D.*

where the meridional PV gradients in each layer are given by

$$\partial_y \Pi_1 = \beta - F_{11}(U_2 - U_1) \tag{B.3}$$

$$\partial_y \Pi_2 = \beta + F_{21}(U_2 - U_1) - F_{22}(U_3 - U_2) \tag{B.4}$$

$$\partial_y \Pi_3 = \beta + F_{32}(U_3 - U_2), \tag{B.5}$$

and the layer PVs are now defined as

$$\begin{aligned} q_1 &= \nabla^2 \phi_1 + F_{11}(\phi_2 - \phi_1) \\ q_2 &= \nabla^2 \phi_2 + F_{21}(\phi_1 - \phi_2) + F_{22}(\phi_3 - \phi_2) \\ q_3 &= \nabla^2 \phi_3 + F_{32}(\phi_2 - \phi_3), \end{aligned}$$

where $F_{m,n} = f_0^2/(H_m g'_n)$ and g'_n and H_m are the reduced gravities and layer depths respectively.

After neglecting terms of $\mathrm{O}({\phi_n}^2)$, we seek solutions of the form $\phi = \hat{\phi} e^{i(kx - \sigma t)}$:

$$(kU_1 - \sigma)[-k^2\phi_1 + F_{11}(\phi_2 - \phi_1)] + k\phi_1 \partial_y \Pi_1 = 0 \tag{B.6}$$

$$(kU_2 - \sigma)[-k^2\phi_2 + F_{21}(\phi_1 - \phi_2) + F_{22}(\phi_3 - \phi_2)] + k\phi_2 \partial_y \Pi_2 = 0 \tag{B.7}$$

$$(kU_3 - \sigma)[-k^2\phi_3 + F_{32}(\phi_2 - \phi_3)] + k\phi_3 \partial_y \Pi_3 = 0. \tag{B.8}$$

The above equations can be cast into a generalised eigenvalue problem of the form $\mathsf{A}\Phi = \sigma \mathsf{B}\Phi$, where $\Phi = [\phi_1, \phi_2, \phi_3]$ are the eigenvectors and σ the eigenfrequency. Thus, for different mean flows U_i, we will be able to study the wave response in terms of its perturbed dispersion relation.

The system of equations (B.6)-(B.7)-(B.8) can be explicitly written in matrix notation as

$$\begin{bmatrix} B_1 & kU_1 & 0 \\ G_2 kU_2 & B_2 & kU_2 \\ 0 & kU_3 & B_3 \end{bmatrix} \begin{bmatrix} \phi_1 \\ \phi_2 \\ \phi_3 \end{bmatrix} = \sigma \begin{bmatrix} -G_1 & 1 & 0 \\ G_2 & -G_3 & 1 \\ 0 & 1 & -G_4 \end{bmatrix} \begin{bmatrix} \phi_1 \\ \phi_2 \\ \phi_3 \end{bmatrix},$$

where we have defined

$$\begin{aligned} B_1 &= [k\partial_y \Pi_1 - kU_1(k^2 + F_{11})]/F_{11} \\ B_2 &= [k\partial_y \Pi_2 - kU_2(k^2 + F_{21} + F_{22})]/F_{22} \\ B_3 &= [k\partial_y \Pi_3 - kU_3(k^2 + F_{32})]/F_{32} \\ G_1 &= (K^2 + F_{11})/F_{11} \\ G_2 &= F_{21}/F_{22} \\ G_3 &= (K^2 + F_{21} + F_{22})/F_{22} \\ G_4 &= (K^2 + F_{32})/F_{32} \end{aligned}$$

If the mean flow is set to zero, i.e. $U_1 = U_2 = U_3 = 0$, the unperturbed solution (1.1.1) is recovered.

The mean zonal flows are extracted from the layer pressure meridional gradients via the geostrophic relation $f_0 U_i = -\partial_y P_i$. Four cases with different shear are given as an example of possible solutions; their location is shown in Fig.B.1 and their values are listed on Table B.1.

Case A is the typical vertical shear found by meridional density sections at the latitudes considered and was the example proposed in the study of de Szoeke and Chelton (1999). This is also the location were the Hovmoöller plots where constructed in the previous chapters and thus it will be the one considered in the comparisons with the phase speeds observed in the model.

The barotropic, first and second baroclinic mode dispersion relation in the four cases are plotted in Fig.B.2, together with a schematic of the three-layer vertical shear. In general, small speed-ups of the first baroclinic mode are found, especially

Case	U_i [cm s^{-1}]
A	(3.0, -0.75, 0.05)
B	(-2.6, 0.9, 0.01)
C	(-2.8, -1.0, 0.07)
D	(3.5, 2.0, -0.05)

Table B.1: *Mean zonal flows ($\bar{u}_i$) from the model runs at four different locations.*

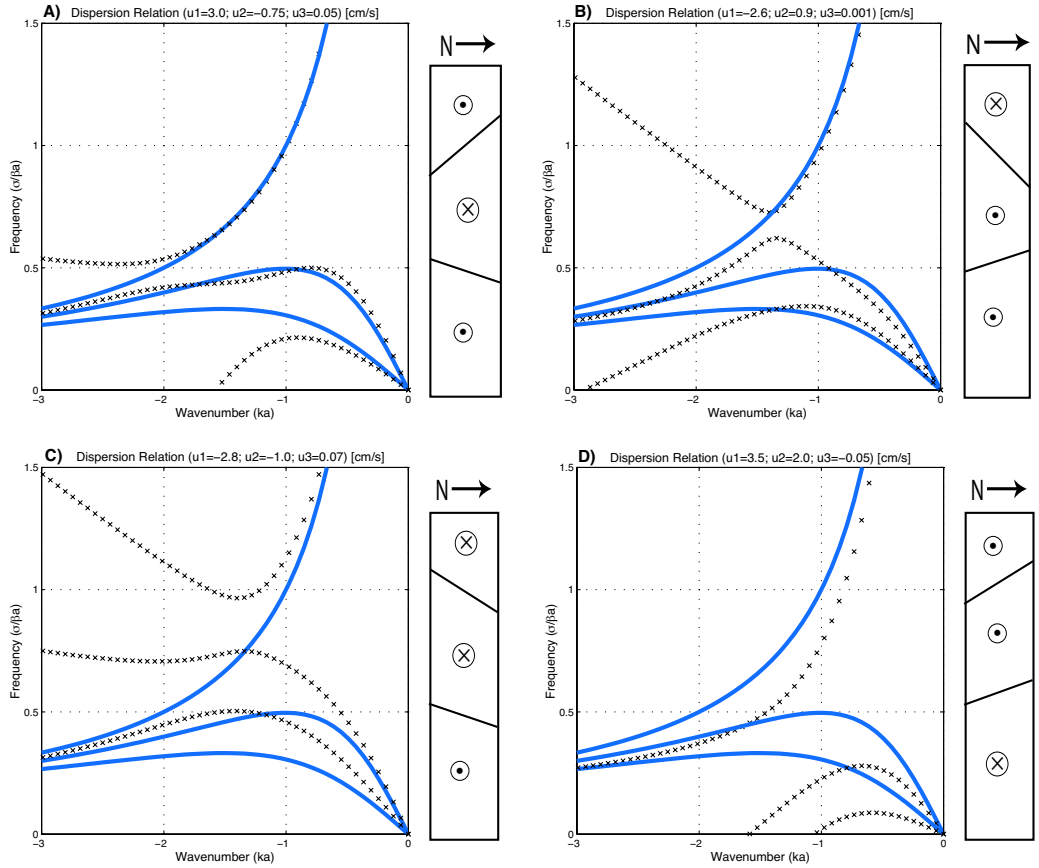

Figure B.2: *Barotropic, first and second baroclinic mode perturbed dispersion relations (x-lines) for the different mean flows of Table B.1 and the unperturbed solutions (blue lines). The vertical shears are schematised in each case.*

in the long-wave limit. However, negative effects on the second baroclinic mode and significant modifications in the behaviour of the barotropic mode for short wave are evident.

de Szoeke and Chelton (1999) suggested that in a QG layered system the speed-up of the planetary wave propagation speed is a function of the layer depths H_i and the density difference ratio. The mechanism proposed by de Szoeke and Chelton (1999) would indicate for our parameter values a speed-up of about 1.4 (their Figure 4). In our calculations we found a variable speed-up/-down depending on the wavelength; for the long-wave region which characterises the Rossby waves observed in the model, we found a maximum speed-up of about 1.2 in Case A (Fig.B.3). This is the solution plotted as solid lines in Fig.4.2.

The choice of layer depths, density jumps and corresponding Rossby radii are therefore crucial in the resulting Rossby wave phase speed if these are to be compared with real data and if a true estimate is attempted. However, the purpose of this exercise is to estimate the wave speed in the model employed, where a particular mean flow on a flat-bottomed ocean is present, given by the slopes of the interfaces

for specific parameter settings.

The system (B.6)-(B.7)-(B.8), although tedious, can be extended for a 6-layer model. We repeated the dispersion relation calculations for our 6-layer results but found no significant changes in the wave speed-up/-down (solid lines in Fig.5.4), most likely due to the fact that the Rossby radii have been kept constant.

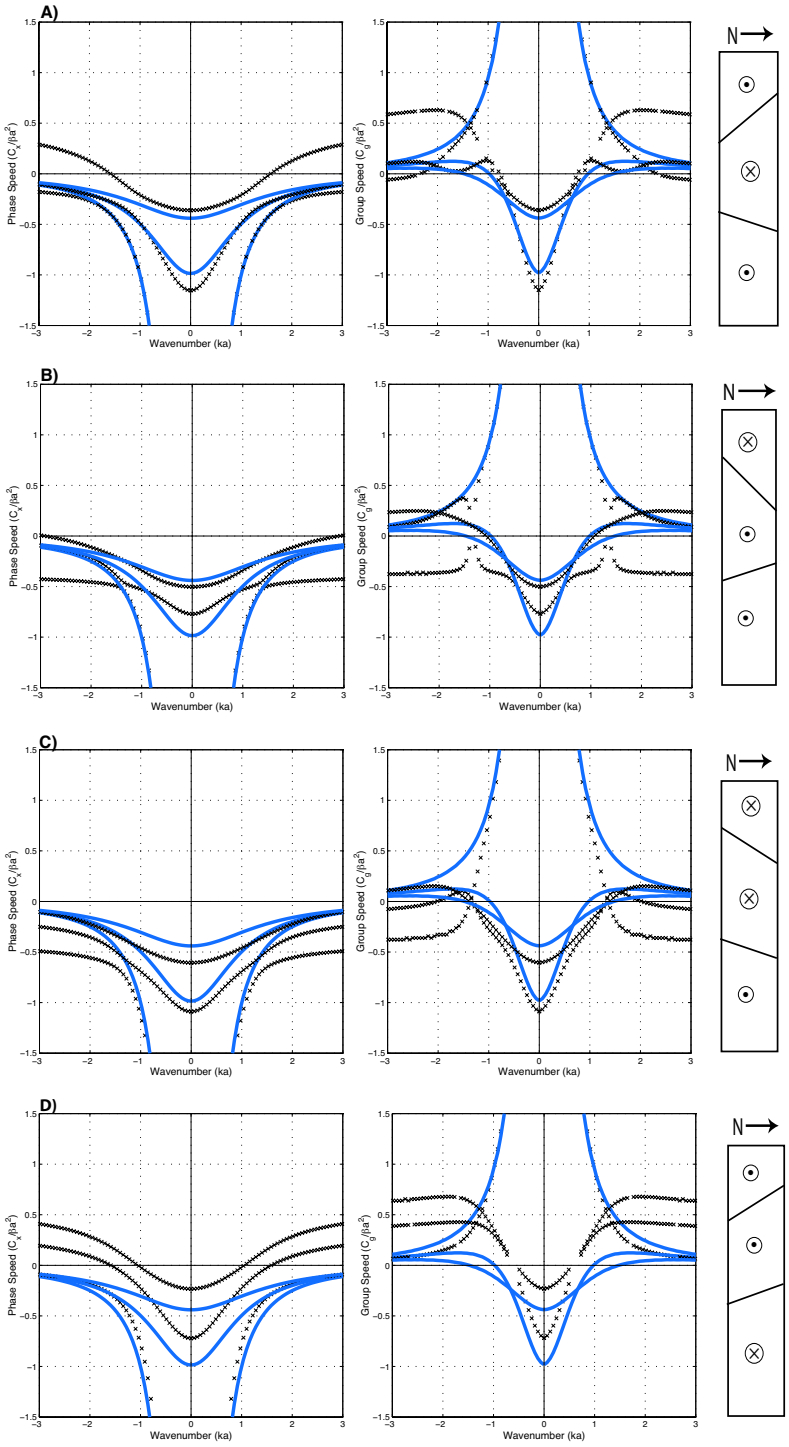

Figure B.3: *As in Fig.B.2 but for the phase and group speeds.*

Bibliography

Anderson, D. L. T. and A. E. Gill, 1975: Spin-up of a stratified ocean, with application to upwelling. *Deep-Sea Res.*, **22**, 583–596.

— 1979: Beta-dispersion of inertial waves. *J. Geophys. Res.*, **84**, 1836–1842.

Arzel, O. and T. Huck, 2003: Decadal oscillations in a simplified coupled model due to unstable interactions between zonal winds and ocean gyres. *Dyn. Atmos. Oceans*, **37**, 245–270.

Barnett, T., D. W. Pierce, R. Saravanan, N. Schneider, D. Dommenget, and M. Latif, 1999: Origins of the midlatitude Pacific decadal variability. *Geophys. Res. Lett.*, **26**, doi:10.1029/1999GL900278.

Barnett, T. and R. Preisendorfer, 1987: Origins and levels of monthly and seasonal forecast skill for United States air temperature determined by canonical correlation analysis. *Mon. Weather Rev.*, **115**, 1825–1850.

Barnier, B., B. Hua, and C. L. Provost, 1991: On the catalytic role of high baroclinic modes in eddy-driven large-scale circulations. *J. Phys. Oceanogr.*, **21**, 976–997.

Barsugli, J. J. and D. S. Battisti, 1998: The basic effects of atmosphere-ocean thermal coupling on midlatitude variability. *J. Atmos. Sci.*, **55**, 477–493.

Bjornsson, H., L. Mysak, and G. Schmidt, 1997: Mixed boundary conditions versus coupling with an energy-moisture balance model for a zonally averaged ocean climate model. *J. Climate*, **10**, 2412–2430.

Bretherton, C. S., C. Smith, and J. M. Wallace, 1992: An intercomparison of methods for finding coupled patterns in climate data. *J. Climate*, **5**, 541–560.

Bye, J., 2004: Growing interfacially coupled oscillations of the ocean-atmosphere. *Dyn. Atmos. Oceans*, **38**, 39–56.

Capotondi, A. and M. Alexander, 2001: Rossby waves in the Tropical Pacific and their role in decadal thermocline variability. *J. Phys. Oceanogr.*, **31**, 3496–3515.

Cessi, P., 2000: Thermal feedback on wind stress as a contributing cause of climate variability. *J. Climate*, **13**, 232–244.

Cessi, P. and P. Otheguy, 2003: Oceanic teleconnections: Remote response to decadal wind forcing. *J. Phys. Oceanogr.*, **33**, 1604–1617.

Cessi, P. and F. Paparella, 2001: Excitation of basin modes by ocean-atmosphere coupling. *Geophys. Res. Lett.*, **31**, 3020–3029.

Cessi, P. and F. Primeau, 2001: Dissipative selection of low-frecuency modes in a reduced-gravity basin. *J. Phys. Oceanogr.*, **31**, 127–137.

Chelton, D. B. and M. G. Schlax, 1996: Global observations of oceanic Rossby waves. *Science*, **272**, 234–238.

Cherry, S., 1996: Singular value decomposition analysis and canonical correlation analysis. *J. Climate*, **9**, 2003–2009.

Cipollini, P., D. Cromwell, P. G. Challenor, and S. Raffaglio, 2001: Rossby waves detected in global ocean colour data. *Geophys. Res. Lett.*, **28**, 323–326.

Cipollini, P., D. Cromwell, G. D. Quartly, and P. G. Challenor, 2000: Remote sensing of extra-tropical Rossby waves. *Satellites,Oceanography and Society*, D. Halpern, ed., Elsevier Science, 99–123.

Colin de Verdière, A. and M. Blanc, 2001: Thermal resonance of the atmosphere to SST anomalies. Implications for the Antarctic circumpolar wave. *Tellus*, **53A**, 403–424.

Colin de Verdière, A. and T. Huck, 1999: Baroclinic instability: an oceanic wavemaker for interdecadal variability. *J. Phys. Oceanogr.*, **29**, 893–910.

Colin de Verdière, A. and R. Tailleux, 2005: The interaction of a baroclinic mean flow with long Rossby waves. *J. Phys. Oceanogr.*, **35**, 865–879.

de Szoeke, R. A. and D. B. Chelton, 1999: The modification of long planetary waves by homogeneous potential vorticty layers. *J. Phys. Oceanogr.*, **29**, 500–511.

Dewar, W., 2001: On ocean dynamics in midlatitude climate. *J. Climate*, **14**, 4380–4397.

Dewar, W. K., 1998: On "too fast" baroclinic planetary waves in the general circulation. *J. Phys. Oceanogr.*, **28**, 1739–1758.

Dewar, W. K. and M. Y. Morris, 2000: On the propagation of baroclinic waves in the general circulation. *J. Phys. Oceanogr.*, **30**, 2637–2649.

Dickinson, R. E., 1978: Rossby waves-long period oscillations of oceans and atmosphere. *Annu. Rev. Fluid Mech.*, **10**, 159–195.

Dijkstra, H. A. and C. A. Katsman, 1997: Temporal variability of the wind-driven quasi-geostrophic double gyre ocean circulation: basic bifurcation diagrams. *Geophys. Astrophys. Fluid Dynam.*, **85**, 195–232.

Fanning, A. F. and A. Weaver, 1996: An atmospheric energy-moisture balance model: climatolgy, interpentadal climate change, and coupling to an ocean general circulation model. *J. Geophys. Res.*, **101**, 15111–15128.

Ferreira, D. and C. Frankignoul, 2005: The transient atmospheric response to midlatitude SST anomalies. *J. Climate*, **18**, 1049–1067.

Ferreira, D., C. Frankignoul, and J. Marshall, 2001: Coupled ocean-atmosphere dynamics in a simple midlatitude climate model. *J. Climate*, **14**, 3704–3723.

Frankignoul, C., 1985: Sea surface temperature anomalies, planetary waves, and air-sea feedback in the middle latitudes. *Reviews of geophysics*, **23**, 357–390.

Frankignoul, C., P. Müller, and E. Zorita, 1997: A simple model of decadal response of the ocean to stochastic wind forcing. *J. Phys. Oceanogr.*, **27**, 1533–1546.

Fu, L.-L., 2004: Latitudinal and frequency characterisctics of the westward propagation of large-scale oceanic variability. *J. Phys. Oceanogr.*, **34**, 1907–1921.

Fu, L.-L. and B. Qiu, 2002: Low-frequency variability of the North Pacific ocean: The roles of boundary- and wind-driven baroclinic Rossby waves. *J. Geophys. Res.*, **107(C12)**, doi:10.1029/2001JC001131.

Galanti, E. and E. Tziperman, 2003: A midlatitude-ENSO teleconnection mechanism via baroclinically unstable long Rossby waves. *J. Phys. Oceanogr.*, **33**, 1877–1888.

Gallego, B. and P. Cessi, 2000: Exchange of heat and momentum between the atmosphere and the ocean: a minimal model of decadal oscillations. *Climate. Dyn.*, **16**, 479–489.

Gill, A. E., 1982: *Atmosphere-Ocean Dynamics*, volume **30**. Academic Press, International Geophysics Series, 662 pp.

Goodman, J., 2001: *Interannual middle-latitude atmosphere-ocean interactions*. Ph.D. thesis, Massachusetts Institute of Technology.

Goodman, J. and J. Marshall, 1999: A model of decadal middle-latitude atmosphere-ocean coupled modes. *J. Climate*, **12**, 621–641.

— 2002: Using neutral singular vectors to study low-frequency atmospheric variability. *J. Atmos. Sci.*, **59**, 3206–3222.

— 2003: The role of neutral singular vectors in midlatitude air-sea coupling. *J. Climate*, **16**, 88–102.

Haney, R., 1971: Surface thermal boundary condition for ocean circulation models. *J. Phys. Oceanogr.*, **1**, 241–248.

Harvey, L., 1988: A semi-analytic energy balance climate model with explicit sea ice and snow physics. *J. Climate*, **1**, 1065–1085.

Held, I., 1983: Stationary and quasi-stationary eddies in the extratropical troposphere: Theory. *Large-scale dynamical processes in the Atmosphere*, R. P. Pearce and B. J. Hoskins, eds., Academic Press, 127–168.

Hill, K. L., I. Robinson, and P. Cipollini, 2000: Propagation characteristics of extratropical planetary waves observed in the ATSR global sea surface temperature record. *J. Geophys. Res.*, **105**, 21927–21945.

Hogg, A., J. Blundell, W. Dewar, and P. Killworth, 2003a: Formulation and users guide for q-gcm (version 1.0). *Southampton Oceanography Centre Internal document n.88, pp.40*.

Hogg, A., W. Dewar, P. Killworth, and J. Blundell, 2003b: A quasi-geostrophic coupled model: Q-GCM. *Mon. Weather Rev.*, **131**, 2261–2278.

— 2005: Decadal variability of the midlatitude climate system driven by the ocean circulation. *J. Climate*, in press.

Hough, S., 1897: On the application of harmonic analysis to the dynamical theory of the tides, Part I, on Laplace's oscillations of the first species, and on the dynamics of ocean currents. *Phil. Trans. Roy. Soc. Lond.*, **189**, 201–257.

Huck, T. and G. Vallis, 2001: Linear stability analysis of the three-dimensional thermally-driven ocean circulation: application to interdecadal oscillations. *Tellus*, **53A**, 526–545.

Huck, T., G. Vallis, and A. C. de Verdière, 2001: On the robustness of the interdecadal modes of the thermohaline circulation. *J. Phys. Oceanogr.*, **14**, 940–963.

Hughes, C. W., 1995: Rossby waves in the Southern Ocean: A comparison of TOPEX/POSEIDON altimetry with model predictions. *J. Geophys. Res.*, **100**, 15933–15950.

Jin, F.-F., 1997: A theory for interdecadal climate variability of the North Pacific ocean-atmosphere system. *J. Climate*, **10**, 1821–1835.

Jin, F.-F., J.-S. Kug, S.-I. An, and I.-S. Kang, 2003: A near annual coupled ocean-atmosphere mode in the equatorial Pacific ocean. *Geophys. Res. Lett.*, **30**, doi:10.1029/2002GL015983.

Johnson, H. L. and P. Marshall, 2002: A theory for the surface Atlantic response to thermohaline variability. *J. Phys. Oceanogr.*, **32**, 1121–1132.

Katsman, C. A., 2001: *Internal variability of the wind-driven ocean circulation*. Ph.D. thesis, University of Utrecht, Netherlands.

Kawase, M., 1987: Establishment of deep ocean circulation driven by deep-water production. *J. Phys. Oceanogr.*, **17**, 2294–2317.

Kiehl, J. T., 1992: *Atmospheric general circulation modeling. In: Climate system modeling, Ed. K.E. Trenberth.*, Cambridge University Press. 319–369.

Killworth, P. D. and J. R. Blundell, 1999: The effect of bottom topography on the speed of long extratropical planetary waves. *J. Phys. Oceanogr.*, **29**, 2689–2710.

— 2003: Long extra-tropical planetary wave propagation in the presence of slowly varying mean flow and bottom topography. I: the local problem. *J. Phys. Oceanogr.*, **33**, 784–801.

— 2005a: The dispersion relation for planetary waves in the presence of mean flow and topography: I. Analytical theory and one-dimensional examples. *J. Phys. Oceanogr.*, **34**, 2692–2711.

— 2005b: The dispersion relation for planetary waves in the presence of mean flow and topography: II. Two-dimensional examples and global results. *J. Phys. Oceanogr.*, in press.

Killworth, P. D., D. B. Chelton, and R. A. de Szoeke, 1997: The speed of observed and theoretical long extratropical planetary waves. *J. Phys. Oceanogr.*, **27**, 1946–1966.

Killworth, P. D., P. Cipollini, B. M. Uz, and J. R. Blundell, 2004: Physical and biological mechanisms for planetary waves observed in satellite-derived chlorophyll. *J. Geophys. Res.*, **109**, doi:10.1029/2003JC001768, 2004.

Kravtsov, S., P. Berloff, W. K. Dewar, J. C. McWilliams, and M. Ghil, 2005a: Eddy-driven decadal variability in a coupled ocean-atmosphere model of mid-latitude climate. Part II: Dynamics. *J. Climate*, submitted.

Kravtsov, S. and W. Dewar, 2003: On the role of thermohaline advection and sea ice in glacial transitions. *J. Geophys. Res.*, **108**, doi:10.1029/2002JC001439.

Kravtsov, S., W. K. Dewar, P. Berloff, J. C. McWilliams, and M. Ghil, 2005b: Eddy-driven decadal variability in a coupled ocean-atmosphere model of mid-latitude climate. Part I: Phenomenology. *J. Climate*, submitted.

Kravtsov, S. and A. Robertson, 2002: Midlatitude ocean-atmosphere interaction in an idealized coupled model. *Climate. Dyn.*, **19**, 693–711.

Kravtsov, S., A. Robertson, and M. Ghil, 2003: Low-frequency variability in a baroclinic β-channel with land-sea contrast. *J. Atmos. Sci.*, **60**, 2267–2293.

Kravtsov, S., A. W. Robertson, and M. Ghil, 2005c: Bimodal behaviour in the zonal mean flow of a baroclinic β-channel model. *J. Atmos. Sci.*, **62**, 1746–1769.

Kundu, P. K. and I. M. Cohen, 2002: *Fluid Mechanics*. Academic Press, second edition, xxiv+730 pp.

LaCasce, J. and J. Pedlosky, 2002: Baroclinic Rossby waves in irregular basins. *J. Phys. Oceanogr.*, **32**, 2828–2847.

— 2004: The instability of Rossby basin modes and the oceanic eddy field. *J. Phys. Oceanogr.*, **34**, 2027–2041.

Latif, M. and T. P. Barnett, 1994: Causes of decadal climate variability over the North Pacific and North America. *Science*, **266**, 634–637.

— 1996: Decadal climate variability over the North Pacific and North America: Dynamics and predictability. *J. Climate*, **9**, 2407–2423.

Leblond, P. H. and L. A. Mysak, 1978: *Waves in the Ocean*. Elsevier, xiv+602 pp.

Ledwell, J., A. Watson, and C. Law, 1998: Mixing of a tracer in the pycnocline. *J. Geophys. Res.*, **103**, 21499–21529.

Lehoucq, R. B., D. C. Sorensen, and C. Yang, 1998: *ARPACK Users' guide: Solution of large scale eigenvalue problems with Implicitly Restarted Arnoldi Methods*. SIAM Publications, 160 pp.
URL `www.caam.rice.edu/software/ARPACK/index.html`

Liu, Z., 1993: Interannual positive feedbacks in a simple extratropical air-sea coupling system. *J. Atmos. Sci.*, **50**, 3022–3028.

— 1999a: Forced planetary wave response in a thermocline gyre. *J. Phys. Oceanogr.*, **29**, 1036–1055.

— 1999b: Planetary wave modes in the thermocline: non-doppler-shift mode, advective mode and green mode. *Quart. J. Roy. Meteor. Soc.*, **125**, 1315–1339.

Liu, Z. and L. Wu, 2004: Atmospheric response to North Pacific SST: The role of ocean-atmosphere coupling. *J. Climate*, **17**, 1859–1882.

Longuet-Higgins, M. S., 1965: Planetary waves on rotating sphere II. *Proc. R. Soc. A*, **284**, 40–54.

Marshall, J. and F. Molteni, 1993: Toward a dynamical understanding of planetary-scale flow regimes. *J. Atmos. Sci.*, **50**, 1792–1818.

Munk, W. and C. Wunch, 1998: Abyssal recipes II: energetics of tidal and wind mixing. *Deep-Sea Res.*, **45**, 1977–2010.

Münnich, M., M. Latif, S. Venzke, and E. Maier-Reimer, 1998: Decadal oscillations in a simple coupled model. *J. Climate*, **11**, 3309–3319.

Navarra, A., 1993: A new set of orthonormal modes for linearized meteorological problems. *J. Atmos. Sci.*, **50**, 2569–2583.

Neelin, J. and W. Weng, 1999: Analytical prototypes for ocean-atmosphere interaction at midlatitudes. Part I: Coupled feedbacks as a sea surface temperature dependent stochastic process. *J. Phys. Oceanogr.*, **12**, 697–721.

Nilsson, J., 2001: Spatial reorganization of SST anomalies by stationary atmospheric waves. *Dyn. Atmos. Oceans*, **34**, 1–21.

North, G., 1975: Theory of energy-balance climate models. *J. Atmos. Sci.*, **32**, 2033–2043.

North, G., R. Cahalan, and J. Coakley, 1981: Energy balance climate models. *Rev. Geophys. Space Phys.*, **19**, 91–121.

Osychny, V. and P. Cornillon, 2004: Properties of Rossby waves in the North Atlantic estimated from satellite data. *J. Phys. Oceanogr.*, **34**, 61–76.

Paldor, N. and A. J. Mariano, 2005: The westward phase speed of planetary waves on the beta-plane and on the spherical earth. *J. Phys. Oceanogr.*, submitted.

Pedlosky, J., 1987: *Geophysical Fluid Dynamics*. Springer-Verlag, 710 pp.

Pierce, D., T. P. Barnett, N. Schneider, R. Saravanan, D. Dommenget, and M. Latif, 2001: The role of ocean dynamics in producing decadal climate variability in the North Pacific. *Climate Dyn.*, **18**, 51–70.

Pierce, D., K.-Y. Kim, and T. Barnett, 1996: Variability of the thermohaline circulation in an ocean general circulation model coupled to an atmospheric energy balance model. *J. Phys. Oceanogr.*, **26**, 725–738.

Preisendorfer, R. W. and C. D. Mobley, 1988: *Principal component analysis in meteorology and oceanography*. Elsevier, 425 pp.

Qiu, B. and F.-F. Jin, 1997: Antarctic circumpolar waves: an indication of ocean-atmosphere coupling in the extratropics. *Geophys. Res. Lett.*, **24**, 2585–2588.

Qiu, B., W. Miao, and P. Müller, 1997: Propagation and decay of forced and free Rossby waves in off-equatorial oceans. *J. Phys. Oceanogr.*, **27**, 2405–2417.

Rhines, P., 1986: Vorticity dynamics of the oceanic general circulation. *Annu. Rev. Fluid Mech.*, **18**, 433–497.

Santoso, A. and M. H. England, 2004: Antarctic intermediate water circulation and variability in a coupled climate model. *J. Phys. Oceanogr.*, **34**, 2160–2179.

Sheremet, V., G. R. Ierley, and V. Kamenkovich, 1997: Eigenanalysis of the two-dimensional wind-driven ocean circulation. *J. Mar. Res.*, **55**, 57–92.

Shutts, G., 1987: Some comments on the concept of thermal forcing. *Quart. J. Roy. Meteor. Soc.*, **113**, 1387–1394.

Simonnet, E. and H. A. Dijkstra, 2002: Spontaneous generation of low-frequency modes of variability in the wind-driven ocean circulation. *J. Phys. Oceanogr.*, **32**, 1747–1762.

Solomon, A. and J. McCready, 2003: Interannual and decadal variability in an intermediate coupled model of the Pacific region. *J. Climate*, **16**, 383–405.

Tailleux, R. and J. C. McWilliams, 2001: The effect of bottom pressure decoupling on the speed of extratropical, baroclinic Rossby waves. *J. Phys. Oceanogr.*, **31**, 1461–1476.

Talley, L., 1999: Simple coupled midlatitude climate models. *J. Phys. Oceanogr.*, **29**, 2016–2037.

Trenberth, K., ed., 1992: *Climate system modeling*. Cambridge University Press, 788 pp.

van der Avoird, E., H. Dijkstra, J. Nauw, and C. Schuurmans, 2002: Nonlinearly induced low-frequency variability in a midlatitude coupled ocean-atmosphere model of intermediate complexity. *Climate. Dyn.*, **19**, 303–320.

Venegas, S. A., 2001: *Statistical Methods for Signal Detection in Climate*. Danish Center for Earth System Science Report No. 2, 96 pp.

von Storch, H. and A. Navarra, eds., 1999: *Analysis of Climate Variability*. Springer-Verlag, 342 pp.

von Storch, H. and F. W. Zwiers, 2001: *Statistical Analysis in Climate Research*. Cambridge Univesity Press, 484 pp.

Weaver, A. J., M. Eby, E. C. Wiebe, C. M. Bitz, P. B. Duffy, T. L. Ewen, A. F. Fanning, M. M. Holland, A. MacFadyen, H. D. Matthews, K. J. Meissner, O. Saenko, A. Schmittner, H. Wang, and M. Yoshimori, 2001: The UVic Earth System Climate Model: model description, climatology, and applications to past, present and future climates. *Atmos-Ocean*, **39**, 361–428.

Webb, D. and N. Suginohara, 2001: Vertical mixing in the ocean. *Nature*, **409**, 37.

White, W. B., 2000a: Coupled Rossby waves in the Indian ocean on interannual timescales. *J. Phys. Oceanogr.*, **30**, 2972–2988.

— 2000b: Tropical coupled Rossby waves in the Pacific ocean-atmosphere system. *J. Phys. Oceanogr.*, **30**, 1245–1264.

— 2001: Evidence for coupled Rossby waves in the annual cycle of the Indo-Pacific ocean. *J. Phys. Oceanogr.*, **31**, 2944–2957.

— 2004: Comment on "Synchronous variability in the Southern Hemisphere atmosphere, sea ice, and ocean resulting from the annual mode. *J. Climate*, **11**, 2249–2254.

White, W. B., Y. Ghao, and C. K. Tai, 1998: Coupling of biennial oceanic Rossby waves with the overlying atmosphere in the Pacific basin. *J. Phys. Oceanogr.*, **28**, 1236–1251.

White, W. B. and R. G. Peterson, 1996: An Antarctic circumpolar wave in surface pressure, wind, temperature and sea-ice extent. *Nature*, **380**, 699–702.

Wunsch, C. and X. Zang, 1999: The observed dispersion relationship for the North Pacific Rossby wave motions. *J. Phys. Oceanogr.*, **29**, 2183–2190.

Yang, H., Z. Liu, and Q. Zhang, 2004: Tropical ocean decadal variability and resonance of planetary wave basin modes. Part II: Numerical study. *J. Climate*, **17**, 1711–1721.